NANOGENERATOR FOR MECHANICAL ENERGY HARVESTING AND ITS HYBRIDIZATION WITH LI-ION BATTERY

A Dissertation
Presented to
The Academic Faculty

by

Sihong Wang

In Partial Fulfillment
of the Requirements for the Degree
Doctor of Philosophy in the
School of Materials Science and Engineering

Georgia Institute of Technology
May, 2014

NANOGENERATOR FOR ENERGY HARVESTING AND ITS HYBRIDIZATION WITH LI-ION BATTERY

Approved by:

Dr. Zhong Lin Wang, Advisor
School of Materials Science and Engineering
Georgia Institute of Technology

Dr. Russell D. Dupuis
School of Electrical and Computer Engineering
Georgia Institute of Technology

Dr. Meilin Liu
School of Materials Science and Engineering
Georgia Institute of Technology

Dr. Mostafa A. El-Sayed
School of Chemistry and Biochemistry
Georgia Institute of Technology

Dr. David L. McDowell
School of Materials Science and Engineering/Mechanical Engineering
Georgia Institute of Technology

Dr. Paul A. Kohl
School of Chemical and Biochemical Engineering
Georgia Institute of Technology

Date Approved: March 27, 2014

To my beloved family and friends

ACKNOWLEDGEMENTS

This PhD dissertation is completed under the guidance, the support, the care, and the help from a lot of important people in my life. I would like to extend my deepest sense of gratitude to all of them.

First of all, I like to express my deepest thanks to my advisor—Prof. Zhong Lin Wang, who gave me this invaluable chance to pursue the PhD degree under his guidance. During these years of studying and doing research as his student, I have achieved considerable growth towards a good scientific researcher under his direction and the influence of his personality. His pioneering scientific vision has not only led me into a great research field that I can work on throughout my life, but also taught me about how to choose the research field as a good scientist. His critical directions on research have helped me to build up my research capabilities. More importantly, his behaviors and personalities have set him as the best role model for me of a good person and an effective researcher. As his student, I received unreserved supports and care from him, not only on my career development, but also on my personal life. In Prof. Wang's group, I launched my academic career in the best way. All the things I learnt from him will surely benefit me for my entire life.

Moreover, I also would like to extend my thanks to the professors serving on my dissertation committee: Dr. El-Sayed, Dr. Dupuis, Dr. Liu, Dr. Kohl, and Dr. McDowell. It is truly a great honor of mine to have these prestigious professors as my committee members. They have spent their precious time to give advice on my research and supports on my career development.

During these years as a PhD student, I have received tremendous help from my group members and my friends in Georgia Tech, without whom I could not have gone this far or had a happy life in the US. Thanks to Dr. Rusen Yang and Dr. Guang Zhu, who have mentored me on my research in my first years and taught me about how to do research and the basic experimental skills. I also received plenty of help and learned a lot from those great researcher and nice persons whom I have collaborated with: Long Lin, Yannan Xie, Dr. Xinyu Xue, Simiao Niu, Chang Liu, Dr. Ya Yang, Chang Liu, Fang Yi. Moreover, I would like to thank Mr. Tiejun Zhang for all his helps on various technique issues I have met in my research projects. I also feel very fortunate having a good roommate—Wentian Gu, who has lived in the same apartment with me for 4 years. He has given me a lot of care and help on my life. Also many thanks to those who have helped me on my research and my life from different aspects: Dr. Jinhui Song, Dr. Yong Ding, Dr. Youfan Hu, Dr. Wenzhuo Wu, Dr. Caofeng Pan, Yusheng Zhou, Dr. Fengru Fan, Dr. Sheng Xu, Dr. Wenxi Guo, Ying Liu, Xiaonan Wen, Ruomeng Yu, Fan Bai, etc.

Last but not least, I would like to give my most special thanks to my family. My parents have given all their unconditional love to me since I was born. They serve as my first and most important “advisors” in my life. It is from them that I start to know how to behave as a good people and what my life should be. They made me who I am today. My mother, who is a successful professor in China, has been and will continue to be my role-model throughout my whole life. The achievements I have obtained today also attribute to my grandmother, and my grandfather who passed away 14 years ago. In my childhood, I was mostly looked after by them. Even in her 70’s, my grandmother still takes care the daily life of me and my family. During the past years of my PhD study, she came to

Atlanta twice to help me on my personal life. Any words cannot express my deepest thanks to her. Moreover, I also want to say thank you to my girlfriend. For the pursuit of my academic career, I cannot stay together with her and do what a boyfriend should do. But she has been giving me all her understandings, firm supports and constant care. Whenever I meet some difficulty and feel frustrated, she will encourage me and help me to get out from troughs. All these important peoples—my parents, my grandparents, my girlfriend—are the deepest and long-lasting drive for me to keep moving forward!

TABLE OF CONTENTS

LIST OF TABLES

LIST OF FIGURES

LIST OF ABBREVIATIONS

TENG	Triboelectric Nanogenerator
SEM	Scanning Electron Microscope
XRD	X-Ray Diffraction
ICP-RIE	Inductively Coupled Plasma-Reactive Ion Etching
PTFE	Polytetrafluoroethylene
PMMA	Poly(methyl methacrylate)
PDMS	Polydimethylsiloxane
PET	Polyethylene terephthalate
PVDF	Polyvinylidene fluoride
PE	Polyethylene
SCPC	Self-Charging Power Cell
SCPU	Self-Charging Power Unit

SUMMARY

Energy harvesting and energy storage are two most important technologies in today's green and renewable energy science. As for energy harvesting, the fundamental science and practically applicable technologies are not only essential in realizing the self-powered electronic devices and systems, but also tremendously helpful in meeting the rapid-growing world-wide energy consumptions. Mechanical energy is one of the most universally-existing, diversely-presenting, but usually-wasted energies in the natural environment. Owing to the limitations of the traditional technologies for mechanical energy harvesting, it is highly desirable to develop new technology that can efficiently convert different types of mechanical energy into electricity. On the other hand, the electricity generated from environmental energy often needs to be stored in energy storage unit before used to drive electronic devices. For the energy storage units such as Li-ion batteries as the power sources, the limited lifetime is the prominent problem. Hybridizing energy harvesting devices with energy storage units could not only provide new solution for this, but also lead to the realization of sustainable power sources.

In this dissertation, the research efforts have led to several critical advances in a new technology for mechanical energy harvesting—triboelectric nanogenerators (TENGs). Previous to the research of this dissertation, the TENG only has one basic mode—the contact mode. Through rational structural design, we largely improved the output performance of the contact-mode TENG and systematically studied their characteristics as a power source. Beyond this, we have also established the second basic mode for TENG—the lateral sliding mode, and demonstrated sliding-based disk TENGs for harvesting rotational energy and wind-cup-based TENGs for harvesting wind energy. In order to expand the application and versatility of TENG by avoid the connection of the electrode on the moving part, we further developed another basic mode—freestanding-

layer mode, which is capable of working with supreme stability in non-contact mode and harvesting energy from any free-moving object. Both the grating structured and disk-structured TENGs based on this mode also display much improved long-term stability and very high energy conversion efficiency. For the further improvement of the TENG's output performance from the material aspect, we introduced the ion-injection method to study the maximum surface charge density of the TENG, and for the first time unraveled its dependence on the structural parameter—the thickness of the dielectric film. The above researches have largely propelled the development of TENGs for mechanical energy harvesting and brought a big potential of impacting people's everyday life.

Targeted at developing sustainable and independent power sources for electronic devices, efforts have been made in this dissertation to develop new fundamental science and new devices that hybridize the nanogenerator-based mechanical energy harvesting and the Li-ion-battery-based energy storage process into a single-step process or in a single device. Through hybridizing a piezoelectric nanogenerator with a Li-ion battery, a self-charging power cell has been demonstrated based on a fundamentally-new mechanical-to-electrochemcial process. The triboelectric nanogenerator as a powerful technology for mechanical energy harvesting has also been hybridized with a Li-ion battery into a self-charging power unit. This new concept of device can sustainably provide a constant voltage for the non-stop operation of electronic devices.

CHAPTER 1

INTRODUCTION

Energy, as the essential support for all the activities on the earth, plays a vitally important role in the development of the human civilization.[1] For the thousands of years in the human history, chemical energy of certain matters, such as food, coals, petroleum and natural gas, is the major form of energy that people rely on. In the ancient time, the most important type of energy needed by people is heat, which was converted from the chemical energy of various fossil fuels simply by combustion. Starting from the discovery of electricity, the electrical machines and equipment have brought people into the modern society. From then on, electrical energy becomes the major type of energy that support people's everyday life and the running of the whole world. As a result, the generation of electricity through the conversion of different types of energy gradually became one of the most important technologies. In the past, the electricity generation was enabled by the generation of heat through the combustion of fuels.[2] Thus, the chemical energy of fossil fuels continues to serve as the major source of energy for human. With the rapid growth of the world's population, the demand for energy is increasing dramatically, and the abundant emissions from the combustion of the fuels are giving the global warming. Thus, searching for renewable and ''green'' energy resources is one of the most urgent issues to the sustainable development of human civilization.[3] On the larger scale, active research and development are taking place into exploring alternative energy resources such as solar, geothermal, biomass, nuclear, wind, and hydrogen. At a much smaller scale, with rapid expansion of electronic devices in both numbers and functionalities towards wireless, portability, and multi-function,[4-7] new type of power sources are desperately needed for independent, sustainable, maintenance-free, and continuous operation of portable electronics, bio-implantable devices, widely-distributed environmental sensors, nanorobotics, and security applications. [8,9]

Harvesting energy in our living environment is the most feasible approach to meet all the above requirements for energy, both in the total quantity for the rapid-growing world energy consumption, and in the advanced functionalities for portable and miniaturized electronics by replacing or working conjunctionally with energy storage units such as batteries. The abundance of energy in our environment exists in the form of solar, thermal, mechanical, chemical, magnetic, biochemical, and so on. Targeted at different forms of energy, vastly different mechanisms and technologies have been developed for generating electricity, such as photovoltaics,[10-15] thermoelectrics[16-18] and so on[19-23]. Energy harvesting, together with energy storage,[24-26] has become a big field—energy science—that determines the development pace of the whole world and the quality of people's everyday life.

1.1 Mechanical Energy Harvesting

Among all these different types of environmental energies, mechanical energy, including vibration, air flow, and human physical motion, is available almost everywhere and at all times, which is called random energy with irregular amplitude and frequencies. Therefore, it is desirable to develop technologies that can effectively and efficiently harvest energy from the environment, through which the operation of the electronic devices/systems could possibly be sustainably and independently self-powered. However, compared to other forms of energy such as solar energy and thermal energy, the harvesting of mechanical energy, especially small scale mechanical energy, is severely overlooked, thus its development far lacks the development of technologies for other forms of energies. This mainly results from the various drawbacks of the traditional technologies for mechanical energy harvesting, which generally fall into three categories—electromagnetics,[27,28] electrostatics[29,30] and piezoelectricity[31,32]. For the target of small-scale mechanical energy harvesting, since the year of 2006, nanogenerators have been developed based on piezoelectric ZnO nanowires (NWs), which emerge as a

revolutionary technology to harvest small-scale mechanical energies.[23,33-37] More recently, enabled by the triboelectric effect,[38-41] which is a well-known phenomenon that can generate electrostatic charges from mechanical contact, triboelectric nanogenerators (TENGs) have been invented.[42-44] They are showing unprecedented advantages in extremely high output and efficiency, low cost, easy fabrication. In the following, both the traditional technology and the most-recently developed nanogenerators for small-scale mechanical energy harvesting will be briefly reviewed.

1.1.1 Electromagnetic Generators

Electromagnetic induction, first discovered by Faraday in 1831, is the generation of electric current in a conductor located within a magnetic field.[45] The conductor typically takes the form of a coil and the electricity is generated by either the relative movement of the magnet and coil, or because of changes in the magnetic field. This serves as the basic mechanism for the electricity generation in the past hundreds of years. In the harvesting of large-scale mechanical energy, the rotating motion of the magnet (or the coil) is driven by the hydropower or wind-power.[46-48]

In the small-scale, the application of this mechanism is mainly based on the designs involving the cantilever structures.[27,28] In principle, either the magnets or the coil can be chosen to be mounted on the beam while the other remains fixed. It is generally preferable, however, to have the magnets attached to the beam as these can act as the inertial mass.

A typical example is an electromagnetic micro generator developed by Beeby *et al.*,[27] for harvesting energy from the vibrations of an air compressor unit, which exhibits large vibration maxima in the range of 0.19–3.7 m/s^2 at frequencies between 43 Hz and 109 Hz. The micro generator was therefore designed to operate within this range and to be as small as possible whilst still generating useable levels of power and voltage. As shown in Figure 1.1, the generator uses four magnets arranged on an etched cantilever

with a wound coil located within the moving magnetic field. This arrangement produces a concentrated flux gradient through the stationary coil as the magnets vibrate. The beams were fabricated from double polished single crystal silicon wafers. The coil was manually bonded to a semi-circular recess machined in the base. The practical volume of the generator components is approximately 0.15 cm^3. With magnet size and coil properties optimized, the final device can produce 46 μW in a resistive load of 4 kΩ from just 0.59 m/s^2 acceleration levels at its resonant frequency of 52 Hz. A voltage of 428 mVrms was obtained from the generator with a 2300 turn coil. From this above example, it can be found that the electromagnetic-based structures for small-scale mechanical energy harvesting are often low in output power, complicated in structural design, expensive in manufacturing cost with the usage of permanent magnetic, and difficult for further miniaturization, all of which limit the practical application of this type of technology.

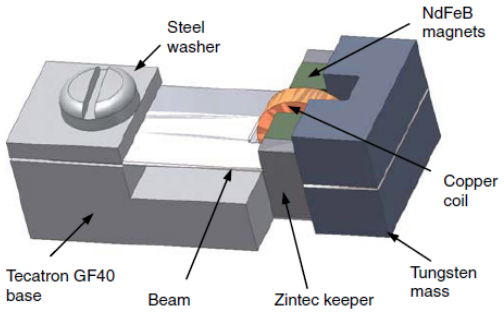

Figure 1.1 Micro electromagnetic cantilever generator. (From ref. 20)

1.1.2 Electrostatic Generators

Electrostatic generator is usually based on a variable capacitor, which consists of two plates, isolated by air, vacuum or an insulator. The charging of the plates by a battery of voltage *V* creates equal but opposite charges on the plates, *Q*, leading to storage of the charge when the voltage source is disconnected. Driven by mechanical vibrations, the capacitive structure changes, leading to the change of its capacitance, and thus the stored energy. The work done against the electrostatic force between the plates provides the harvested energy.[19,29,30]

Electrostatic generators can be classified into three types: 1. in-plane overlap varying; 2. in-plane gap closing; 3. out-of-plane gap closing.[19] These are illustrated in Figure 1.2. Both in-plane configurations create two variable capacitors with the capacitances 180° out of phase. The three approaches can be operated either in charge constrained or voltage constrained cycles. In general, the voltage constrained offers more energy than the charge constrained approach. However, by incorporating a capacitor in parallel with the energy harvesting capacitor, the energy from the charge constrained system can approach that of the voltage constrained system as the parallel capacitance approaches infinity. The previous studies reported that in-plane gap closing offers the highest power output with an optimized design producing 100 μW/cm^3; out-of-plane gap closing is the next highest followed by in-plane overlap varying. Maximum power generation occurs for very small dielectric gaps. From this, we can see that the outputs produced by the electrostatic generators are still too low for driving most electronic devices, and the need for a DC power source largely limits the real application of this technology.

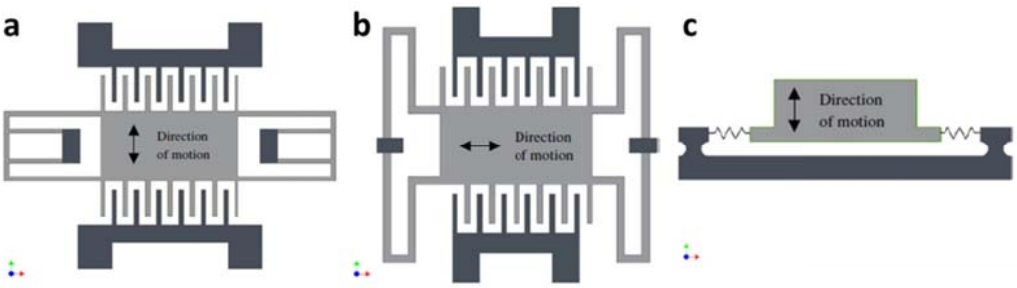

Figure 1.2 Electrostatic generators. (a) In-plane overlapping varying. (b) In-plane gap closing. (c) Out-of-plane gap closing. (From ref. 12)

1.1.3 Piezoelectric (Nano)generators

Piezoelectric ceramics have been used for many years to convert mechanical energy into electrical energy. Traditionally, the piezoelectric generators are based on

thin-film structures, either to collect the impact energy or to harvest vibrational energy through cantilever structures.[31,32,49-51]

Ever since 2006, nanogenerators have been developed based on piezoelectric ZnO nanowires (NWs), for efficiently scavenge tiny-scale mechanical energy.[23,33-37,52-55] In the first demonstration of this idea, as an AFM tip swept across a vertically grown ZnO nanowire (NW), electric voltage/current was generated.[23] The working principle was attributed to the coupling between piezoelectric and semiconducting properties of the ZnO NW. Later in 2008, a new design of NG was developed with a single ZnO NW bonded horizontally on a flexible substrate.[33] Cycled bending of the substrate produced an AC electric output from the NW. Since then, substantial progress has been made to integrate a large number of NWs together, aiming at collecting electric current from all NWs simultaneously. The power output has been directed to a rapidly ascending path, as shown in Figure 1.3.[23,33-36,52,54] Most recently, an integrated NG based on vertically aligned ZnO NWs was developed. The peak open-circuit voltage and short-circuit current reached a record high level of 58 V and 12 μA using an NG of 1cm^2 in size, respectively.[55] Figure 1.3 summarizes the elevation of the piezoelectric NGs' output voltage throughout the 6 years from 2006 to 2012.[56]

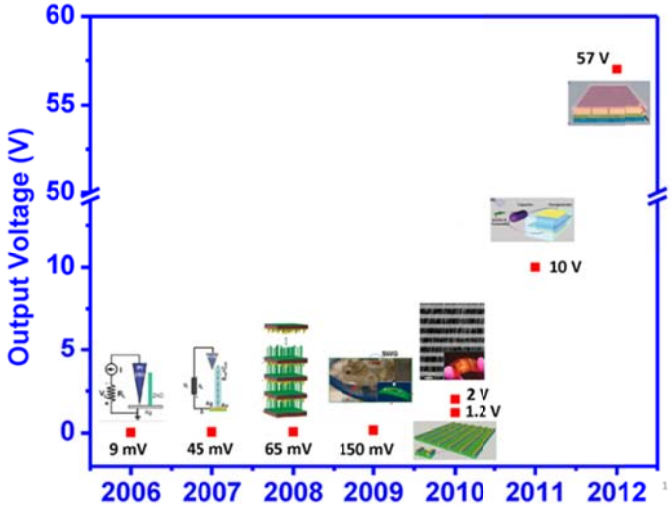

Figure 1.3 A summary on the development of high output piezoelectric nanogenerators ever since it was invented in 2006. (From ref. 48)

1.1.4 Triboelectric Nanogenerator

Triboelectric Effect

Triboelectric effect is a one of the few effects that has been known for thousands years. When a material gets into contact with a different material, the difference in chemical potential of the two surfaces will result in a charge transfer across the interface, making both electrically charged after separation.[38-41] It is generally believed that, after two different materials come into contact, a chemical bond is formed between some parts of the two surfaces, called adhesion, and charges move from one material to the other to equalize their electrochemical potential.[57,58] The transferred charges can be electrons or may be ions/molecules. When separated, some of the bonded atoms have a tendency to keep extra electrons and some a tendency to give them away, possibly producing triboelectric charges on surfaces. Although this fundamental process of the triboelectrification is still in debate, people have been very clear that the contact between almost all the types of materials can produce triboelectric charges, only different in charge densities resulting from different electrochemical potentials of different materials. According to the polarity and density of charges after contact, common materials have been ranked in a series—triboelectric series (Fig. 1.4).[59] In the past thousands of years, although it is widely perceived that the triboelectric charges can often generated a high voltage, this voltage has not been utilized to drive the flow of charges to generate electricity. Actually, this high voltage from the triboelectrification has always been deemed as an undesirable effect for electronic systems.

Figure 1.4 The triboelectric series: a list that ranks various materials according to their tendency to gain (negative) or lose electrons (positive) in the contact charging process.

Triboelectric Nanogenerators

Ever since 2012, a newly invented technology—triboelectric nanogenerator—started to use this effect for harvesting mechanical energy.[42-44] The first triboelectric nanogenerator (TENG) is fabricated by stacking two polymer sheets made of materials having distinctly different triboelectric characteristics, with metal films deposited on the top and bottom of the assembled structure (Fig. 1.5).[43] Once subjected to mechanical deformation, a friction between the two films, owing to the nano-scale surface roughness, generates equal amount but opposite signs of charges at two sides. In meanwhile, the mechanical deformation also causes the change of the gap between the two polymer sheets, so that the opposite triboelectric charges serve as a charge ‘‘pump’’ for driving the flow of electrons in the external load. Such a flexible polymer TENG gives an output voltage of up to 3.3V at a power density of 3.67 mW/cm^2.

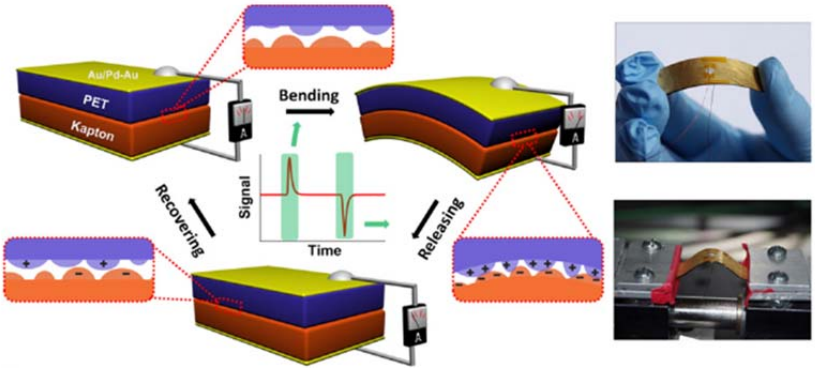

Figure 1.5 Schematic illustration of the structure and working principle of the first triboelectric nanogenerator. (From ref. 36)

The operating principle of such TENGs is based upon the coupling of contact charging and electrostatic induction, as shown in Figure 1.6.[44] In the original state before any contact between the two surfaces, no charge is generated or induced, thus no electric potential difference between the two electrodes (Fig. 1.6I). With an externally applied force, the two polymers are brought into contact with each other. Surface charge transfer then takes place at the contact area due to triboelectrification. As a result, one surface (PMMA) will carry positive charges and the other one (Kapton) with negative charges (Fig. 1.6II). As the generator starts to be released, the Kapton film fully reverts to the original position (Fig. 1.6IV and Fig. 1.6V) and those two oppositely charged surfaces starts to get separated with a gap forming in between. These separated charges will induce a potential difference between the two electrodes, which will drive electrons to flow from the top electrode to the bottom electrode (Fig. 1.6III) in order to balance the generated triboelectric potential, resulting in an instantaneous current peak (Fig. 1.6IV). The net effect is that induced charges accumulate with positive sign on the top electrode and negative sign on the bottom electrode (Fig. 1.6V). Once the generator is pressed again, the top electrode will possess a higher electric potential than the bottom electrode. As a consequence, electrons are driven from the bottom electrode back to the top electrode, reducing the amount of induced charges (Fig. 1.6VI). This process corresponds

to an instantaneous negative current (Fig. 1.6V). When the two polymers are in contact again, all induced charges are neutralized (Fig. 1.6II). When the TENG is subjected to periodic pressing agitations, such a described cycle will repeat again and again to generate electricity from mechanical energy.

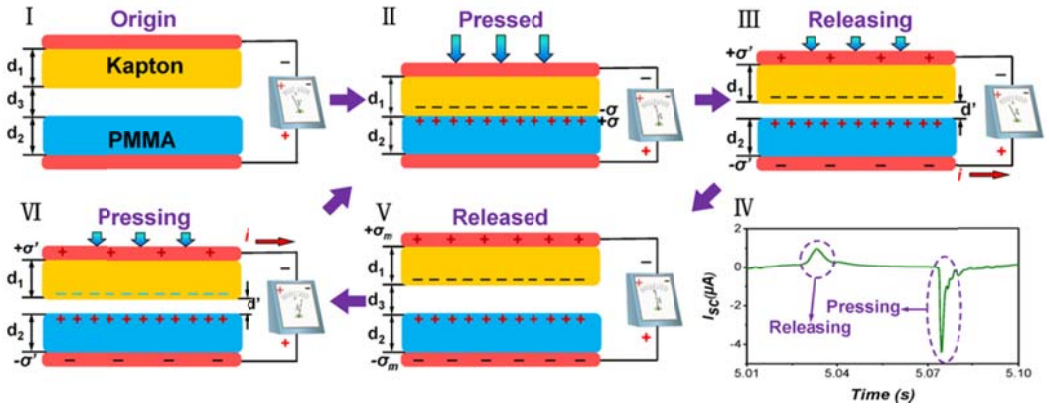

Figure 1.6 Sketches that illustrate the operating principle of the triboelectric nanogenerator. (From ref. 37)

However, in the several as-developed structures of TENGs based on the above mechanism, the electrical output is still relatively too low for the purpose of serving as sustainable power sources for electronics. It is mainly because that these structures were not rationally designed to fulfill the determinant factors in the above electricity generation process. Also, this operation mode of TENGs is not applicable for efficiently harvesting some types of mechanical energies in different applications. Thus, it is highly desirable to explore more fundamental modes for TENGs and design different structures for different applications. Thus, my research target in this dissertation is to achieve the above aspects so that the triboelectric nanogenerator can become a truly revolutionary and practically-applicable technology for both large-scale and small-scale mechanical energy harvesting.

1.2 Energy Storage

Besides energy harvesting, energy storage is another important category of technologies in today's green and renewable energy science.[24,26,60,61] Because the electricity generated by energy harvesters (such as solar cells, nanogenerators, etc.) largely depends on the availability of the targeted environmental energy and have uncontrollable fluctuations and instabilities due to the unstable ambient energy input, the energy harvesters cannot be directly used to drive electronics devices in most cases. The generated electrical energy often needs to be stored in energy storage units in the first place. The energy storage units make the electrical energy "portable", and can supply a stale and controllable electrical output to electronic devices. The electrochemical-system based energy storage technologies (such as batteries and supercapacitors) are widely used as direct power source for most portable electronics, and has attracted massive research efforts during the past decades.

1.2.1 Current research background of energy storage technologies

Lithium-ion battery is one of the most important categories of energy storage units and one of the great successes of modern materials electrochemistry.[24,62-65] Its basic science has been well-established and extensively reported. A lithium-ion battery consists of a lithium-ion intercalation negative electrode (generally graphite), and a lithium-ion intercalation positive electrode (generally the lithium metal oxide, $LiCoO_2$), these being separated by a lithium-ion conducting electrolyte, for example a solution of $LiPF_6$ in ethylene carbonate-diethylcarbonate (Fig. 1.7).[24] The two electrodes have different chemical potentials, dictated by the chemistry that occurs at each. When these electrodes are connected by means of an external device, electrons spontaneously flow from the more negative to the more positive potential. Ions are transported through the electrolyte, maintaining the charge balance, and electrical energy can be tapped by the external

circuit. In rechargeable, batteries, a larger voltage applied in the opposite direction can cause the battery to recharge.

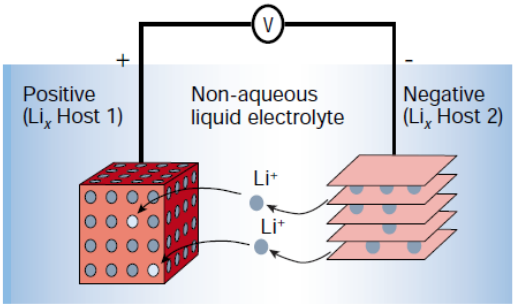

Figure 1.7 Schematic representation and operation principles of Li ion battery. (From ref. 17)

The nature of the energy storage units determines their finite lifetime, which means that they need to be recharged after being used for a certain period of time. Thus, the performance of Li-ion batteries is often characterized by two types of parameters: the capacity (or the stored energy density), and the cyclability. Most of the current research focuses on making improvements on those two aspects of performance through choosing better electrode materials and constructing optimized structures. The specific capacity provided by a material is determined by the number of atoms per formula unit after the insertion of Li^+. From this point, Silicon is the most promising electrode material for a high specific capacity, because of the chemical formula of the lithium-silicon alloy—$Li_{4.4}Si$. Thus, Si provides a theoretical specific capacity of 4,200 mAh g^{-1}, compared with 372 mAh g^{-1} for graphite.[66] However, the accommodation of so much lithium is accompanied by enormous volume changes in the host metal plus phase transitions, which lead to cracking and crumbling of the electrode and a significant loss of capacity in the course of a few cycles. In order to circumvent these issues of Si, nanowire-structure was introduced (Fig. 1.8a).[62] The silicon nanowire battery electrodes can accommodate large strain without pulverization, provide good electronic contact and conduction, and display short lithium insertion distances. The theoretical charge capacity for silicon

anodes was achieved and maintained a discharge capacity close to 75% of this maximum, with little fading during cycling (Fig. 1.8b&c). So far, most investigations of the anode materials are about Si, trying to devise various types of morphologies and structures to accommodate its gigantic volume change, so that its theoretical specific capacity can be reached and maintained for an extended numbers of cycles.

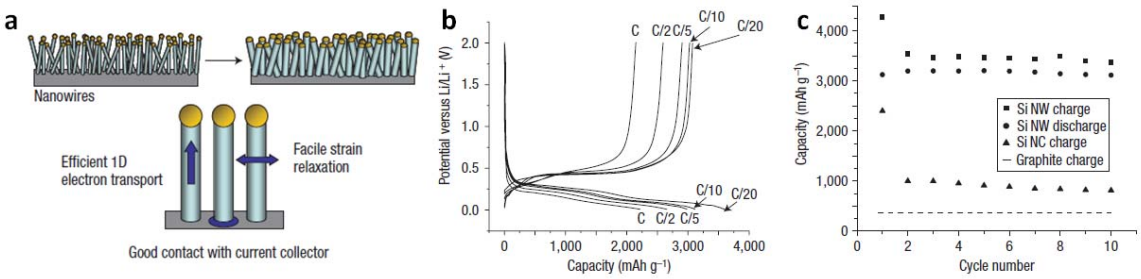

Figure 1.8 High performance Lithium battery anode using Si nanowires. (a) Nanowires (NWs) grown directly on the current collector do not pulverize or break into smaller particles after cycling. (b) The voltage profiles for the Si NWs cycled at different power rates. (c) Capacity versus cycle number for the Si NWs at the C/20 rate showing the charge (squares) and discharge capacity (circles). (From ref. 54)

The development of Li-ion batteries has progressed much more slowly than other areas of electronics. Although extensive efforts have been spent to improve the lifetime of battery by merely one order, graphite has been used as the anode for commercial Li-ion batteries for tens of years. Thus, increasing the lifetime of battery through finding better material systems to enlarge its stored capacity is a very tough approach. More importantly, it cannot radically solve this problem limited lifetime at all.

Alternatively, integrating with energy harvester is another effective approach to extend battery's lifetime. The energy harvester can act as a portable "charger" for the battery, by scavenging energy from the ambient environment and replenish the energy consumption of battery. Since mechanical energy is universally available in the environment, the harvester for scavenging mechanical energy, such as nanogenerators,

can be a promising choice as the portable “charger” for the battery. However, in current technology, such integration is always realized by simply combining two separate units with two different physical processes. This will lead to an integrated power source with a large size, increased complexity, and inflexibility, which is not suitable for miniaturized portable electronics. Moreover, the electricity from nanogenerators often needs to be rectified and regulated before charging the battery. These components for bridging the two processes not only increase the size of the system, but also result in energy loss.

Thus, for the integration energy harvesting and storage, it is desirable to develop new fundamental science and new device structures that can hybridize nanogenerator and Li-ion battery in one device, or even a single process. This is the second goal of this dissertation, which will make significant contributions to the realization of the sustainable and self-sufficient power sources for electronic devices.

CHAPTER 2

HIGH OUTPUT VERTICAL CONTACT-SEPARATION-MODE BASED TRIBOELECTRIC NANOGENERATOR

The triboelectric nanogenerator (TENG) based on the periodic contact and separation of the two oppositely-charged triboelectric layers was previously demonstrated as the first type of TENG. The basic working mechanism of this mode of TENG has been elaborated in Chapter 1, which can be summarized as the conjunction of the triboelectrification and the periodic change of the electrostatically-induced potential difference between the two electrodes. Previous to the study in this dissertation, two different device structures have been developed to enable the above mechanism that can convert this mechanical energy into electricity.[43,44] However, the outputs from these TENGs are still in a relatively low level for serving as sustainable power sources for portable electronics. This is mainly because that previous TENG structures were not rationally designed according to the determinant factors for this electricity generation process. Thus, there is plenty of room for the improvement of the TENG's output by the rational structure design. Moreover, for realizing self-powered systems, the characteristics of this type of TENG as the power sources have not been systematically studied.

2.1 Determinant Factors for Vertical Contact-Separation-Mode TENG

Similarly with piezoelectric (nano)generators, the TENG also has the following physical process[2,3] for producing electricity: generation of immobile charges (ionic charges for piezoelectric generator or electrostatic charges on insulators for TENG), and a periodic separation and contact of the oppositely charged surfaces to change the induced potential across the electrodes, which will drive the flow of free electrons through an external load. The electrical output and efficiency is radically determined by the effectiveness of the above two processes. Thus, the determinant factors for the

effective electricity generation of the contact-mode TENG are the intensive triboelectrification between the two surfaces and the effective change of the electrostatic induction between the two electrodes.

As for the triboelectrification process in the TENG, the resulted static charges on the surface of the triboelectric layer are the resources of the electrostatic induction and also determine the upper limit of charge transfer amount as the generated current flowing through the external load in each working cycle. Thus, it is critically important to maximize triboelectric charge densities on the opposite contacting surfaces. Since the triboelectrification are mainly influenced by both the chemical nature and the physical morphologies of the two surfaces, the triboelectric charge density can be enhanced through two major methodologies: the selection of the pair of materials (including the surface functionalization) with the largest difference in the ability to attract electrons,[67] and the modification of surface morphology.[42] The first approach can be realized by purposely selecting triboelectric layers according to the semi-empirical triboelectric series that ranks the frequently-used materials according to the polarity of the retained charges after one has been contacted with another. As for modification of surface morphology, previous studies have illustrated that introducing microscale/nanoscale patterns and structures on the surfaces can help to increase the triboelectric charge density.

In another aspect, periodic change of the triboelectric-charge-induced potential difference between the two electrodes is the driving force for the back-and-forth flow of the electrons between the two electrodes across the external load. Thus, in order to have a TENG generate electricity efficiently, it is indispensable to make the device structure that can ensure the effective periodic switching between separation and intimate contact of the two charged plates as it is triggered by the surrounding mechanical energy. For the plate-structured TENG, it is not easy to achieve both complete contact and separation of the two oppositely charged plates upon pressing and releasing, especially under the

electrostatic attraction between them. A firmly attached contact of the two oppositely charged surfaces is unfavorable for electricity generation. If we simply use a spacer between the two plates, it will then hinder the complete contact of the two plates.[37] Thus, in order to have the best electrical output from the TENG, we need to rational design a device structure that can enable the two triboelectric surfaces to get into intimate contact under mechanical pressing; and fully separate from each when released.

2.2 Design and Fabrication of Arch-Shaped TENG

In order to have a high electrical output from the TENG through reaching the above two determinant factors, we rational designed an arch-shaped TENG with a steady gap between the plates at strain-free conditions.[68] This was achieved through ingeniously introducing surface thermal stress during thin film deposition.[69,70] Moreover, the arch-shaped TENG is based on the contact electrification between patterned polydimethylsiloxane (PDMS)[42] as the top plate and patterned Al foil as the bottom plate (Fig. 2.1). According to the triboelectric series[59,67] (Fig. 1.4), the purposely-chosen PDMS and Al are almost at the two ends with very large difference in ability to attract and retain electrons. This is also the first TENG based on the triboelectrification between a metal and a dielectric material.[68]

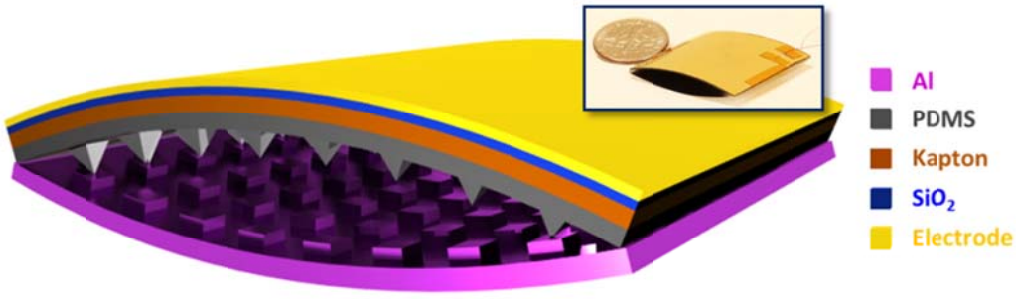

Figure 2.1 Schematic diagram showing the structural design of the arch-shaped TENG, the inset is the photograph of a typical arch-shaped TENG device.

2.2.1 Fabrication of PDMS Film with Pyramid Patterns

As reported in previous study, the microscale pyramid structures on PDMS surfaces can help to increase the triboelectric charge density compared to the flat PDMS surface. Thus, we made the pyramid patterned PDMS film as the bottom triboelectric layer in this arch-shaped TENG.

The fabrication process starts from photolithographic patterning of 4 in. (100) Si wafers (Fig. 2.2a) with thermally grown SiO_2 on top. The patterned wafer with the array of square window openings was firstly etched by buffered-oxide-etching process to transfer the pattern onto the SiO_2 layer. Then, the wafer was etched in KOH solution to fabricate the recessed features of pyramid (Fig. 2.2b). After cleaned with acetone, isopropanol and ethanol in sequence, the Si molds were treated with trimethylchlorosilane (Sigma Aldrich) by gas phase silanization to enable the easy peel-off of the PDMS film from the Si mold in the following step. In preparing the patterned PDMS film, the elastomer and the cross-linker (Sylgard 184, Dow Corning) were mixed in a 10:1 ratio (w/w), and then casted on the Si mold. After the degassing process under the vacuum, the mixture was spin-coated on the Si mold at 500 rpm for 60 s (Fig. 2.2c). After the thermally curing process at 85 °C for 1 hour, the PDMS inked with pyramid patterns was peeled off from Si mold (Fig. 2.2d).[42] The surface without patterns will be glued to the inner surface of the bending Kapton substrate.

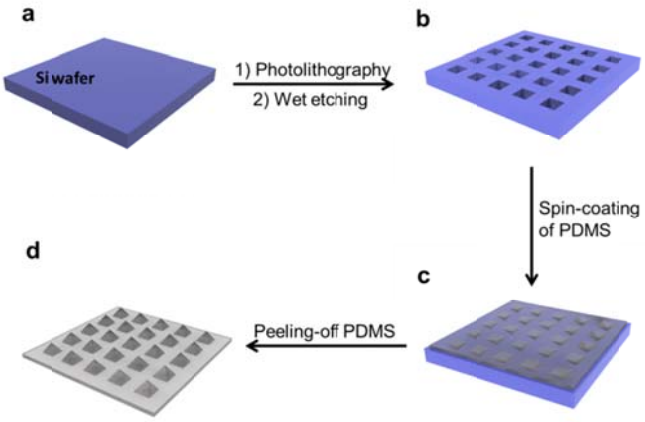

Figure 2.2 Schematic fabrication process flow of the pyramid-patterned-PDMS film. (a) The (100) Si wafer used to fabricate the mold for PDMS casting. (b) After the sequence of photolithography and wet etching, the Si wafer was patterned with array of recessed features of pyramids. (c) The PDMS mixture of elastomer and cross-linker was spin-casted onto the Si mold. (d) The thermally cured PDMS film was peeled off the Si mold to get the PDMS film with patterned pyramid features on the surface.

2.2.2 Fabrication of the Arch-Shaped TENG.

The unique arch-shaped structure of the TENG from the naturally-bent top plate, which helps to carry out the action of effective charge separation and contact using the elasticity of the film, is achieved by the following innovative fabrication process (Fig. 2.3): The top part starts from a piece of flat Kapton film (Fig. 2.3a<i>). A layer of 500-nm SiO_2 film is deposited using plasma-enhanced chemical vapor deposition (PECVD) at 250 °C (Fig. 2.3a<ii>). Upon cooling down to room temperature, the Kapton will shrink to a much larger extent than the SiO_2 film because of the large difference in thermal expansion coefficients, so that thermal stress across the interface will make the plate bent naturally towards the SiO_2 side (the curvature is calculated in Supplementary Discussion S1). Then, the pre-fabricated PDMS film with pyramid patterns is glued to the inner surface through a thin PDMS bonding layer (Fig. 2.3a<iii>). Finally, the electrode is

deposited on top (Fig. 2.3a<iv>). As for the bottom plate, an aluminum foil (Fig. 2.3b<i>) is patterned with a typical photolithography process: defining the photoresist to the array of square windows (Fig. 2.3b<ii>); depositing a layer of aluminum on top (Fig. 2.3b<iii>), and finally lift-off, leaving the patterned Al cubes on the foil (Fig. 2.3b<iv>). At last, the two as-fabricated plates of the same size are attached face to face and sealed at the two ends. The soft Al plate will be forced to bend outward under the contraction from the other plate, so that a gap will form naturally in between.

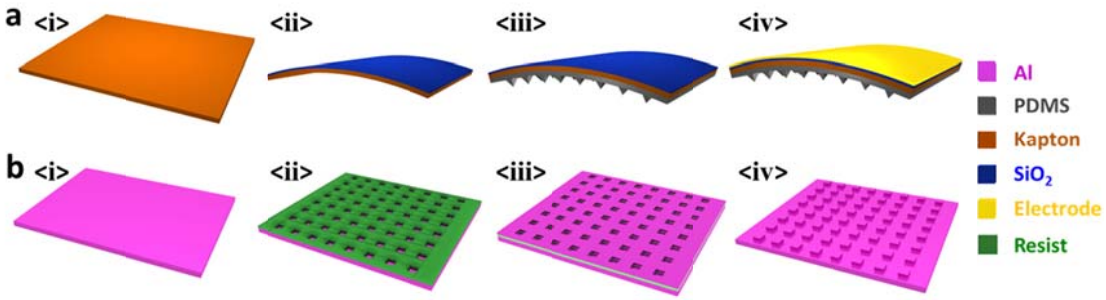

Figure 2.3 Fabrication process of the arch-shaped TENG. (a) The top plate; (b) the bottom plate of the TENG.

The patterned surfaces of PDMS film (Fig. 2.4a) and Al foil (Fig. 2.4b) are fabricated to enhance the triboelectric charging and are characterized using scanning electron microscopy (SEM). Both the arrays are uniform and regular across a very large area.

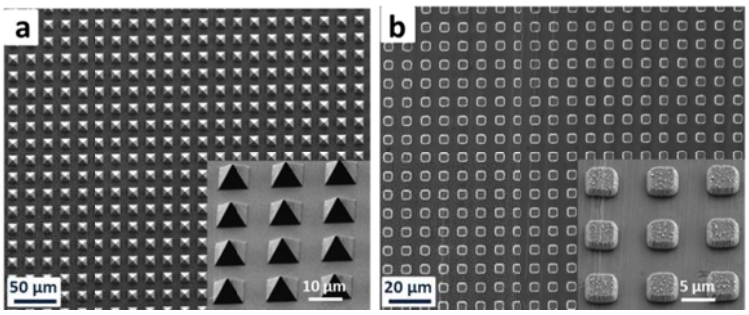

Figure 2.4 Top view SEM images of (a) the PDMS surface with pyramids patterns and (b) Al surface with cubic patterns, the insets are high-magnification images in tilted angle.

2.3 Theoretical Study on the Working Mechanism of the Dielectric-Metal Arch-Shaped TENG

Because this is the first TENG based on the triboelectrification between a metal and a dielectric layer, in which the metal not only serves as the triboelectric layer but also acts as the electrode itself, the detailed mechanism including the charge transfer behavior will be different from the previously demonstrated TENGs based on the triboelectrification between two dielectric layers. Thus, we utilized the both finite-element simulation and analytical derivation to illustrate working principle the dielectric-metal based TENG.

2.3.1 Finite-Element Simulation of the Arch-Shaped TENG

The operation of the arch-shaped TENG is realized by applying a cycled compressive force onto the whole area of the device, so that the bending plates will be periodically pressed to flatten and contact closely with each other. Once released, the two plates will separate apart due to the stored elastic energy and revert instantaneously back to their original arch shape due to resilience. The working principle of the polymer-metal TENG is schematically depicted in Figure 2 using the numerically simulated electrostatic potential distribution arising from triboelectric charges (using COMSOL package). These semi-quantitative results show that a cycled generation of the potential difference between the two electrodes drives the flow of electrons through an external load. At the original state before the contact of the triboelectric films (Fig. 2a), there is no charge transferred, thus no electric potential. Upon the pressing of the two films towards each other, they will be brought into fully surface contact and possibly relative sliding would occur, which results in electrons transfer from a material in the positive side of the triboelectric series to the one in the negative side in the series. Accordingly, electrons will be injected from Al to PDMS surface, leaving positive charges on Al foil. Previous theoretical study on triboelectricity reveals that such charge transfer process will continue

in the first few hundreds of cycles until the accumulated charges reach a saturation and equilibrium; the negative charges will preserve on the PDMS surface due to the nature of insulator.[59] But the positive triboelectric charges on the conductive Al foil would attract the electrons in the opposite electrode to flow through external load, which is the observed current in this case. This process is different from the mechanism proposed for the polymer-polymer based TENG.[44] After cycles of deformation, when the device is pressed and the surfaces with charges are in close contact with each other, all of the triboelectric charges will stay on the inner surfaces with the same surface density (σ_0) (Fig. 2b). Thus, these charges with opposite signs will be virtually in the same plane, and there will be little potential difference across the two layers due to the negligible charge separation. Once the pressing force is released, the TENG will immediately rebound back to its original arch shape due to the elasticity of the film so that a gap will form again between the two plates. From the numerical simulation result, if the charge transfer has not happened at the moment, the electric field generated by the separated surface charges will give rise to a much higher potential on the Al foil side than the top electrode (TE) (Fig. 2c). Such a potential difference will drive the flow of positive charges from Al foil to TE through the external load until the potential difference is fully offset by the transferred charges, rendering the TE with a surface charge density of ($\Delta\sigma$), while the Al is left with ($\sigma_0-\Delta\sigma$) (Fig. 2d). Subsequently, when the TENG is pressed again to reach the close contact of the two plates, these redistributed charges will inversely build a positive potential on TE (Fig. 2e), which will drive all of the transferred charges ($\Delta\sigma$) to flow back to the inner surface of the Al foil. Then a cycle is achieved and the device will go back to the equilibrium state depicted in Figure 2b. This is a full cycle of electricity generation.

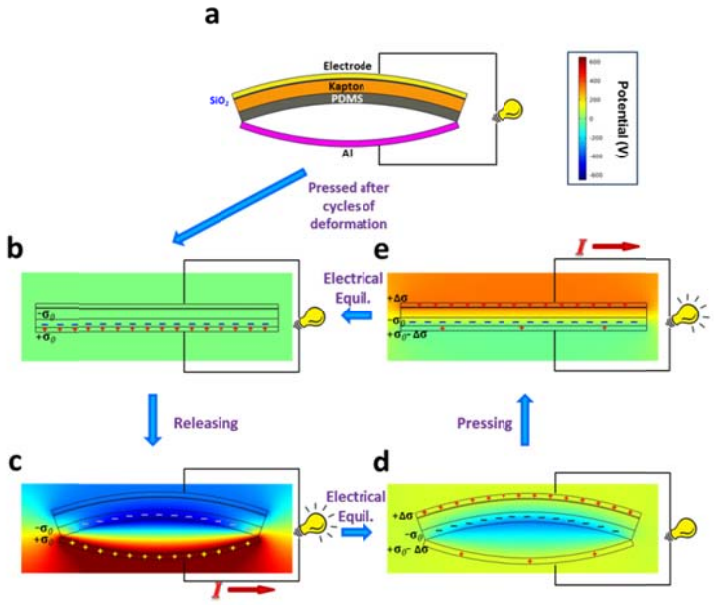

Figure 2.5 The finite-element simulated working principle of the polymer-metal based TENG. (a) A two-dimensional sketch showing the initial state of the TENG before any deformation. (b-e) The finite element simulation of the periodic potential change between the two electrodes upon cyclic deformation, showing the driving force for the back-and-forth charge flow generated by the TENG. A cycle is generally divided into four states, (b) device under pressing, (c) deformation released, (d) charges transferred, and (e) device gets pressed again, and finally charge transferred again to cycle back to (b).

2.3.2 Analytical Derivation of Charge Transfer Behavior

From the above simulation result, we can easily tell that both the voltage and current outputs are related to the amount of charges transferred ($A\Delta\sigma$, A is surface area of the plate), which is determined by the triboelectric charge density (σ_0) and the separation distance of the two plates. As σ_0 is regarded as a constant, we did an analytical calculation based on the simplified model of quasi-infinite flat plates (Fig. 2.6a), to give an idea on the magnitude of the distance required for the optimum output.

As for the infinite plane with surface charge of density σ, the generated electric field in the medium with the relative permittivity of ε_r is:

$$E = +\frac{\sigma}{2\varepsilon_0\varepsilon_r} \tag{2.1}$$

the direction is pointing outward away from the charges.

If there are several planes with charges in the space, then the voltage drop between two points will be:

$$\Delta V = \sum_i \sum_k E_{ik} d_k \tag{2.2}$$

E_{ik} is the electric field generated by i^{th} charge plane in k^{th} medium, d_k is the thickness of k^{th} medium.

So in the model of the TENG shown in Figure 2.6a, the voltage drop from bottom electrode to top electrode will be:

$$\begin{aligned}\Delta V_{BE\to TE} = &\left[+\frac{\sigma_0-\Delta\sigma}{2\varepsilon_0}d + \frac{\sigma_0-\Delta\sigma}{2\varepsilon_0\varepsilon_{rPDMS}}t_{PDMS} + \frac{\sigma_0-\Delta\sigma}{2\varepsilon_0\varepsilon_{rK}}t_K + \frac{\sigma_0-\Delta\sigma}{2\varepsilon_0\varepsilon_{rSiO_2}}t_{SiO_2}\right] \\ &+\left[-\frac{(-\sigma_0)}{2\varepsilon_0}d + \frac{-\sigma_0}{2\varepsilon_0\varepsilon_{rPDMS}}t_{PDMS} + \frac{-\sigma_0}{2\varepsilon_0\varepsilon_{rK}}t_K + \frac{-\sigma_0}{2\varepsilon_0\varepsilon_{rSiO_2}}t_{SiO_2}\right] \\ &+\left[-\frac{\Delta\sigma}{2\varepsilon_0}d - \frac{\Delta\sigma}{2\varepsilon_0\varepsilon_{rPDMS}}t_{PDMS} - \frac{\Delta\sigma}{2\varepsilon_0\varepsilon_{rK}}t_K - \frac{\Delta\sigma}{2\varepsilon_0\varepsilon_{rSiO_2}}t_{SiO_2}\right] \\ = &\frac{\sigma_0}{\varepsilon_0}d - \frac{\Delta\sigma}{\varepsilon_0}\left(d + \frac{t_{PDMS}}{\varepsilon_{rPDMS}} + \frac{t_K}{\varepsilon_{rK}} + \frac{t_{SiO_2}}{\varepsilon_{rSiO_2}}\right)\end{aligned} \tag{2.3}$$

where d is the planar separation distance of the two plates. If we assume:

$$t = \frac{t_{PDMS}}{\varepsilon_{rPDMS}} + \frac{t_K}{\varepsilon_{rK}} + \frac{t_{SiO_2}}{\varepsilon_{rSiO_2}} \tag{2.4}$$

Then, $\Delta V_{BE\to TE} = \frac{\sigma_0}{\varepsilon_0}d - \frac{\Delta\sigma}{\varepsilon_0}(d+t)$ (2.5)

When the charge transfer reaches equilibrium, $\Delta V_{BE\to TE} = 0$, so we can get from the above equation that:

$$\frac{\Delta\sigma}{\sigma_0} = \frac{d}{d+t} \tag{2.6}$$

According to the parameters of these three layers of dielectric layers ($t_{PDMS} = 100\ \mu m$, $t_K = 125\ \mu m$, $t_{SiO_2} = 0.5\ \mu m$ as thicknesses of PDMS layer, Kapton layer, and SiO_2 layer, respectively, and $\varepsilon_{rPDMS} = 2.6$, $\varepsilon_{rK} = 3.5$, $\varepsilon_{rSiO_2} = 4.2$ are relative permittivity of PDMS layer, Kapton layer, and SiO_2 layer, respectively), we can get $t = 74.29\ \mu m$.

Using this value and Equation (2.6), we can depict the curve of $\Delta\sigma/\sigma_0$ *vs.* d, as shown in Fig. 2.6b. We can see that, when the separation distance starts to increase from 0 to 0.7 mm, $\Delta\sigma$ keeps a very rapid increase from 0 to ~90% of σ_0. Then, the slope of this curve starts to decrease. Thus, it can be concluded that both an intimate contact and a subsequent separation of nearly 1 mm are required for the phenomenal transferring of charges. This is just the unique innovation and advantage of the purposely designed arch-shaped structure, which introduces sufficient resilience for separating the plates but without sacrificing the intimate contact and electrification.

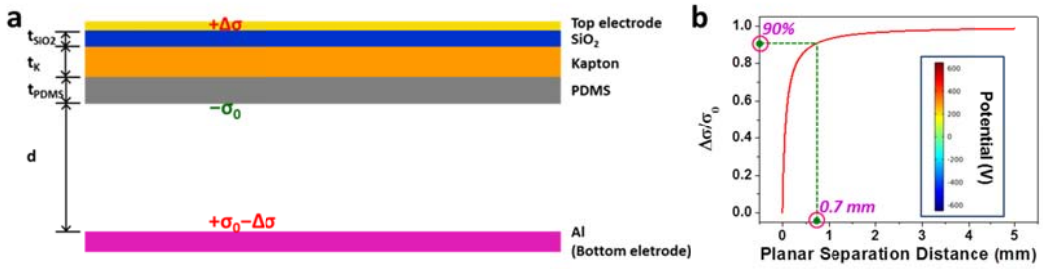

Figure 2.6 The analytic study of the arch-shaped TENG. (a) The schematic diagram showing the quasi-infinitely large plane model of the TENG. (b) The relationship of the ratio between transferred charge density ($\Delta\sigma$) and triboelectric charge density (σ_0), with the planar separation distance, which shows the importance of the effective charge/plate separation.

2.4 Electrical Output of the Arch-Shaped TENG

Triggered by periodic pressing to flatten the arch-shaped TENG, the electric output measurement was performed on a typical device in a size of 3 cm×2.8 cm, with the

triggering frequency of 6 Hz and controlled amplitude. Since the accumulation of the triboelectric charges increases and reaches equilibrium in a certain period of time after multiple cycles, the output will gradually go up in the first stage upon deformation. Then, the open-circuit voltage (V_{OC}) will stabilize at 230 V (Fig. 2.7a), measured by an electrometer with infinite input resistance. From the inset of Figure 3a, when the bottom Al is connected to the positive probe of the electrometer, upon the release of the pressing force a positive voltage is generated because of the immediate charge separation. Since in an open-circuit condition the electrons cannot flow to screen the induced potential difference between the two electrodes, the voltage will hold at a plateau until the subsequent pressing deformation in the second half cycle. As shown in Figure 2.7b, the peak value of the short-circuit current (I_{SC}) reaches 94 μA, corresponding to the half cycle of pressing that is in higher straining rate than releasing. The integration of the each current peak gives the total charges transferred in a half cycle of deformation. Moreover, when the connection polarity to the electrometer is switched, both the voltage and current signal will be completely reversed. The gap from the arch-shaped structure is a key factor for the enhanced output, because without the SiO_2-film-introduced bending, there will be much smaller and unstable electrical output (Figs. 2.7 c&d).

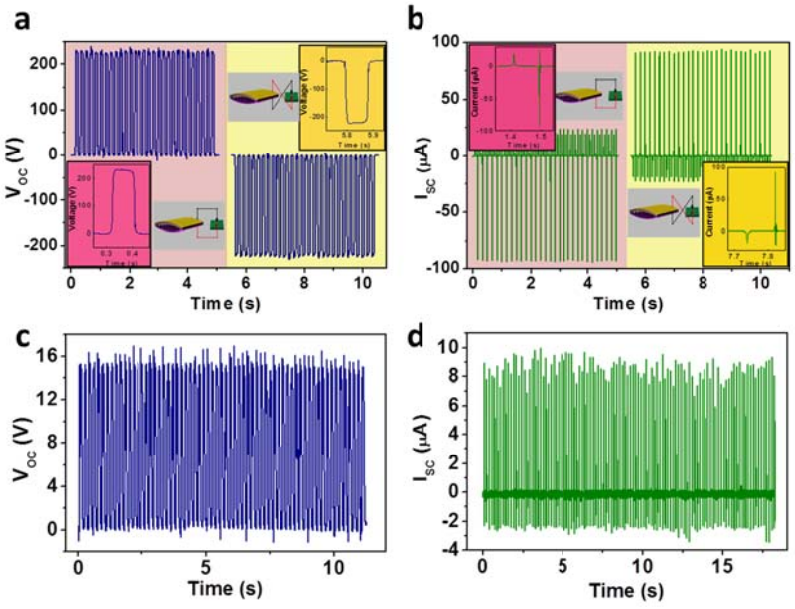

Figure 2.7 Characterizing the performance of the arch-shaped TENG and the comparison with a TENG without the presence of the arch-shape. (a) The open-circuit voltage and (b) the short-circuit current of the TENG under the deformation frequency of 6 Hz. These are studies under both the forward connection (Al connected to the positive probe) shown at the left-hand side and reverse connection shown at the right-hand side. The insets are the magnified output curve in one cycle, and the sketch of the corresponding connection polarity. (c) The open-circuit voltage and (d) the short-circuit current.

Besides the triboelectric charge density and the separation distance of the two plates, another factor that could make an influence on the output of the TENG is the deformation frequency, which affects the straining rate. Since the mechanical energy from the environment is always irregular and varies in frequencies, it is necessary to study the dependence of TENG's output on the frequency. Thus, we tested the TENG device in a series of 9 different frequencies, from 2 to 10 Hz, with the amplitude of the triggering motor remaining constant. As shown in Figure 2.8a, V_{OC} almost remains the same at different frequencies. The probable reason is that at the open-circuit condition, it doesn't involve the dynamic process of charge transfer. The voltage is only determined by the triboelectric charge density and the plate separation at any given time. But for the short-circuit current, it presents a very clear increasing trend with the increase of frequency, from 35 μA at 2 Hz to 130 μA at 10 Hz (Fig. 2.8b), because the deformation rate increases with deformation frequency, which leads to a higher flow rate of charges, i.e., higher current, but the total amount of charges transferred is constant at given triboelectric condition and separation distance. This is confirmed by the integration of every single current peak from each of the 9 different frequencies (inset of Fig. 2.8b). Therefore, the instantaneous power output increases with the increase of frequency, so that it will be more eligible to drive electronic devices with larger power consumption. From the above results, when the frequency reaches 10 Hz, the instantaneous power output reaches up to 3.56 mW/cm^2 and 128 mW/cm^3.

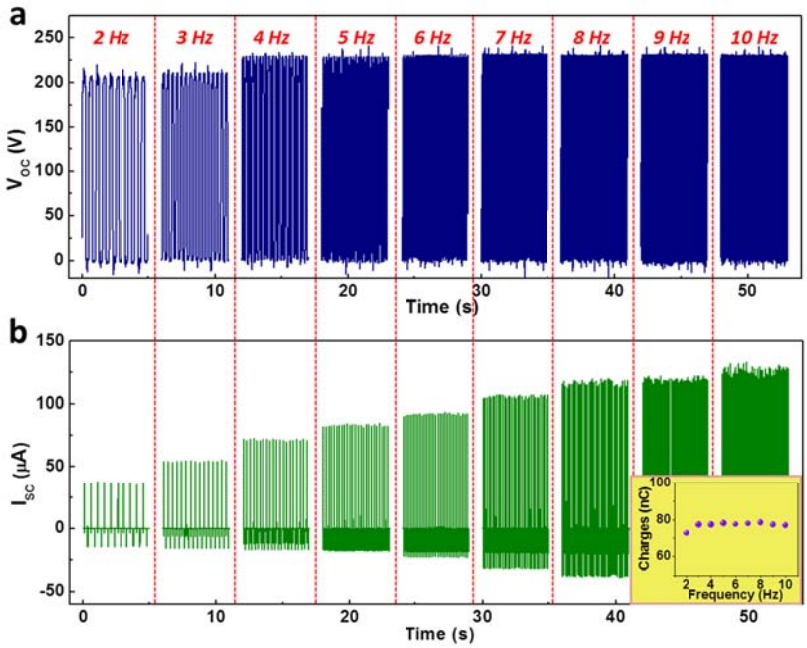

Figure 2.8 The influence of the deformation frequency on (a) the open-circuit voltage and (b) the short-circuit current. The inset in (b) is the integration of a single current peak from each frequency, which gives the total charges transferred in a half cycle, showing that the total contact charges generated is almost independent of the deformation frequency.

2.5 Study of the Vertical Contact-Mode TENG as Direct Power Source

The goal of the development of nanogenerators is to drive electronic devices by harvesting small-scale mechanical energy, so that the self-powered system can be realized. As for the energy conversion devices such as TENGs, there are generally two methodologies for them to be used as a power source. The first choice is to power devices directly using the pulses generated by TENGs, such as a chemical sensor[34] and a LCD[54,71]. In practice, the output power to the load depends on the match between the load and the power source. Thus, it is highly desirable to both experimentally study and theoretically understand the characteristics of the contact-mode TENG (e.g. the arch-shaped TENG) as the direct power source for external load.

2.5.1 Experimental Study and Demonstration of the Arch-Shaped TENG as a Direct Power Source

When the TENG is connected to an external load with certain resistance, both the voltage and the current on the load will deviate from V_{OC} and I_{SC} respectively. Thus, it is necessary to study the relationship of the voltage and current with the resistance of the external load. For the study of this relationship, we connected a working arch-shaped TENG (under frequency of 6 Hz) the loads of different resistances. From this experiment, we found that the current through the load will generally decrease from I_{SC} when the resistance increases from zero (Fig. 2.9a), but the voltage across the load will follow an opposite trend and saturate to V_{OC} when the resistance gets infinitely large. The instantaneous power on the load will reach the maximum value of 9 mW at a load resistance of ~3 MΩ (Fig. 2.9b).

In the other case, when the TENGs are used to drive polar devices such as diodes, the AC signals of the NG needs to be rectified before connected to the load. We can find that both the rectified voltage and current follow a similar trend (Fig. 2.9c) with the scenario of no rectification, and the only difference is that the voltage will not saturate but continues to increase as the load resistance above 100 MΩ. The maximum output power is 7.2 mW at a load of ~2 MΩ (Fig. 2.9d), which is a bit smaller than the maximum power of 9 mW without rectification, simply because of the energy loss of the rectifier unit.

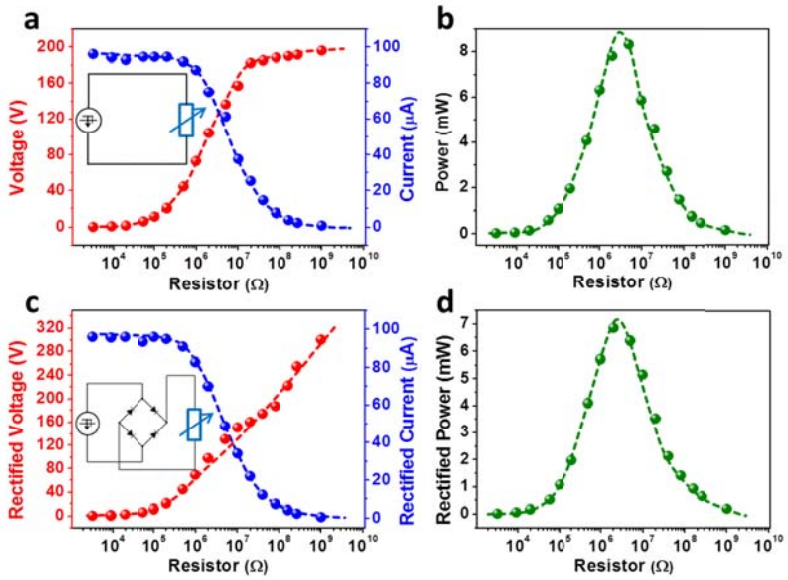

Figure 2.9 Characteristics of the arch-shaped TENG as a direct power source to drive electronic devices. (a-b) When the TENG driving a load without rectification, the dependence of (a) the output voltage, current and (b) instantaneous power on the load resistance. (c-d) When the TENG driving a load with rectification, the dependence of (c) the output voltage, current and (d) instantaneous power on the resistance of the load. All of the dots are measured values and the solid lines are fitted curves.

As a representative example of serving as a direct power source, the arch-shaped TENG with the large instantaneous electrical output was for the first time used to continuously drive LEDs. The real-time current signals flowing through the LED is given in Figure 2.10a. In comparison with the characteristic *I-V* curve of the LED, the peak current of 100 μA is way sufficient to turn the LED on. Figure 2.10b shows snapshots taken from a flashing LED. Each instant of lighting-up corresponds to a large peak of the output current. In coordination with the TENG's output characteristics discussed above, the resistance of the LED in "on" state is only about 23 kΩ, far below the range (1 MΩ to 100 MΩ) of rapid change of the current, so the current is almost the same as I_{SC}, but the voltage on the LED is only ~2.5 V. From Figure 4b, because the resistance of such a single LED is far below the maximum power point, TENG can also drive the flashing of

up to 50 LEDs connected in series (Fig. 2.10c) which only results in less than 5% decrease of the current. This demonstration clearly illustrates the ability of the TENG as a direct power source to continuously drive regular electronic devices.

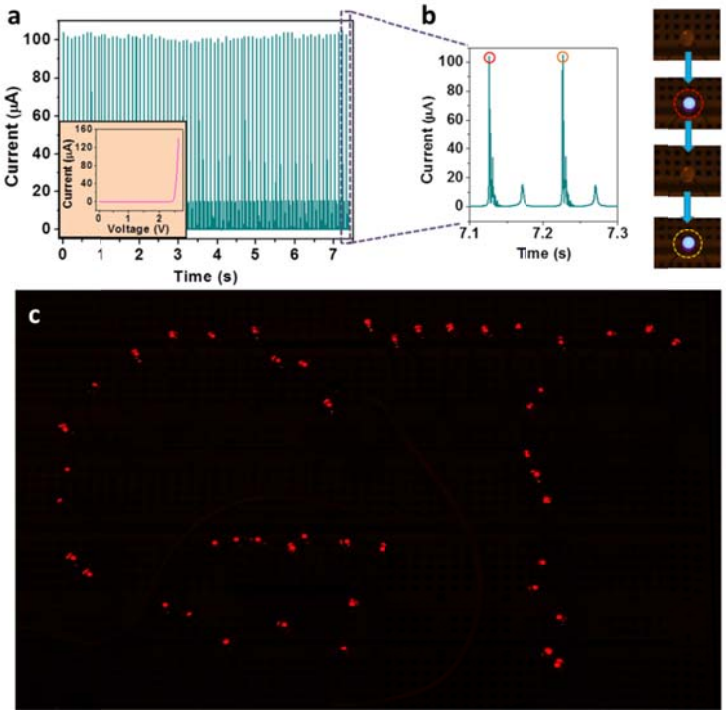

Figure 2.10 Demonstration of the arch-shaped TENG as a direct power source for LEDs. (e) The current through a LED driven by a rectified TENG under 8 Hz. The inset is the characteristic I-V curve of the LED. (f) The snapshots of the TENG-driven flashing LED, corresponding to the magnified current peaks. (c) The instantaneous flashing of 46 red LED connected in series, which is directly driven by a single triboelectric nanogenerator device.

2.5.2 Theoretical Study of the Contact-Mode TENG as a Direct Power Source

According to our derivation in Equation (2.5), the instantaneous voltage (V) between the two electrodes has the following relationship with the separation distance ($x(t)$) of the two triboelectric layers and the instantaneous transferred charge (Q) between the two plates:

$$V = -\frac{Q}{S\varepsilon_0}\big(d_0 + x(t)\big) + \frac{\sigma x(t)}{\varepsilon_0} \tag{2.7}$$

where $d_0 = \sum_i \frac{d_i}{\varepsilon_{ri}}$, d_i and ε_{ri} is the thickness and relative permittivity of each dielectric layer in the TENG structure; S is the surface area of the electrode, and σ is triboelectric charge density. This equation showing the relationship among V-Q-x is the basic equation for the contact-mode TENG and can be utilized to calculate its output property when driving a load with a resistance of R.[72]

First, two special cases of open-circuit (OC) condition and short-circuit (SC) condition are analyzed. At OC condition, there is no charge transfer, which means that Q is 0. Therefore, the open-circuit voltage V_{OC} is given by:

$$V_{OC} = \frac{\sigma x(t)}{\varepsilon_0} \tag{2.8}$$

At SC condition, V is 0. Therefore, the transferred charges are

$$Q_{SC} = \frac{S\sigma x(t)}{d_0 + x(t)} \tag{2.9}$$

$$I_{SC} = \frac{dQ_{SC}}{dt} = \frac{S\sigma d_0}{(d_0 + x(t))^2}\frac{dx}{dt} = \frac{S\sigma d_0 v(t)}{(d_0 + x(t))^2} \tag{2.10}$$

In general cases that a contact-mode TENG is connected with an arbitrary resistor R, the output properties can be estimated by combining Equation (2.7) with the Ohm's law:

$$V = IR = R\frac{dQ}{dt} \tag{2.11}$$

Merging Equation (2.11) into Equation (2.7), we can have:

$$R\frac{dQ}{dt} = -\frac{Q}{S\varepsilon_0}\big(d_0 + x(t)\big) + \frac{\sigma x(t)}{\varepsilon_0} \tag{2.12}$$

In the separating process of the two plates starting from t = 0, we have the boundary condition of:

$$Q(t = 0) = 0 \tag{2.13}$$

Then Equation (2.12) can be solved analytically as:

$$Q(t) = \sigma S - \sigma S\, exp[-\frac{1}{RS\varepsilon_0}(d_0 t + \int_0^t x(t)dt)] - \frac{\sigma d_0}{R\varepsilon_0} exp[-\frac{1}{RS\varepsilon_0}(d_0 t + \int_0^t x(t)dt)] \times$$

$$\int_0^t exp\left[\frac{1}{RS\varepsilon_0}\big(d_0 z + \int_0^z x(z)dz\big)\right] dz \tag{2.14}$$

Therefore, the current and voltage output can be derived as:

$$I(t) = \frac{dQ}{dt} =$$

$$-\frac{\sigma d_0}{R\varepsilon_0} + \frac{\sigma(d_0+x(t))}{R\varepsilon_0} exp[-\frac{1}{RS\varepsilon_0}(d_0 t + \int_0^t x(t)dt)] + \frac{\sigma d_0}{R\varepsilon_0} \times \frac{d_0+x(t)}{RS\varepsilon_0} exp[-\frac{1}{RS\varepsilon_0}(d_0 t +$$

$$\int_0^t x(t)dt)] \times \int_0^t exp\left[\frac{1}{RS\varepsilon_0}\left(d_0 z + \int_0^z x(z)dz\right)\right] dz \quad (2.15)$$

$$V(\mathrm{t}) = RI(t) =$$

$$-\frac{\sigma d_0}{\varepsilon_0} + \frac{\sigma(d_0+x(t))}{\varepsilon_0} exp[-\frac{1}{RS\varepsilon_0}(d_0 t + \int_0^t x(t)dt)] + \frac{\sigma d_0}{\varepsilon_0} \times \frac{d_0+x(t)}{RS\varepsilon_0} exp[-\frac{1}{RS\varepsilon_0}(d_0 t +$$

$$\int_0^t x(t)dt)] \times \int_0^t exp\left[\frac{1}{RS\varepsilon_0}\left(d_0 z + \int_0^z x(z)dz\right)\right] dz \quad (2.16)$$

In a special case of uniform motion at a constant velocity (v), the above equations can be further simplified to Equations (2.17-19), as shown below.

$$Q(t) = \sigma S[1 - exp(-At - Bt^2) + \sqrt{2}Fexp(-At - Bt^2) \times Dawson\left(\frac{F}{\sqrt{2}}\right) - \sqrt{2}F \times$$

$$Dawson(\frac{F}{\sqrt{2}} + \sqrt{B}t)] \quad (2.17)$$

$$I(t) = \sigma S[exp(-At - Bt^2)(A + 2Bt) - \sqrt{2}F \times exp(-At - Bt^2)(A + 2Bt) \times$$

$$Dawson\left(\frac{F}{\sqrt{2}}\right) - A + 2A(\frac{F}{\sqrt{2}} + \sqrt{B}t) \times Dawson(\frac{F}{\sqrt{2}} + \sqrt{B}t)] \quad (2.18)$$

$$V(t) = \sigma SR[exp(-At - Bt^2)(A + 2Bt) - \sqrt{2}F \times exp(-At - Bt^2)(A + 2Bt) \times$$

$$Dawson\left(\frac{F}{\sqrt{2}}\right) - A + 2A(\frac{F}{\sqrt{2}} + \sqrt{B}t) \times Dawson(\frac{F}{\sqrt{2}} + \sqrt{B}t)] \quad (2.19)$$

The constants A, B, and F are defined by:

$$A = \frac{d_0}{RS\varepsilon_0} \quad (2.20\text{-}1)$$

$$B = \frac{v}{2RS\varepsilon_0} \quad (2.20\text{-}2)$$

$$F = \frac{A}{\sqrt{2B}} = \frac{d_0}{\sqrt{RS\varepsilon_0 v}} \quad (2.20\text{-}3)$$

The Dawson's integral (*Dawson(x)*)[73,74] in the above expressions is shown as:

$$Dawson(x) = exp(-x^2) \int_0^x exp(y^2)\, dy \quad (2.21)$$

In real experimental cases, the movement of the top plate always has a maximum distance (x_{max}). Thus, the relationship between x and t in such uniform movement with the velocity of v can be expressed as Equation (2.22). From this, the numerical calculation results can be obtained by specifying the parameters, which are shown in Table 1.

$$x = vt \ \left(t < \frac{x_{max}}{v}\right) \tag{2.22-1}$$

$$x = x_{max} \ \left(t \geq \frac{x_{max}}{v}\right) \tag{2.22-2}$$

Dielectric 1	Metal, $d_1 = 0$ μm
Dielectric 2	$d_2 = 125$ μm, $\varepsilon_{r2} = 3.4$
Area size of Dielectrics S	58.0644 cm^2 (9 $inch^2$)
Tribo-charge surface density σ	10 μC/m^2
Maximum separation distance x_{max}	0.001 m
Average Velocity v	0.1 m/s

Table 2.1 Parameters utilized in the constant velocity theoretical calculation.

The real-time output properties for a contact-mode TENG is plotted in Figure 2.11 with different load resistances. The detailed profiles of the charge, current, and voltage relationships at different loads are shown in Figures 2.11a-c. At SC condition, the charge transfers at the fastest speed. For a relatively small R, Q can still get its saturation value when the top electrode stops moving (t= 10 ms). However, when R is more than 100 MΩ, at t= 10 ms, the charge cannot get saturated due to the limit charge transfer rate by the resistor, resulting in the unstopped charge transfer from metal 1 to metal 2 after t= *10 ms*. Therefore, the current is a peak-shape when R is small while the current continues increasing during the plate movement when R is large. The voltage has the same profile with the current, but a different trend in magnitude. The peak values of the voltage, current and power on different loads are displayed in Figures 2.11d and e. It can be clearly observed that the operation of the TENG can be divided into three working

regions. First, In Region I where the resistance is low (0.1-1000 Ω), the peak current has little drop from the SC condition, which is due to the similar charge transfer process in comparison with that of the SC condition. As a result, the maximum voltage is approximately proportional to the external resistance. On the other hand, when the resistor is larger than 1 GΩ (Region III), the output characteristics are close to the OC condition, in which the maximum voltage saturates at V_{OC}. The medium range of the resistance is Region II, where the maximum current drops dramatically but the maximum voltage increases at a reverse trend. Around 100 MΩ inside this region, the TENG reaches its maximum instantaneous output power. The general shape of these analytical calculated results match very well with the experiment results obtained from the arch-shaped TENG shown in Figure 2.9.

This unique output characteristic of TENG can be interpreted both physically and mathematically. Physically, the working principle of the TENG is a conjunction of the triboelectric process and the electrostatic induction. When the tribo-charges are separated, an induced voltage will be generated between the two electrodes, which will drive the electrons to flow from metal electrode 2 to metal electrode 1. The electric field from these transferred charges will screen the original electric field from the tribo-charges. The charge accumulation rate at SC condition is the maximum charge transfer rate. If there is an external load with certain resistance, the resistor will limit the real charge transfer rate, making it lower than that at the SC condition. When the load resistance is very small, this limitation is not obvious so that the rate can still catch up with the maximum rate, enabling the Q to stay close to Q_{SC} in Region I. When the load resistance continues to increase and gets into Region II, it begins to significantly limit the charge flow rate, making the charge accumulation curve deviate downward from Q_{SC}. As the load resistance is large enough, the transfer of electrons from metal 2 to metal 1 is rather slow, which results in a very small current. The induced voltage between the two electrodes

will hold for a long time due to the limited screening effect, with the magnitude approaching V_{OC}. This is the Region III of the TENG.

Mathematically, this can be interpreted from the behavior of the Dawson's integral. When R is small, the parameters F and B (as defined in Equation 20) are approaching infinity. In this region, using the first-order asymptotic series of the Dawson's integral, the following approximate equation can be obtained.[72]

$$I(t) = \frac{\sigma v A}{R\varepsilon_0(A+2Bt)^2} = \frac{\sigma v d_0 S}{(d_0+vt)^2} \tag{2.23}$$

This is just the same equation with I_{SC}. Therefore, within this region satisfying the first-order asymptotic series (Region I), the behavior of the charge transfer (i.e. the current) remains similar with that of the SC condition.

When R is very large, the parameters F and B are close to 0. At this time, the Dawson's integral can be approximated by its first-order Maclaurin series and the following equation can be obtained.[72]

$$V(t) = \frac{\sigma v t}{\varepsilon_0} \tag{2.24}$$

This is the expression of the V_{OC}, so the TENG is now in the quasi-OC condition, which is the Region III.

When R is neither too large nor too small, the behavior of the TENG is in the transitional region between SC and OC conditions (Region II), within which the maximum power is reached, as shown in Figure 2.11f.

In this unique output characteristic of the TENG, the instantanous power (P_{max}) reaches the maximum value at a certain resistance, which can be termed as the optimum resistance (R_{opt}). P_{max} can be obtained as $P_{max} = I_{max}^2 R$, in which I_{max} is the peak value of the current at a certain resistance of R. Thus, R_{opt} satisfies the following equation:

$$\frac{\partial P_{max}}{\partial \mathrm{R}} = 0 \tag{2.25}$$

Through mathematic derivation,[72] we can get the approximate expression for R_{opt}:

$$R_{opt} \approx \frac{(d_0+x_{max})^2}{Sv\varepsilon_0} \tag{2.26}$$

Thus, the optimum resistance of a contact-mode TENG related to the structure parameters (d_0, S) and movement mode (v, x_{max}). When designing a TENG as a direct power source for certain electronics, it is very important to match the optimum resistance of the TENG with the actual resistance of the load, so that we could have the best output power from a TENG.

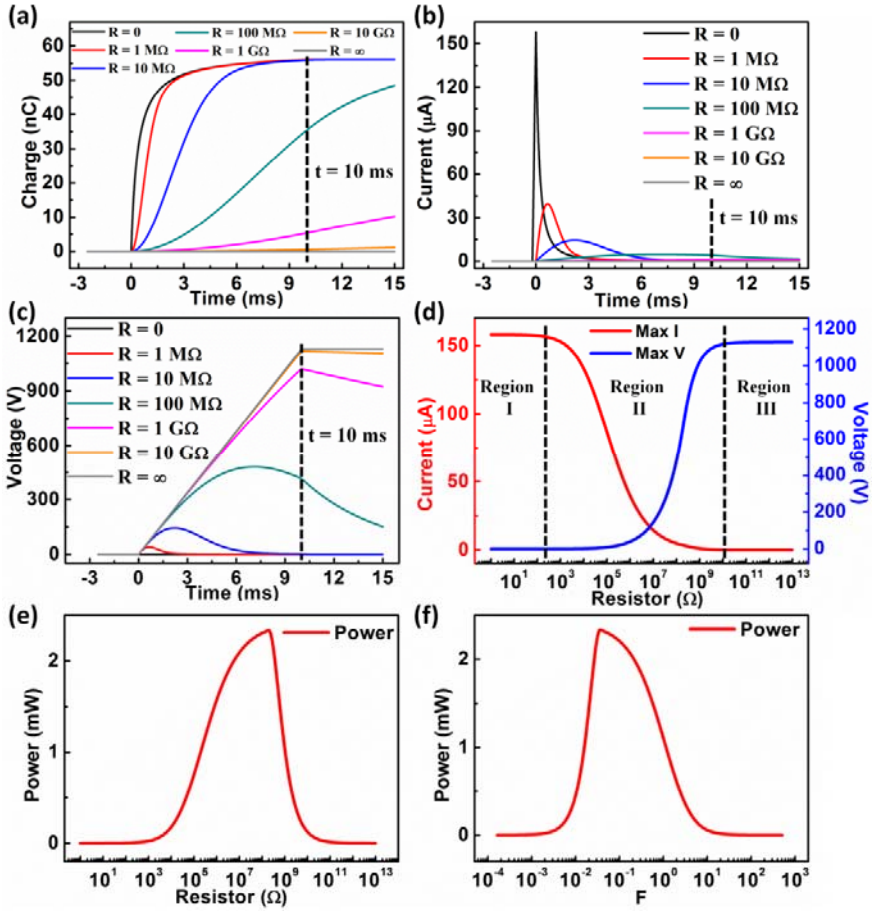

Figure 2.11 Calculated output characteristics of a contact-mode TENG when the plates are separated at a uniform velocity. The top plate reaches the maximum separation distance and stops moving at t = 10 ms. (a) Real-time transferred charge-time relationship at different load resistances. (b) Real-time current-time relationship at different load resistances. (c) Real-time voltage-time relationship at different load resistances. (d) The influence of the load resistance on the magnitude of the output current and voltage. Three working regions are marked. (e) The

influence of the load resistance on the instantaneous power output. (f) The influence of the defined F parameter on the instantaneous power output.

2.6 Construction of a Power Source Module Using the Arch-Shaped TENG and Li-Ion Battery

In many cases, the AC pulses from the nanogenerators may not directly satisfy the need of some electronic devices/systems, either because of the requirement for a constant DC current, or the higher power consumption than that generated by a single device. Thus, the output power needs to be regulated with an energy storage unit and a rectifier[15]. As for the energy storage device, lithium ion batteries (LIBs) are the most widely used and promising choice.[24,60] As the output (especially the current) from the arch-shaped TENG has reached the level to match the capacity of a LIB and overcome the self-discharge current, it will be feasible to use a TENG to charge a LIB. The electrical circuit of such a power source module is shown in Figure 2.12a. At the standby mode, the LIB is continuously charged by a TENG through a rectifier and is disconnected from the load (switch S1 on; S2 off). When enough charges have been stored, the module will move on to the active mode, in which the battery will be disconnected from the TENG charger (S1 off) and start to power the system (S2 on). Such power source module is demonstrated using a home-made LIB, with $LiCoO_2$ as the cathode and graphite as the anode, with the same structure as commercial LIBs. In the standby mode, such a battery was fully charged by a TENG in 12.8 hours, with the battery voltage increased from 2.5 V to 4.2 V (Fig. 2.12b), which is the standard charging window for a commercial LIB of this type. This is the first time a LIB is fully charged by a nanogenerator! Then in the "active mode", it can run for 5.2 hours with a constant discharge current at 2 μA, corresponding to a total capacity of 10.4 μAh.

Such an operation model of switching between the two modes is suitable for a lot of applications, such as wireless sensor network systems that have a long standby mode

and a short active mode.[54] If each module can be driven by an independent power source composed of a TENG and a LIB, the operation of the wireless sensor network could be maintenance-free. We demonstrated the powering of a wireless wind and humidex thermometer (Fig. 2.12c), which consists of two parts—an outdoor remote sensor panel to measure the temperature, humidity and the wind speed, as well as to transmit the data back to the indoor receiver; a display panel with a data receiver, a data processing unit and an integrated temperature sensor. We use two TENG charged batteries (with charging curves similar as that in Fig. 2.12b) to power these two components (located ~10 m apart) respectively, and a self-powered wireless sensor network system is realized. This type of power source module could solve two vital limitations for a battery:[24] (1) the periodical replacement of a drained battery; (2) the relatively big size and weight of the battery to ensure a longer life operation. Thus, this will realize the miniature of a battery or extend its lifetime, especially for nanosystems, because they can be charged up at any time.

Another huge application of the combination of nanogenerator with battery could be in people's daily life, to power personal electronics. With the greatly enhanced output from a 9 cm^2 size single-layer arch-shaped TENG, we successfully used it to charge a commercial cell phone battery (which was completed drained). Then, it could drive a cell phone up again including making a phone call (Fig. 2.12d). Since the current of the TENG should be proportional to its area, if the TENG is scaled up in 3-dimensions, the charging rate could be tens of times higher, which is very feasible to fully charge a cell phone battery.

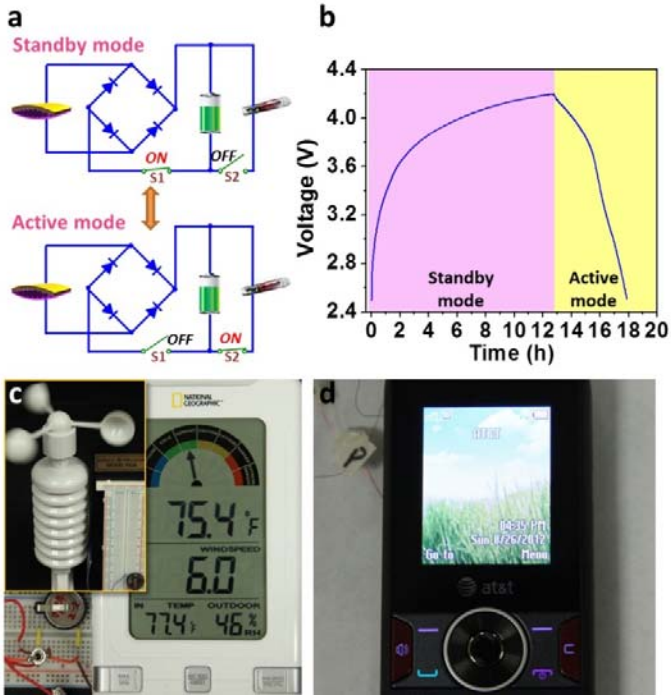

Figure 2.12 The power source module composed of an arch-shaped TENG and a lithium ion battery for driving a portable electronics that needs a regulated input power. (a) The schematic circuit diagram showing the switching between the "standby mode" and the "active mode" of the power source module. (b) The voltage curve showing the entire cycle of a lithium ion battery fully charged by TENG (standby mode) the subsequent constant current discharge at 2 μA (active mode). (c) A wireless wind and humidex thermometer, as an example of a whole wireless sensor network system, is driven by two such power source systems (one for the remote sensor module and one for the receiver-display module). (d) A commercial cell phone powered by its original battery that was charged by the TENG.

2.7 Estimation of the Energy Conversion Efficiency of the Arch-Shaped TENG

The energy conversion efficiency (η%) of the arch-shaped TENG can be calculated based on the following definition expression:

$$\eta\% \equiv \frac{Electric\ Energy\ Generated}{Mechanical\ Energy\ Applied} \times 100\% \qquad (2.27)$$

2.7.1 Electrical Energy Generated

At the deformation frequency of 6 Hz, the maximum electric energy generated by a single arch-shaped TENG within a cycle can be estimated using the data of the TENG's output characteristic when driving external load (Fig. 2.9). The highest power output is reached at the resistance of 5 MΩ, which will correspond to the maximum electric energy output (E_e). The electrical energy consumed by the load of 5 MΩ can be calculated according to the following equation:

$$E_{5M\Omega} = \int I^2 R dt \tag{2.28}$$

The curve of I^2R vs. t (R=5 MΩ) can be derived from the *I* vs. *t* curve, and through the integration of the curve in one cycle, we can get:

$$E_{5M\Omega} = 0.0153\ mJ. \tag{2.29}$$

Thus, this is the maximum electrical energy (E_e) generated by the arch-shaped TENG in one deformation cycle.

2.7.2 Mechanical Energy Applied

Before the estimation of the input mechanical energy, we need to first calculate the curvature of the arch-shaped TENG.

The calculation of the arch-shaped TENG

The Kapton film is deposited a layer of SiO_2 thin film on top using PECVD at 250°C. Since the thermal expansion coefficient of the Kapton film ($\alpha_K = 20 \times 10^{-6}/℃$) is much larger than that of SiO_2 ($\alpha_{SiO_2} = 0.5 \times 10^{-6}/℃$)), the Kapton will contract a lot more than SiO_2, so that there will appear lateral thermal stress on the interface of Kapton substrate and SiO_2 film. The plate will bend towards the SiO_2 surface.

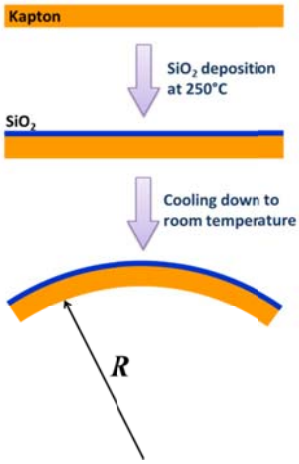

Figure 2.13 Schematic diagram showing the bending of the substrate through SiO_2 deposition at 250°C.

The linear thermal contraction of the Kapton and SiO_2 when the temperature goes down from 250°C to room temperature (25°C):

$$\Delta T = 250℃ - 25℃ = 225℃ \tag{2.30}$$

$$\Delta L_K = \alpha_K \cdot \Delta T \cdot L \tag{2.31}$$

$$\Delta L_{SiO_2} = \alpha_{SiO_2} \cdot \Delta T \cdot L \tag{2.32}$$

L is the original linear length of SiO_2 and Kapton film at 250°C after the deposition, which is 3 cm for the TENG device. The linear length difference between Kapton and SiO_2 at room temperature:

$$\Delta L = \Delta L_K - \Delta L_{SiO_2} = (\alpha_K - \alpha_{SiO_2}) \cdot \Delta T \cdot L \tag{2.33}$$

So, the thermal strain is

$$\varepsilon_{th} = \frac{\Delta L}{L} = (\alpha_K - \alpha_{SiO_2}) \cdot \Delta T \tag{2.34}$$

Thus, the thermal stress caused by the SiO_2 film is

$$\sigma_{th} = \frac{E_{SiO_2}}{1-\upsilon_{SiO_2}} \cdot \varepsilon_{th} = \frac{E_{SiO_2}}{1-\upsilon_{SiO_2}} (\alpha_K - \alpha_{SiO_2}) \Delta T \tag{2.35}$$

E_{SiO_2} and υ_{SiO_2} are the Young's modulus and poisson ratio of SiO_2, respectively.

The stress existing at the interface between the film and the substrate will result in the bending of the substrate, which can be calculated using the Stoney equation:

$$R = \frac{E_K t_K^2}{6(1-\upsilon_K)\sigma t_{SiO_2}} \tag{2.36}$$

E_K is the Young's modulus of the Kapton film, υ_K is the Poisson's ratio of the Kapton film, t_K and t_{SiO_2} are the thickness of the Kapton substrate and the deposited SiO_2 film, respectively.

All of the values of the parameters are listed below:

	Kapton	***SiO_2***
$\alpha(\times 10^{-6}/℃)$	20	0.5
E (GPa)	2.5	60
t (μm)	125	0.5
ν	0.34	0.17

Table 2.2 Property parameters of the Kapton and the SiO_2.

So, the curvature radii can be calculated to be:

$$R = 6.2\ cm \tag{2.37}$$

The estimation of the input mechanical energy

The pressing force applied to flatten the naturally-bending top plate mainly contributes on straining the Kapton film elastically, because the Young's modulus of the Kapton (~2.5 GPa) is much larger than that of PDMS (~500 kPa). Thus, the mechanical energy applied (E_m) can be estimated using the elastic energy stored in the Kapton layer from a single deformation. The thickness of the substrate (t_K) is 50 μm, and the SiO_2 film has the thickness of 80 nm.

We can assume an approximately linear strain distribution across the thickness of the Kapton film. Thus, if the local strain on the bottom surface (in contact with PDMS) of

Kapton is ε_B and the strain on the top surface (in contact with SiO_2) is ε_T, then the local strain at the plane with the vertical distance of t to the bottom plane is:

$$\varepsilon_t = \varepsilon_B + \frac{t}{t_K}(\varepsilon_T - \varepsilon_B) \tag{2.39}$$

As for the strain boundary condition of ε_T at the interface of Kapton layer and SiO_2 film, we can assume that ε_T is always determined by the thermal stress, and remains constant before and after the deformation: $\varepsilon_{Tb} = \varepsilon_{Ta} = \left(\alpha_K - \alpha_{SiO_2}\right) \cdot \Delta T = 0.44\%$.

And we can estimate ε_{Bb} before deformation using the curvature (R=6.2 cm) calculated in Discussion S1. Since the total length of the plate is 3 cm, so

$$\varepsilon_{Bb} = \varepsilon_{Tb} - \frac{3\ cm}{6.2\ cm} \times 50\ \mu m \times \frac{1}{3\ cm} = 0.44\% - 0.08\% = 0.36\% \tag{2.40}$$

And after the deformation, the flat plate will have $\varepsilon_{Ba} = \varepsilon_{Ta} = 0.44\%$. Thus, the strain distribution before the deformation:

$$\varepsilon_{tb} = \varepsilon_{Bb} + \frac{t}{t_K}(\varepsilon_{Tb} - \varepsilon_{Bb}) = 0.36\% + 0.08\%\frac{t}{t_K} \tag{2.41}$$

And after the deformation,

$$\varepsilon_{ta} = \varepsilon_{\mathrm{T}} = \varepsilon_{\mathrm{B}} = 0.44\% \tag{2.42}$$

Because the elastic energy stored under the strain of ε can be estimated using the following equation:

$$E_{elas} = \frac{1}{2} E \varepsilon^2 V \tag{2.43}$$

where E is the elastic modulus, V is the volume.

So the elastic energy stored in Kapton film caused by the deformation can be estimated as:

$$E_{elas} = \int_0^{t_K} \frac{1}{2} E_K (\varepsilon_{ta}^2 - \varepsilon_{tb}^2) A \mathrm{d}t = \frac{1}{2} E_K A \int_0^{t_K} [(0.44\%)^2 - \left(0.36\% + 0.08\%\frac{t}{t_K}\right)^2] \mathrm{d}t \tag{2.44}$$

where A is the surface area of the Kapton layer, that is 8.4 cm^2, t_K is the thickness of the Kapton film, that is 50 μm. E_K is the elastic modulus of Kapton. Thus the above integration can be calculated to be:

$$E_{elas} = 0.17\ mJ$$

Thus, the energy conversion efficiency can be calculated as:

$$\eta\% = \frac{E_e}{E_m} \times 100\% = \frac{E_e}{E_{elas}} \times 100\% = \frac{0.0153\ mJ}{0.17\ mJ} \times 100\% = 9\% \quad (2.45)$$

From the above calculation, the energy conversion efficiency of the arch-shaped TENG we demonstrated here is ~9%.

CHAPTER 3

LATERAL SLIDIND-MODE-BASED TRIBOELECTRIC NANOGENERATOR

Since a triboelectric nanogenerator is based on the coupling between triboelectrification and electrostatic induction, it is essential to have the periodic separation and contact between two surfaces with opposite triboelectric charges (tribo-charges), so that the induced potential difference between two electrodes will be changed periodically. In order to screen this potential difference, electrons will flow alternatingly between the two electrodes through an external load.[44,68] All the previously-demonstrated TENGs are all based on the vertical separation of two triboelectrically-charged (tribo-charged) planes to generate the electric polarization/field in the direction perpendicular to the planes.[42-44,68,75,76] This is the vertical contact-mode-based TENG. To realize such vertical charge separation, an air gap is mandatory to be created after the releasing of the external force, which usually requires sophisticated design of the device structures and makes the TENG difficult for packaging and practical use for some cases.

Besides the vertical-to-plane separation of two triboelectric surfaces, they can also get separated through in-plane sliding, which helps to generate triboelectric charges through sliding friction between the two surfaces. Such an operation behavior can serve as the basis for a new mode of TENG—lateral sliding-mode-based TENG.[77] In this chapter, we developed this new mode of TENG, including its basic device structure design and operation, the fundamental working mechanism, the electrical outputs with the influential factors, the unique features compared to contact-mode TENG, several derived structures (disk-based TENG[78,79] and wind-cup-based rotary TENG[80]) for harvesting rotational energy and wind energy.

3.1 Basic Structure Design and Operation Mechanism of Sliding-Mode TENG

3.1.1 Structure Design of Sliding-Mode TENG

In order to demonstrate and study the basic mechanism and characteristics of sliding-mode TENG, we have constructed a TENG based on two layers of different films as the triboelectric pair. The sliding-triboelectric nanogenerator is structurally composed of two plates (71 mm×50 mm) with glass slides as the supporting substrates to ensure the surface flatness (Fig. 3.1a). Polyamide 6,6 (Nylon) and polytetrafluoroethylene (PTFE) films, the two polymers at the opposite ends of the triboelectric series[25], are purposely chosen as the triboelectric layers adhered on surfaces of the glass slides, respectively, for effective electrification during sliding. On each polymer film, a layer of metal electrode was deposited on the side next to the glass slide (named as top electrode for the one on Nylon and bottom electrode for the one on PTFE). The two plates are kept in parallel to each other and the polymeric surfaces are in intimate contact. As driven by the mechanical motion/vibration along the long-edge of the plate, the two plates slide against each other, with the contact area changing periodically. In order to enhance the triboelectric charge density on the surface,[42,44] the PTFE film was dry-etched using inductive coupled plasma (ICP) to create aligned nanowire-structures[81] (Fig. 3.1b), which will increase the surface roughness and the effective surface area. As shown in the scanning electron microscopy (SEM) images (Fig. 3.1c), the PTFE surface is uniformly covered with nanowire-structures, with an average length of ~1.5 μm. As illustrated in Figure 3.1d, during the real-time demonstration, the PTFE-covered plate was bonded to a stationary stage, while the Nylon side was fastened to a parallel flat-end rail guide, which was connected to a linear motor for inducing an in-plane sliding motion.

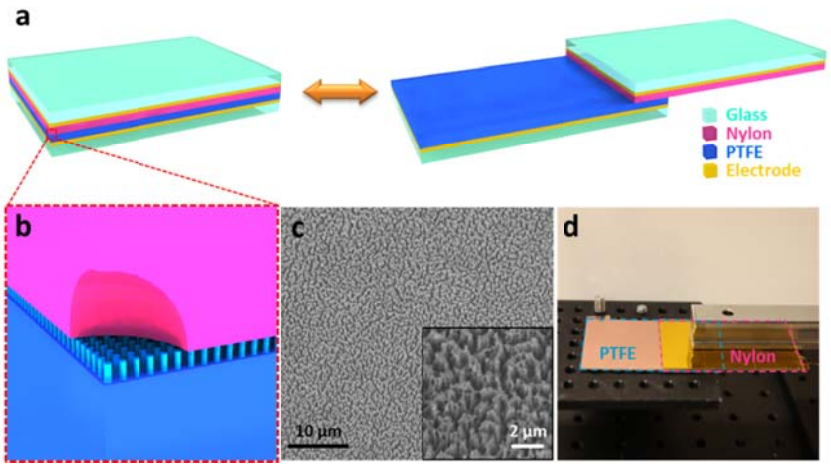

Figure 3.1 Device structure of a sliding-triboelectric nanogenerator (TENG). (a) The schematic diagram showing the structural design of the TENG in two sliding states: the overlapping position (on the left) and the separation position (on the right). (b) The magnified schematic of the surface between the two polymeric films, showing the fabricated nanowire array on PTFE surface. (c) SEM image of the PTFE surface with etched nanowire structure at the tilted view of 30°, the inset is the SEM image in higher magnification. (d) The photograph of a typical sliding-driven TENG on the measurement stage.

3.1.2 Working Mechanism of Sliding-Mode TENG

The sliding-induced electricity generation mechanism is schematically depicted in Figure 3.2a. In the original position (Fig. 3.2-I), the two polymeric surfaces fully overlap and intimately contact with each other. Because of the large difference in the ability to attract electrons, the triboelectrification will leave the Nylon surface with net positive charges and the PTFE with net negative charges with equal density. Since the tribo-charges on the insulators will only distribute in the surface layer and will not be leaked out for an extended period of time,[82] the separation between the positively-charged surface and negatively-charged surface is negligible at this overlapping position, and thus there will be little electric potential drop across the two electrodes. Once the top plate with the positively-charged surface starts to slide outward (Fig. 3.2-II), the in-plane charge separation is initiated due to the decrease in contact surface area. The separated

charges will generate an electric field pointing from the right to the left almost parallel to the plates, inducing a higher potential at the top electrode. This potential difference will drive a current flow from the top electrode to the bottom electrode in order to generate an electric potential drop that cancels the tribo-charge-induced potential. Because the vertical distance between the electrode layer and the tribo-charged polymeric surface is negligible compared to the lateral charge separation distance, the amount of the transferred charges on the electrodes approximately equals to the amount of the separated charges at any sliding displacement. Thus, the current flow will continue with the continuation of the on-going sliding process that keeps increasing the separated charges, until the top plate fully slides out of the bottom plate and the tribo-charged surfaces are entirely separated (Fig. 3.2-III). The measured current should be determined by the rate at which the two plates are being slid apart.

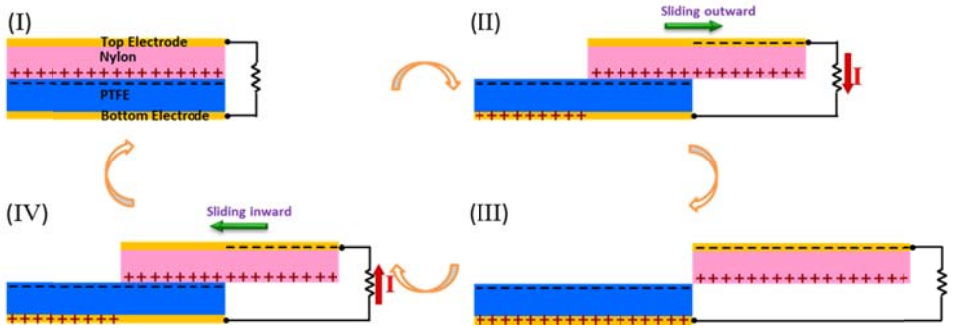

Figure 3.2 Working mechanism of the TENG based on in-plane charge separation in a full cycle of the sliding motion.

Subsequently, when the top plate is reverted to slide backwards (Fig. 3.2-IV), the separated charges begins to get in contact again but no annihilation due to the insulator nature of the polymer materials. The redundant transferred charges on the electrodes will flow back through the external load with the increase of the contact area, in order to keep the electrostatic equilibrium. This will contribute to a current flow from the bottom electrode to the top electrode, along with the second half cycle of sliding. Once the two plates reach the overlapping position, the charged surfaces get into fully contact again.

There will be no transferred charges left on the electrode, and the device returns to the state in Figure 3.2-I. In this entire cycle, the processes of sliding outwards and inwards are symmetric, so a pair of symmetric alternating current peaks should be expected.

This in-plane charge-separation-induced potential difference and charge transfer can be verified through numerical simulation using COMSOL. The model constructed here has the same structure and dimensions (71 mm×50 mm in surface) with the real device, and those two tribo-charged surfaces are assigned with a charge density of ±70 $\mu C/m^2$, respectively. The device is in open-circuit condition, which means no electron transfer between the two electrodes. As shown by the simulation results, when the two plates are in the fully aligned stacking position, which corresponds to the state in Figure 3.2-I, there is no potential difference generated (Fig. 3.3a). When the top plate slides about half way out (with a displacement of 41 mm), there will be a 2950 V potential difference between the two electrodes (Fig. 3.3b); and this potential difference will increase to 1.03×10^5 V when the top plate just slides out of touching the bottom plate (with a displacement of 71 mm) (Fig. 3.3c). We have also simulated the voltage between the two electrodes at a series of displacements from 11 mm to 91 mm. As shown in Figure 3.3d, the voltage keeps increasing when the displacement gets larger, even after the plates slide out of each other. This is because the voltage is the path-integral of the electric field along the displacement. On the other hand, the amounts of transferred charges between the two electrodes under these different displacements are also simulated through equating the potential of the electrodes at the short-circuit condition. As shown in Figure 3.3d, the amount of transferred charges increases linearly with the displacement before the top plate slides out of the bottom plate (with the displacement smaller than 71 mm). But different from the trend of the voltage, the amount of transferred charges will saturate at the total amount of tribo-charges on one surface after the plates have fully slid out of each other, because there is no further charge separation here. So, the effective displacement region for generating electricity is between 0 mm and

71 mm, where the contact area of the two plates is changed during the relative sliding of the two plates.

These simulated increase trends of the potential difference in the open-circuit condition and the transferred charge density in the short-circuit condition between the two electrodes were further confirmed by an analytical study of the sliding-mode TENG in a subsequent theoretical paper.[83]

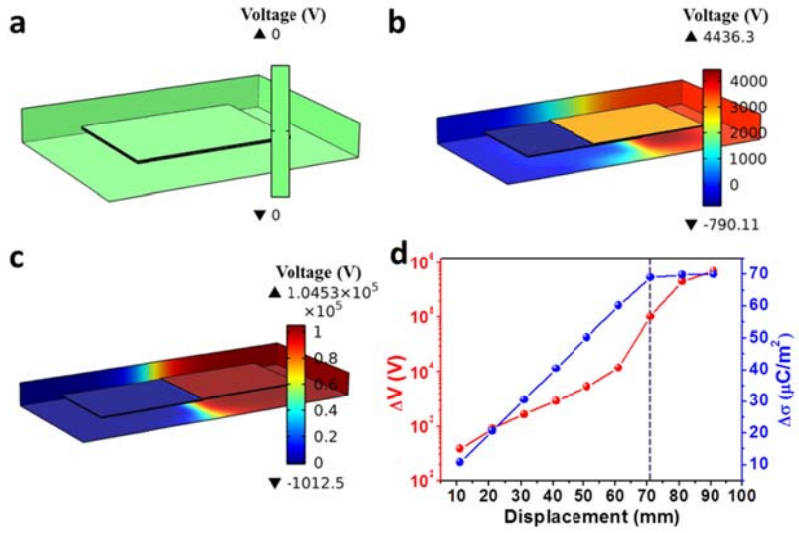

Figure 3.3 Finite element simulation of the potential difference between the two electrodes at consecutive sliding displacements: (b) 0 mm (the overlapping position); (c) 41 mm (sliding half way out); (d) 71mm (fully sliding out). (e) The curves of the simulated potential difference ΔV (red) and transferred charge density Δσ (blue) vs. the sliding displacement from 11 mm to 91 mm, in which the two plates fully slide out of each other at 71 mm (marked by the purple dot line) .

3.2 Electricity Generation Behavior of Sliding-Mode TENG

In order to experimentally study the electricity generation behavior of the sliding-mode TENG, we measured the electrical output of the above mentioned TENG device when with one plate of the TENG was guided by the linear motor in the direction parallel

to the long-edge of the plates. We systematically studied its typical electrical output and the influence of the sliding-motion parameters.

3.2.1 Typical Electrical Output from Sliding-Mode TENG

In the experimental study of the typical electrical output generated by a sliding-TENG, we set the sliding displacement as 71 mm, which was the same with the length of the plate and thus covered the entire effective region for generating electricity (as mentioned above). The sliding movement was in a symmetric acceleration-deceleration mode (the instantaneous sliding velocity was plotted as the pink curve of Fig. 3.4d), with the acceleration rate of ±20 m/s^2. The open-circuit voltage (V_{OC}) was measured by an electrometer with very large input resistance. The electrode at the back of Nylon film was connected to the positive probe. When the plates in the TENG slid from the contact position to the separated position, the V_{OC} jumped from 0 to ~1300 V (Fig. 3.4a), which reflects the induced potential difference between the two electrodes by the in-plane charge separation. At the separation position, the V_{OC} decayed a little bit, due to the slow charge leakage through the electrometer. When the TENG slid back to the contact position, the V_{OC} jumped back to 0. The density of the transferred charge ($\Delta\sigma$) was also measured at the short-circuit condition. As shown in Figure 3.4b, the charges with a density of ~105 $\mu C/m^2$ transferred back and forth between the two electrodes, while the plates slid in and out. Since the plates got fully separated in each cycle, the transferred charge density should approximately equal to the triboelectric charge density on the polymeric surfaces, according to the relationship in Figure 3.3d. With these experimental results, the measured V_{OC} is smaller than the simulated potential difference in Figure 3.3c, which is possibly due to the limitation of the electrical measurement system to record such a high voltage and the imperfection from the ideal open-circuit condition. The transfer of the charges between the electrodes in the outer circuits produced an alternating-current output, with the peak short-circuit current density (J_{SC}) of 4.1 mA/m^2

at a maximum sliding velocity of 1.2 m/s (Fig. 3.4c). The area under each current density peak is the amount of charge density transferred in each sliding motion. The enlarged J_{SC} curve in one single cycle is displayed in Figure 3.4d, together with the corresponding curve of the sliding velocity. We can find that the current output has a symmetric profile and synchronizes very well with the velocity of the sliding motion. With such a power output converted from the sliding motion, hundreds of commercial light-emitting diodes (LEDs) can be instantaneously driven by a single TENG device (Fig. 3.4e).

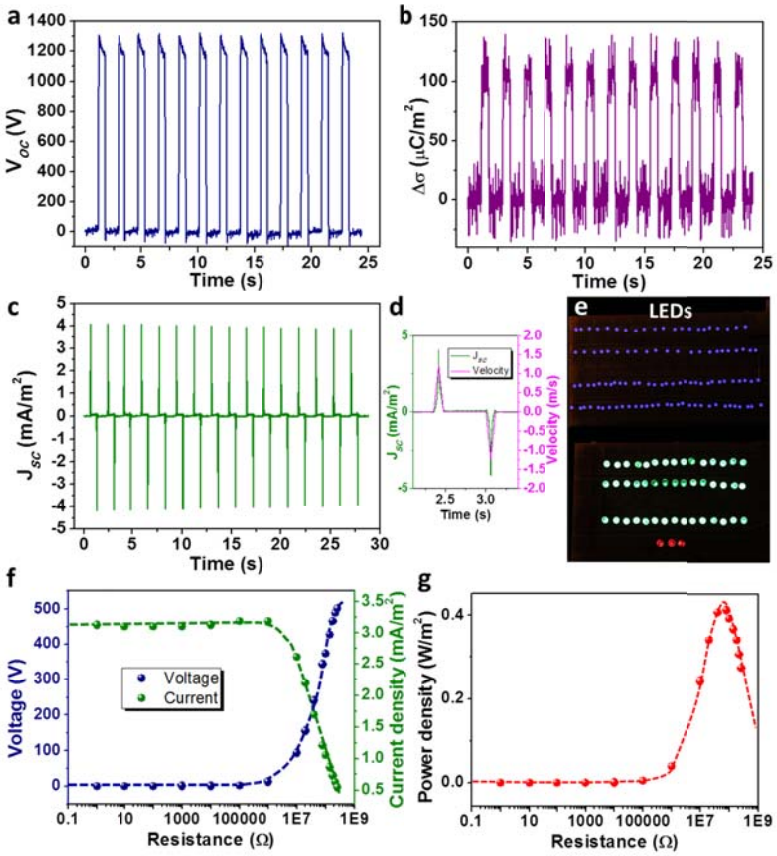

Figure 3.4 Performance of the TENG driven by the cycled sliding motion. (a) The open-circuit voltage (VOC), (b) the density of transferred charges (Δσ), and (c) the short-circuit current density (JSC) under the in-plane sliding with the displacement of 71 mm and the acceleration of 20 m/s2. (d) The enlarged profile of JSC within one cycle (green curve), with the corresponding curve of the instantaneous sliding velocity (pink). (e) The snapshot of ~160 commercial LEDs in serial-connection directly driven by a TENG under sliding. (f-g) The dependence of (f) the output

voltage (blue), current density (green) and (g) the power density on the resistance of the external load.

In practice, the TENG's effective output power to the loads depends on the match with the resistance of the load. As shown in Figure 3.4f, when the resistance is below ~1 MΩ, the output current density and the voltage have little changes from the short-circuit condition: the current density remains at a value of J_{SC} while the voltage stays close to 0. This is because the TENG has infinitely-large inner resistance. When the resistance goes beyond 1 MΩ, the current density will drop with the increase of the resistance; while the voltage on the load rises up. Consequently, the instantaneous power density on the load (Fig. 3.4g) remains close to 0 with the resistance below 1 MΩ, and reaches the maximum value of 0.42 W/m^2 at a resistance of ~50 MΩ. This is the maximum output power density on the device.

3.2.2 Influence of Sliding Motion Parameters on the Electrical Output

The output of the planar-sliding-driven TENG is directly determined by the parameters of the sliding motion—the displacement and the velocity, because the flow of electricity originates from the tribo-charge separation under sliding. As simulated in Figure 3.3d, before the two plates fully slide out of each other (with a displacement smaller than 71 mm), the voltage increases monotonically with the displacement. Also, if we assume a uniform tribo-charge distribution on the polymeric surface, the total amount of transferred charges will have a linear relationship with the displacement, which can be expressed in charge density as:

$$\frac{\Delta\sigma}{\sigma_0} = \frac{\Delta L}{L_0} \tag{3.1}$$

where $\Delta\sigma$ is the transferred charge density, σ_0 is the tribo-charge density on the polymeric surface, ΔL is the sliding displacement and L_0 is the length of the plate which

is 71 mm. According to the definition of current density (J), it has the following relationship:

$$J = \frac{d\,\Delta\sigma}{d\,t} \tag{3.2}$$

where t is the time. After merging the Equation (3.1) into (3.2), we will have

$$J = \frac{\sigma_0}{L_0} \cdot \frac{d\,\Delta L}{d\,t} = \frac{\sigma_0}{L_0} v \tag{3.3}$$

where v is the instantaneous velocity of the sliding. So, the current density should be proportional to the instantaneous velocity at which the two plates are being separated.

A systematic study of these relationships between the electrical outputs (V_{OC} and J_{SC}) and the sliding conditions was carried out experimentally. In the first group of experiments, the electrical outputs were measured under a series of 7 different sliding displacements from 11 mm to 71 mm, with an acceleration kept at 20 m/s^2. As shown in Figure 3.5a, the V_{OC} increases with the displacement, which is in accordance with the simulation results in Figure 2e. And the measured transferred charge density $\Delta\sigma$ displays a linear relationship with the displacement (the inset of Fig. 3.5b), which can be linearly fitted with the correlation coefficient of 0.981. As for the peak value of J_{SC} which is in proportional to the maximum velocity v_m, it also has a positive correlation with the displacement (Fig. 3.5b). This is because v_m has such a relationship with the displacement:

$$v_m = \sqrt{a\Delta L} \tag{3.4}$$

where a is the acceleration and ΔL is the total displacement (the displacement for each acceleration and deceleration process is $\Delta L/2$, respectively).

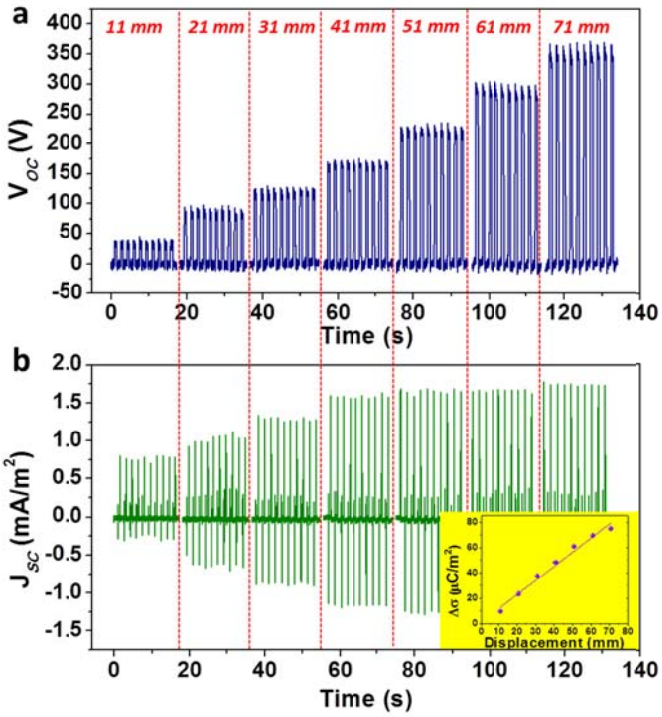

Figure 3.5 Influence of the sliding displacement on the electrical outputs. (a) The open-circuit voltage (V_{OC}), (b) the short-circuit current density (J_{SC}), and the measured transferred charge density ($\Delta\sigma$) (the inset of b) under 7 different sliding displacements from 11 mm to 71 mm.

When the sliding displacement remains at a constant value of 71 mm, the maximum velocity of the sliding is solely determined by the acceleration. Thus, we varied the acceleration to investigate the velocity's influence on the output. As shown in Figure 3.6a, V_{OC} has very little increase with the rising acceleration, which is also consistent with the theoretical expectation that V_{OC} is only determined by the displacement. However, the changing rate of the voltage will depend on the sliding velocity. The higher the velocity, the faster the voltage increases/decreases in sliding. Through differentiating the curve of V_{OC}-t, the maximum slopes of voltage at the rising edges is plotted with the corresponding maximum sliding velocity in Figure 3.6b, which shows a clear positive correlation. As for the output current, the peak value of J_{SC} gets larger at higher acceleration, because of the larger maximum velocity in sliding (Fig.

3.6c). However, the sliding velocity has no influence on the transferred charge density $\Delta\sigma$ under the constant displacement (Fig. 3.6d).

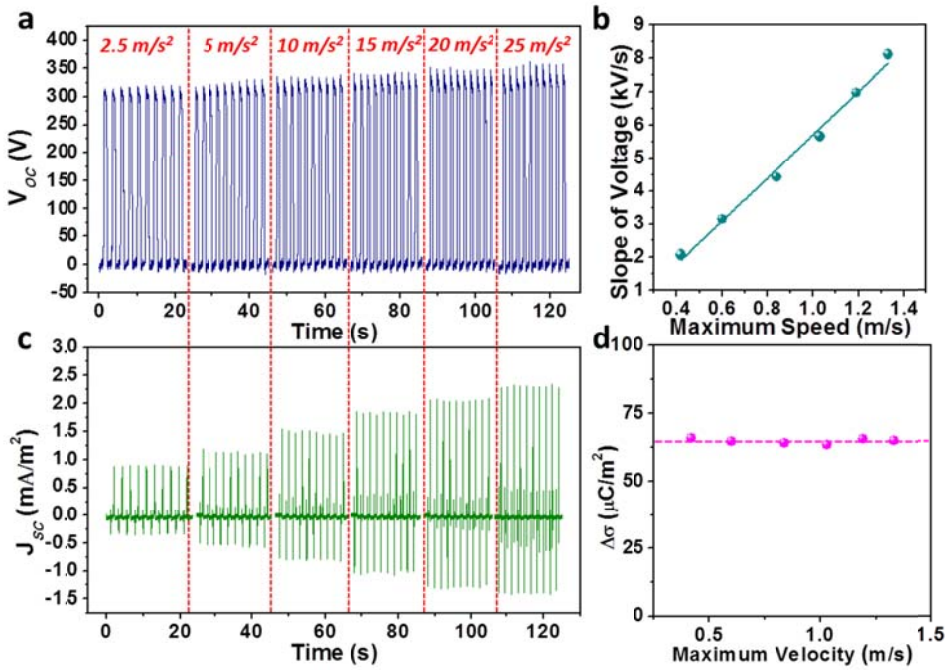

Figure 3.6 Influence of the sliding velocity (acceleration) on the electrical outputs. (a) The open-circuit voltage (V_{OC}) under 6 different sliding accelerations (which correspond to different maximum velocity). (b) The plot of the maximum slope of the voltage change *vs.* the maximum velocity. The dots are measured value and the line is the fitted result. (c) The short-circuit current density (J_{SC}) under 6 different sliding accelerations. (d) The plot of the measured transferred charge density ($\Delta\sigma$) *vs.* the maximum velocity.

The electrical output from the sliding TENG is also largely influenced by the planar distance between the two triboelectric surfaces during sliding. If the two plates do not fully in tight contact with each other at the overlapping position, which means there is always a vertical gap distance between them, the electrical output from the sliding motion will severely deteriorate. This mainly comes from two aspects. First, little triboelectric charges are generated. More importantly, if there are triboelectric charges on the plates, the gap between them in the vertical direction quickly decays the strength of electrostatic

interaction, resulting in a reduced output. As shown in Figure 3.7, when we gradually increase the vertical distance between the two plates of the TENG from 0 to 2 mm, the output voltage, current and transferred charges all quickly decay to zero. Thus, in order to have the sliding-TENG generate electricity efficiently, it is indispensable to maintain the intimate contact of the two sliding surfaces.

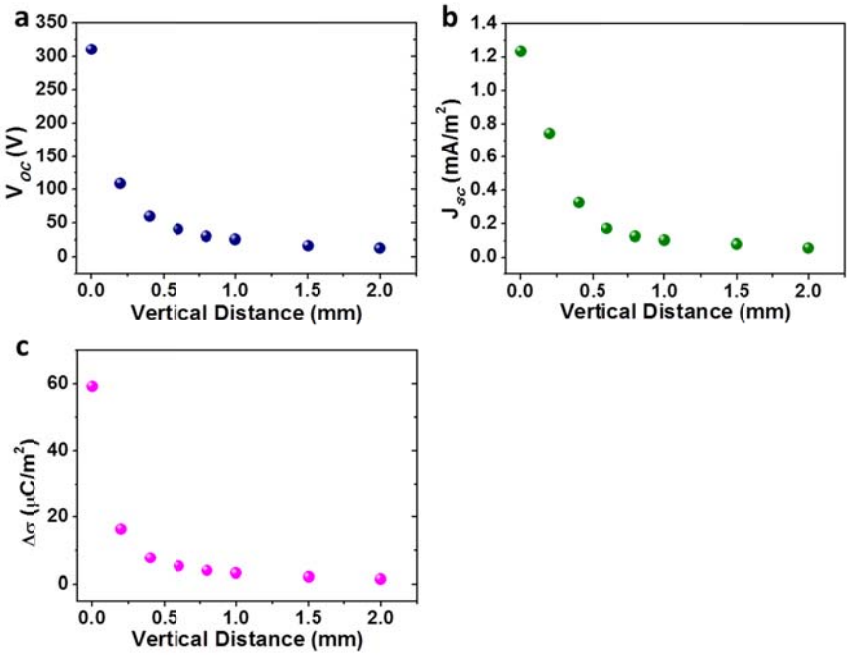

Figure 3.7 The influence of the vertical distance between the two plates on the output of the sliding- TENG. (a) The open-circuit voltage (V_{OC}). (b) The transferred charge density (Δσ). (c) The short-circuit current density (J_{SC}).

3.3 Comparison between Sliding-Mode TENG and Contact-Mode TENG

The working principle of this in-plane-separation based TENG is essentially similar to that of the existing vertical-separation based TENG. However, the characteristics of the electrical output differ a lot. As shown in the experimental comparison of the TENGs in these two modes with the same materials and dimensions (Fig. 3.8), the short-circuit current of the TENG in the planar-sliding mode has a much smaller peak value (~15 μA) but a longer pulse (Fig. 3.8a), compared to a much larger

peak value of (~240 μA) but a much shorter pulse by the TENG in the vertical-touching mode (Fig. 3.8b). This results from the difference in the charge separation process: in the planar-sliding mode, the length of the effective displacement is very large (71 mm in this experimental case), thus the charge transfer takes much longer time (Fig. 3.8c), while in the vertical-touching mode, the effective displacement length is much smaller (less than 1 mm), resulting in a much faster charge flow (Fig. 3.8d). However, as for the total amount of charges flowing through the external load for each displacement, the TENG of the planar-sliding mode delivered a larger value (380 nC) than the TENG of the vertical-touching mode (330 nC), which stands for a higher triboelectric charge density on the polymeric surface. The probable reason is that the lateral sliding between the two polymeric surfaces provides much more frictions, thus could more effectively facilitate the triboelectrification than the vertical-touching mode.

As a power source, the electricity generated by the TENGs needs to be regulated and stored in an energy storage device before powering electronic devices. It is the total amount of charges, rather than the peak current, that acts as the key factor for the efficiency of charging an energy storage device. As shown in Figure 6c-d, the TENGs in these two modes were used to charge a capacitor of 22 μF. It took 313 cycles for the sliding-TENG to charge such an empty capacitor to 10 V, while it took 365 cycles for the TENG in the vertical-touching mode. So, the proposed TENG in the planar-sliding mode shows the superiority when combined with an energy storage device.

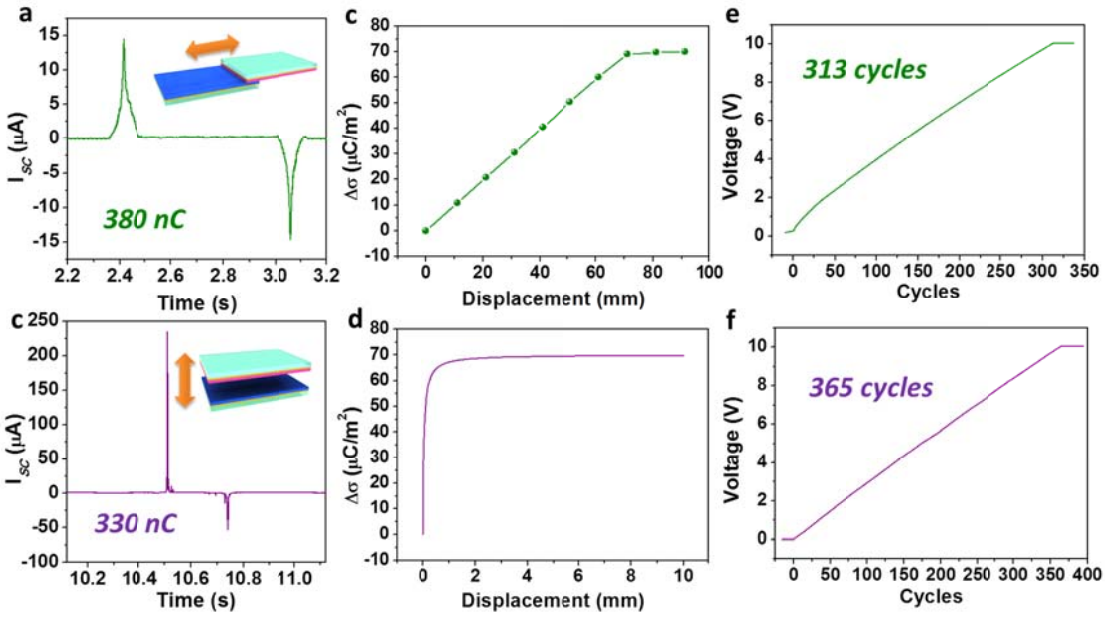

Figure 3.8 Comparison between the TENGs of the planar-sliding mode and the vertical-touching mode. (a-b) The profiles of the short-circuit current (I_{SC}) peaks within one cycle: (a) the TENG of the planar-sliding mode, (b) the TENG of the vertical-touching mode. The insets are the schematics showing the corresponding working modes. The amounts of transferred charges from a single displacement have been marked in the figures. (c-d) The relationships between the transferred charge density (Δσ) and the corresponding displacement of the TENGs in the two modes: (c) Planar sliding mode, (d) vertical touching mode. (e-f) Capacitors of 22 μF charged from 0 V to 10 V by the TENGs of the two modes: (e) the TENG of the planar-sliding mode, which takes 313 displacement cycles; (f) the TENG of the vertical-touching mode, which takes 365 displacement cycles.

Besides the above advantage, this new TENG in the planar-sliding mode has several other unique advantages. Firstly, this novel design of TENG does not need a gap between the two plates. This brings up a lot of convenience in packaging the TENG device. Secondly, there is no need for a large amount of mechanical energy input to trigger this type of TENG, which can help to improve the energy harvesting efficiency. Thirdly, this TENG is simple in structure, easy in fabrication, compact in volume, stable in performance, cost-effective and robust. With these great advantages, such in-plane

charge-separation-based TENGs can harvest mechanical energies in the form of relative sliding that are supplied by many different working configurations, for example, the relative rotation of two contacting plates, the vibration of the piston, the rotation of the axis to its tube, and so on.

3.4 Measurement of the Energy Conversion Efficiency for the Sliding TENG

For this basic structure of the sliding-mode TENG, we experimentally measured its energy conversion efficiency (η). In this measurement, the linear motor was used to introduce the sliding motion onto one plate of the device. The linear motor was connected to the sliding plate—the PTFE plate in our experimental case—through a force gauge, which can measure the real-time dragging force applied onto the sliding plate. This linear motor led the PTFE plate to slide apart from the stationary nylon plate at constant velocity. During this process, the opposite triboelectric charges on the nylon surface and the PTFE surface got laterally separated, which induced a current flow from the back electrode of nylon to the back electrode of PTFE across the external load.

According to the definition of efficiency, we have the following relationship

$$\eta\% \equiv \frac{Electric\ Energy\ Generated}{Mechanical\ Energy\ Applied} \times 100\% = \frac{E_{elec}}{E_{mech}} \times 100\%$$

From the above measurement, the E_{elec} and the E_{mech} from one sliding motion can be both experimentally obtained.

For the electrical energy generated by the sliding-TENG on the load, it can be calculated by measuring the current flowing through the load. Since the electrical energy obtained by the load reaches the maximum value at a certain load resistance, we performed the measurement repeatedly on several different external resistances. According the results shown in Figure 3.4, the maximum electrical energy should be reached within the range of 100 MΩ to 5 GΩ. Thus, the measurement was taken on the following resistance values: 220 MΩ, 500 MΩ, 667 MΩ, 1 GΩ and 2 GΩ. The current signals through these loads were obtained from one sliding motion for each case. Then,

the current curves of I~t were converted to the power curves of I^2R~t for these different load resistances, as shown in Figure 3.9a. Through integrating these power curves, we can get the electrical energy obtained by these 5 different loads, respectively. With the plot of these electrical energies versus the corresponding load resistances shown in Figure 3.9b, it can be found the electrical energy reached the maximum value 0.25 mJ of at the load resistance of 1 GΩ. Thus, the E_{elec} can be approximately taken as 0.25 mJ.

On the other hand, for the mechanical energy applied onto the sliding TENG during this sliding motion, since the PTFE plate was guided to slide from the overlapping position of the nylon plate to the fully separated position in a constant velocity, all the mechanical energy from the work of the dragging force was converted to other forms of energy. Therefore, the input mechanical energy can be obtained by calculating the work done by the dragging force during this sliding process with a total displacement of 0.075 m. Through using the force gauge, we obtained the real time curve of the dragging force in this entire sliding process. The dragging force measured for the case of 1 GΩ external resistance, in which the electrical energy reached the maximum value, is shown in Figure 3.9c. Then, the total work done by the dragging force can be calculated by integrating the curve from the distance of 0 to the distance of 0.075 m. The integration result of 4.78 mJ gave us the approximate $E_{mech.}$

Thus, from the above results of E_{elec} and E_{mech}, the energy conversion efficiency of this basic structure for the sliding-TENG can be approximately estimated as:

$$\eta\% = \frac{E_{elec}}{E_{mech}} \times 100\% = \frac{0.25\ mJ}{4.78\ mJ} \times 100\% = 5.23\%$$

In this experimental demonstration of the sliding-mode TENG, most of the input mechanical energy is converted to heat from friction—both the friction between the two sliding layers and the friction between the sliding plate and the supporting system (like the guiding rails for maintaining the sliding track). For the former, since an intimate contact between the two sliding surfaces is critically important for the effective electricity

generation, we had to apply an amount of pressing force between the two plates in order to maintain the contact during sliding in our demonstration. Because the friction is proportional to the normal pressing force, the applied force for maintaining the contact led to the increased consumption of the input mechanical energy. However, through constructing a very sophisticated and precise system, the two sliding surfaces can be strictly parallel to each other so that a pressing force may not need to maintain the contact. From this, the energy conversion efficiency can be further increased. On the other hand, for the second source of friction that is the friction between the sliding plate and the supporting system, it could also be reduced by the improved precision of the entire mechanical system. Therefore, from the above discussion, through the construction of the mechanically-precision system to minimize the friction, the energy conversion efficiency of the sliding-mode TENG can be further increased.

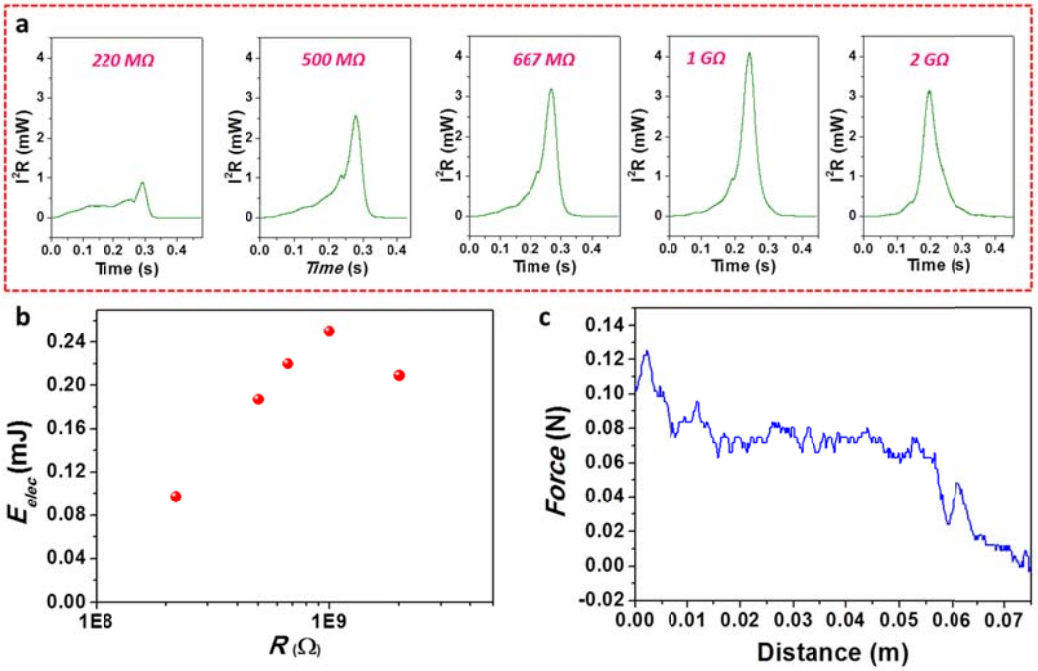

Figure 3.9 The experimental results for the estimation of the energy conversion efficiency for the sliding-TENG. (a) The curves of the power (calculated as I^2R from the curves of the current) obtained by 5 different external resistances from one sliding motion. (b) The amounts of electrical energy obtained by the above 5 external resistances. (c) The real time curve of the dragging force

applied on the sliding plate during one sliding motion (for the case with 1 GΩ external resistance).

3.5 Segmentally-Structured Disk-TENG for Harvesting Rotational Energy

The in-plane charge separation mechanism[77] introduced above for sliding-mode TENG can work in either one directional sliding between two plates or in relative rotation between two "disk"-like structures. On the basis of the one-directional sliding TENG, we further developed a segmentally-patterned disk-shaped TENG, in which a periodic overlapping and separation process of the two groups of sectors on the two concentric and closely-contacted disks is achieved by relative rotation. This design not only introduces the sliding triboelectrification between the two contacting surfaces of the sectors, but also facilitates a rotation-induced periodic, in-plane charge separation for electricity generation.[78]

3.5.1 Structure Design and Working Principle of the Disk TENG

The basic structure of the disk TENG is composed of two disk-shaped components with four sectors each, as schematically illustrated in Figure 3.10a. In the fabrication of the TENG device, two PMMA sheets were firstly processed by laser cutting to form the desired four-sector-structured cyclostyle that served as the templates for the effective contacting parts of the TENG. Then, a 50-μm-thick Kapton film with Au electrode deposited on the back side was manually-patterned into this exact shape and then securely attached onto one of the templates, while a piece of Al foil tailored into the same shape was attached on the other template. The Al part and Kapton part was brought to a face-to-face intimate contact and the Al part was driven to spin on the surface of the Kapton around their common axis. To promote the triboelectrification and increase the effective contact area between the two layers, Kapton nanorod (NR) array was created on the Kapton surface by a top-down approach[81] through ICP-RIE, as displayed in the inset of Figure 3.10a. Scanning electron microscopy (SEM) images of the Kapton NRs are

shown in Figure 3.10b. After a two-minute ICP etching, the NRs were uniformly distributed on the surface of Kapton, with an average diameter and length of 150 nm and 600 nm, respectively. Figure 3.10c is a photograph of the two parts of the disk-shaped TENG with a diameter of 4 inches. The total effective area of the TENG device is 40.54 cm^2.

The working principle of the disk TENG is based on in-plane charge separation of the sliding-mode TENG as presented above, which is induced by the relative-rotation induced between Al and Kapton, as shown in Figure 3.10d. The electricity generation process of the disk TENG can be divided into four stages: in Stage I, the two disks are at an overlapping position. There will be no potential difference between the two electrodes, thus no current flow in the external load. When the Al foil rotates in reference to the Kapton film (Stage II), the in-plane tribo-charges are thus separated in the direction almost parallel to the sliding direction, which will induce a higher potential on the Al layer than the Kapton's electrode. The electrons in the electrode attached to the Kapton film will be driven to flow to the Al foil through an external load until the two disks reach fully mismatch in the contacting segmented areas (e.g. for 45^o of rotation in this case), which is represented by Stage III. At this moment, both the induced potential difference and the amount of transferred charges between the two electrodes reach the maximum values. In Stage IV as the top plate continues spinning, the Kapton surface begins to get contacted with another adjacent sector of Al foil, and the potential difference between two electrodes will drop with the decrease of the mismatch area. As a result, the electrons will flow back in the opposite direction from the Al foil to the electrode attached to the Kapton film. Thus, the entire process will result in an alternating-current (AC) output. Such a charge transfer cycle will start over from Stage I when the two plates reach a complete overlapping again.

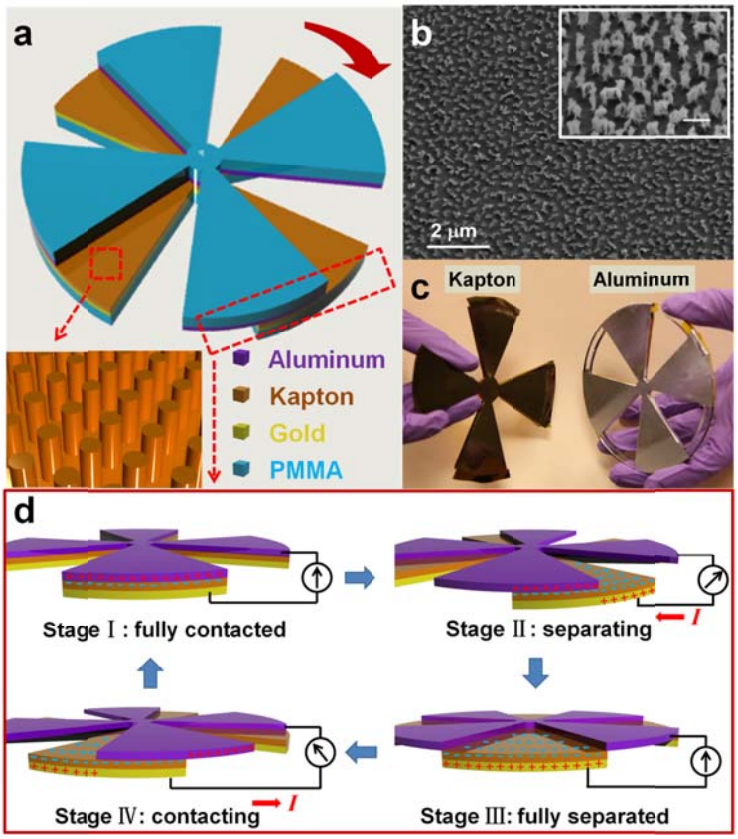

Figure 3.10 The basic structure and proposed working principle of the disk TENG. (a) The structure design of the disk TENG. The inset is an enlarged figure showing the Kapton nanorod array created on the surface area. (b) A top-view SEM image of the Kapton nanorods showing its uniformity in a large range. The inset is a high magnification SEM image of the Kapton nanorods in 30˚-tilted view. The scale bar is 500 nm. (c) A photograph showing the two parts of a real disk TENG. (d) The proposed working principle of the disk TENG with the electrons flow diagram in four consecutive stages within a full cycle of electricity generation. Please note that only one pair of sectors (the cross-section area entangled in Figure 1a) was shown with surface charges for clarity of illustration, and the surface charges on the interface area between Al foil and Kapton film are hidden and are not drawn for easy presentation.

3.5.2 Numerical Calculations and Analysis of the Output Profile for the disk TENG

To gain a more quantitative understanding of the proposed working principle of the disk TENG, we employed finite element simulation to calculate the potential

difference between the two electrodes and the transferred charge density at consecutive stages in a full cycle of charge transfer. The triboelectric charge density on the inner surface of Kapton film and Al foil was assigned as 75 μC/m^2. Figure 3.11a shows the calculation results in the four stages with rotation angles of 0˚ (Stage I), 22.5˚ (Stage II), 45˚ (Stage III), and 67.5˚ (Stage IV), respectively. In Stage I, the two layers are in full contact with each other, and there is no potential difference or charge transfer. Subsequently, as the top plate spins across this position, introducing the charge separation in the lateral direction, both the potential difference and the density of transferred charges between the Al foil and the Kapton's electrode will build up, via 1.62 kV and 34.5 μC/m^2 at 22.5˚ of half separation (Stage II), and finally to the peak values of 14.71 kV and 69.3 μC/m^2 at the fully separated position of 45˚ (Stage III). In the second half of this cycle (Stage IV), both the potential difference and transferred charge density decrease as the contact area begins to recover, and they show a symmetric behavior at the angle of 67.5˚ compared with Stage II.

The calculated potential difference and transferred charge density in a full cycle (from the 0˚ position to the 90˚ position with the step angle of 4.5˚) were depicted in Figure 3.11b. It can be observed that the transferred charge density displays a linear relationship with the rotating angle in each of the half cycles, while the potential difference presents a sharper peak, with an elevated slope around the fully separated position (the rotating angle of 45˚). Assuming a constant value of triboelectric charge density (σ_0) and uniform distribution of these charges on the inner surface of Al and Kapton, the amount of transferred charges should ideally equal to the amount of separated charges, which is proportional to the rotating angle ($\Delta\theta$):

$$\Delta\sigma = \sigma_0 \cdot \frac{\Delta\theta}{\theta_0} \tag{3.5}$$

where θ_0=45˚ is the rotating angle from the fully contacted position to the adjacent fully separated position.

These theoretical expectations were further confirmed by electrical output measurements of the open-circuit voltage (V_{OC}), transferred charge density ($\Delta\sigma$), and short-circuit current density (J_{SC}) at a constant rotation speed of 45 rpm, as shown in Figure 3.11c-e. The output profiles of both the V_{OC} and the $\Delta\sigma$ show excellent consistency with the calculation results, with the V_{OC} showing a sharp peak and the $\Delta\sigma$ showing a linear "triangle waveform" behavior. Based on Equation (2), the dependence of J_{SC} on the angular speed (ω) can be deduced as:

$$J_{SC} = \frac{d(\Delta\sigma)}{dt} = \frac{d}{dt}(\sigma_0 \cdot \frac{\Delta\theta}{\theta_0}) = \frac{\sigma_0}{\theta_0}\frac{d(\Delta\theta)}{dt} = \frac{\sigma_0 \cdot \omega}{\theta_0} = \frac{\sigma_0}{\theta_0} \cdot 2\pi \cdot \frac{n}{60} \tag{3.6}$$

where n is the rotation speed measured in a unit of rounds per minute (rpm). Therefore, as long as the angular speed (ω) remains constant, the J_{SC} should remain a constant value in each half cycle, with a symmetric AC manner in a full cycle. The measurement result of the J_{SC} in Figure 3.11e is also in agreement with this anticipated trend, which shows a "square waveform" behavior, differing a lot from the "pulse-like" current peak behavior in the previous works. This novel characteristic of NG's output performance may bring up new applications in various fields.

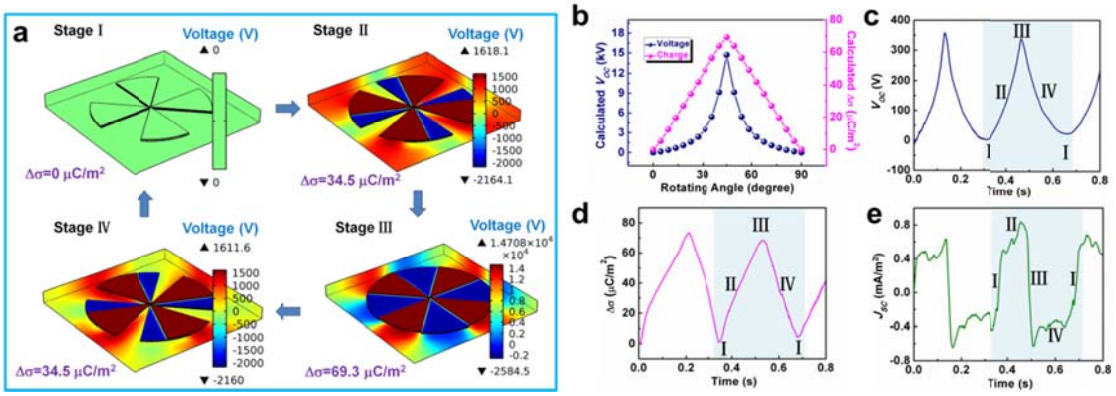

Figure 3.11 Numerical calculations of the charge transfer process of the disk TENG. (a) The numerical calculation of the potential difference and transferred charge density between two electrodes in four different stages within a full cycle of rotational motion: (I) fully contact, (II) half separated, (III) fully separated, and (IV) half contact. (b) A summary of the calculated open-

circuit voltage and transferred charge density in a full cycle of rotation. The calculation takes place from the 0˚ position to the 90˚ position, and the step angle is 4.5˚. (c-e) The measured (c) open-circuit voltage, (d) transferred charge density, and (e) short-circuit current density in a full cycle of rotational motion at 45 rpm.

3.5.3 Influence of Segmentations on Device Performance

The electricity generation process of the disk TENG relies on the magnitude and the rate of the triboelectric charge separation. In this regard, the configuration of the device, which is the number of sectors (*N*) that the entire disk is divided into, can be expected to play a significant role in the output performance of the TENG. For this purpose, we studied three types of TENG devices with the disks divided into 1 sector (Configuration 1, semi-circle), 2 sectors (Configuration 2), and 4 sectors (Configuration 3, equivalent to the structure discussed in Figure 3.10 & 3.11), respectively. Both theoretical calculations and measurements (with a rotation speed of 100 rpm) were carried out to demonstrate the effect of configurations on the output performance, as given in Figure 3.12. From the numerical calculation results in Figures 3.12a, c, and e, it could be found that as *N* increases from 1 to 4, both the calculated potential difference and transferred charge density drop to some extent. This trend is also observed in the measurement results of the V_{OC} and the $\Delta\sigma$ (Figure 3.12b, d, f). This may result from the lower magnitude of polarization due to the shrunk separation distance for finer segments. On the contrary, the J_{SC} shows a phenomenal ascending trend from Configuration 1 to Configuration 3, mainly owing to the obvious increasing of the charge transferring rate due to the smaller rotation angle from fully contact to fully separation. Above all, it could also be found that the frequencies of all the three types of output signals double with the doubled segmentations. This group of comparisons shows a clear trend that with finer segmentation patterns, the amount of electricity generated by the TENG within a single rotation cycle will be largely increased owing to the multiple times (N) of charge transferred across the external load, which can greatly boost up the power conversion

efficiency. Based on this finding, through patterning the disk with much finer segmentations using the techniques of photolithography and etching in the future work, the current output could be greatly improved.

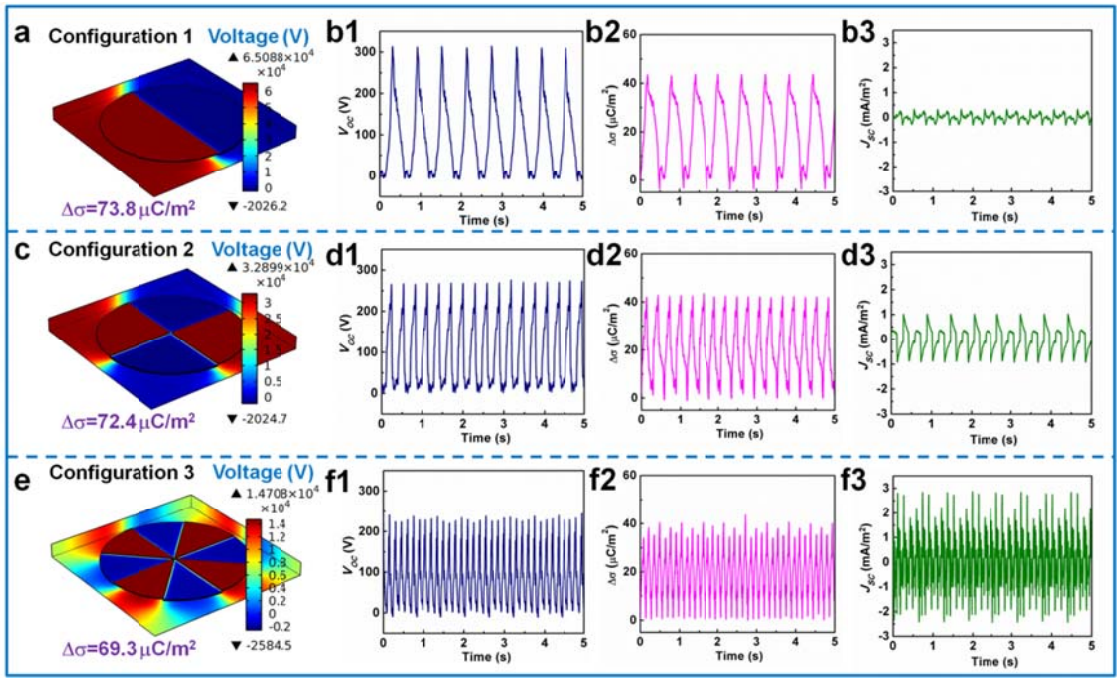

Figure 3.12 The configuration dependence of the output performance of the disk TENG. (a) The calculated open-circuit voltage and transferred charge density for the disk TENG with Configuration 1, in which the whole disk was divided into one sector (half of the full round shape). (b) The measured (b1) open-circuit voltage, (b2) transferred charge density, and (b3) short-circuit current density of Configuration 1 at 100 rpm. (c) The calculated open-circuit voltage and transferred charge density for the disk TENG with Configuration 2, in which the whole disk was divided into two sectors. (d) The measured (d1) open-circuit voltage, (d2) transferred charge density, and (d3) short-circuit current density of Configuration 2 at 100 rpm. (e) The calculated open-circuit voltage and transferred charge density for the disk TENG with Configuration 3, in which the whole disk was divided into four sectors (equivalent to the structure discussed in Figures 1 and 2). (f) The measured (f1) open-circuit voltage, (f2) transferred charge density, and (f3) short-circuit current density of Configuration 3 at 100 rpm.

3.5.4 Influence of Rotating Speed on Device Performance and Its Application as a Self-Powered Sensor

As we have discussed in the theoretical analysis, the J_{SC} will increase linearly with the rotating speed n, while the V_{OC} and the $\Delta\sigma$ should not be influenced by the velocity, as long as the configuration of the device is fixed and the initial surface charge density keeps constant (Equation 3.6). To verify these relationships, a group of electrical measurements with variable rotating speeds were conducted on the TENG with Configuration 3, which is presented in Figure 3.13. Figures 3.13a and c show the measured open-circuit voltage and transferred charge density with different rotating speeds. Both the V_{OC} and the $\Delta\sigma$ almost keep constant with the rotating speed increased from 50 to 500 rpm. Though a slight decay at high speed occurs, which might result from the relatively low sampling rate of the voltage/charge meter, it is negligible with the V_{OC} of around 230 V and $\Delta\sigma$ of about 40 $\mu C/m^2$, as summarized in Figure 3.12b and d. Besides, the averaged slopes of the V_{OC} curve were also analyzed and shown in Figure 3.13b, with an increasing trend with ascending rotating speed because of the rising of the charge separation rate. Different from the V_{OC} and the $\Delta\sigma$, the J_{SC} is strongly enhanced with higher rotating speed (Figure 3.13e), and the good linear fitting in Figure 3.13f is coherently consistent with the behavior predicted by Equation (3). This linear relationship between the J_{SC} and the rotating speed implies that the magnitude of the output current of the disk TENG could be utilized to actively measure the angular speed of a rotating disk structure, which has potential applications in automobile braking systems or transmitting instruments.

Moreover, though the magnitude of both the V_{OC} and the $\Delta\sigma$ is independent of the rotating speed, their frequencies, as well as the frequency of the J_{SC} will be directly related to the velocity. In the practical application, this could be simply realized by Fourier Transform of any output signal to acquire the frequency information.

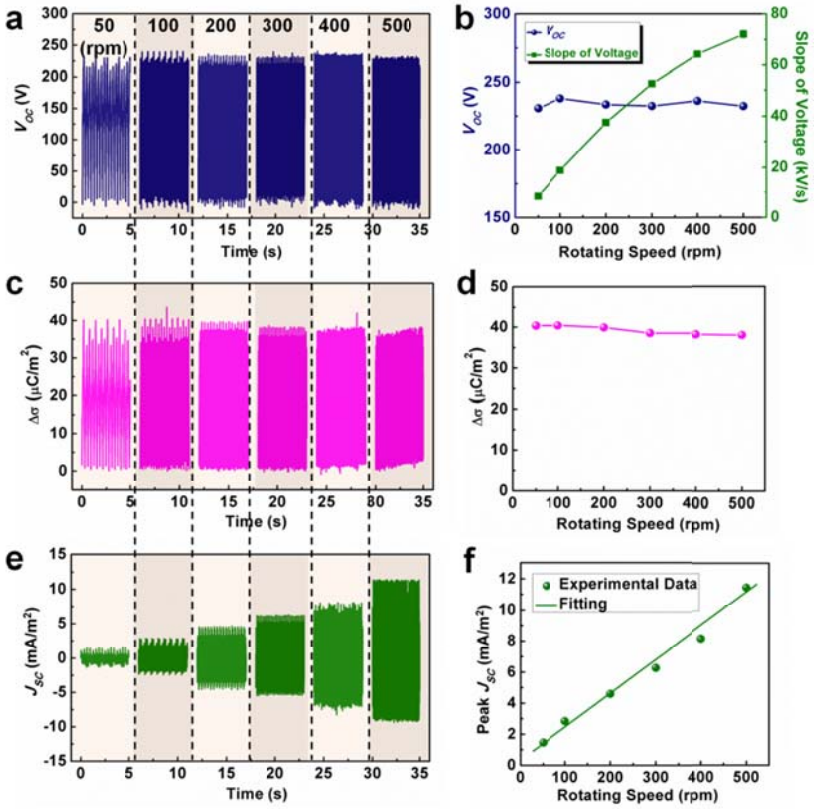

Figure 3.13 The influence of the rotating speed on the output performance of the disk TENG. (a) The measured open-circuit voltage with different rotating speeds from 50 to 500 rpm. (b) The summarized relationship between the open-circuit voltage/slope of the voltage and the rotating speed. (c) The measured transferred charge density with different rotating speeds from 50 to 500 rpm. (d) The summarized relationship between the transferred charge density and the rotating speed. (e) The measured short-circuit current density with different rotating speeds from 50 to 500 rpm. (f) The summarized relationship between the short-circuit current density and the rotating speed.

3.5.5 High Output of Disk TENG for Driving Portable Electronics

This unique design of the segmentally-patterned disk TENG realizes multiple times of charge transfers within a full rotation cycle, which enables a fast charge transfer rate at high rotating speed. This will contribute to a large output current at a high frequency. The current output of the demonstrated disk TENG at 1000 rpm could reach

29.0 mA/m^2 (Fig. 3.14a), corresponding to 117.6 μA for the entire device area of 40.54 cm^2. The frequency of the J_{SC} is as high as ~66.7 Hz, which is even a bit higher than the frequency of the commercial electric power (50 Hz). After rectification, a high-magnitude and high-frequency DC like output was achieved (Figure 3.14b), which can be used to drive portable electronic devices (e.g. 60 serially-connected commercial LEDs) instantaneously, as shown in Figure 3.14c. As we can see from 4 consecutive frames in Figure 3.14c (with a time interval of only 0.1 s) taken from the video, the disk TENG achieves a continuous lighting-up of the LEDs, rather than just flashing in the previous works[17-19]. Besides, such high frequency and large magnitude of electrical output imply a large averaged output current density and power density, which also shows its superiority when combined with energy storage units (e.g. batteries and capacitors) for long-term applications. As shown in Figure 3.14d, a 22 μF capacitor was charged by the disk TENG with variable rotating speeds at 100, 500, 1000, and 1500 rpm. The capacitor charging rates rose almost linearly with the rotating speed because of the faster charge transfer under higher rotation speeds. With the highest tested rotation rate at 1500 rpm using the device we have fabricated, the 22 μF capacitor was charged to 10 V in merely 33 s, which is a gigantic enhancement compared to the previous work[68] using the traditional type of TENG.

The output performance of the disk TENG was systematically studied at different loads. Figure 3.14e shows the resistance dependence of both output current density and voltage, from 10 Ω to 1 GΩ. The output current density decreases with the increasing resistance while the output voltage shows the reverse trend, but both the current and voltage tend to saturate at both high and low ends of the resistance. The power density was also plotted as a function of external resistance in Figure 3.14f. The output power density firstly increases at a low resistance region and then decreases at a higher resistance region. The maximum value of the power density of ~1 W/m^2 occurs at ~10 MΩ.

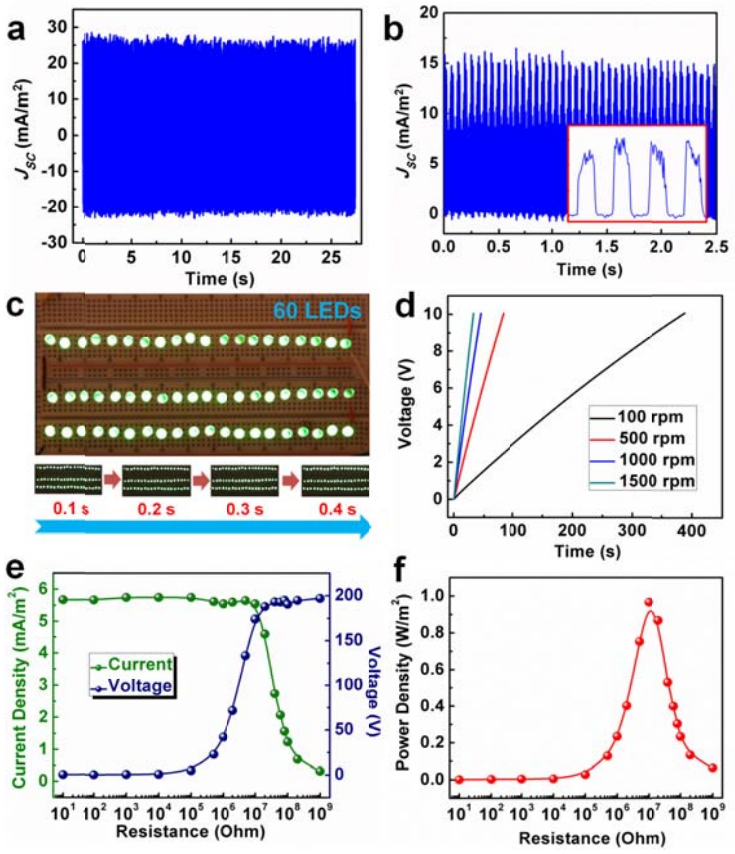

Figure 3.14 The disk TENG as a power source with high current output and frequency. (a) The measured output current for Configuration 3 at 1000 rpm. (b) The rectified output current for Configuration 3 at 1000 rpm. The inset is an enlarged view of the rectified output current with "square waveform" output profile. (c) Top: a snapshot showing the instantaneous and continuous powering of 60 green LEDs in series by the disk TENG working at 1000 rpm. Bottom: four consecutive frames captured from Video S1 with the time interval of 0.1 s. (d) The measured voltage of a 22 μF capacitor charged by the disk-TENG at variable rotating speeds. (e) The relationship between the output voltage/current and the resistance of an external load. (f) The relationship between the effective power density and the resistance of the external load. The maximum power is received when the external resistance is 10 MΩ.

Such continuous-motion-driven TENG generates the electricity with adjustable frequency and at high frequency, because it does not rely on the resilient bouncing of the TENG after mechanical triggering. This could help to realize a direct and continuous

driving of electronic devices and fast charging of storage units. The disk TENG makes it possible to harvest rotational mechanical energy at a high frequency with a high magnitude of power density, showing unprecedented superiority and practicability in both driving electronic devices directly and continuously as well as charging energy storage units.

3.6 Multi-Layered Disk-TENG for Power Enhancement

In the above design of the disk TENG, only one pair of triboelectric layers can be driven to slide by rotation motion, which is inefficient for fully utilizing the input energy. Thus, it is highly desirable to realize multi-layered integration[84] on the disk TENGs, which requires two critical issues resolved in the structure design in order to reach a multiplied output performance: intimate contacts between any two adjacent triboelectric layers maintained during the rotation, under a minimized pressing for a small resistance; strictly synchronized rotation of all the segmentally-structured disk pairs so that the output from each pair can be perfectly added-up. For this regard, we developed an effective strategy for the multi-layer integration of the disk TENGs, with the above two issues resolved.

3.6.1 Structural Design of Multi-Layered Disk-TENG

In the design of the multi-layered disk TENG, a D-shape shaft was introduced to coaxially transmit the rotation motion onto each rotor (rotation part in each triboelectric layer), with the segmental phase synchronized. On the other hand, to maintain intimate contact of the tribo-surfaces, light weight and low stiffness springs were adopted to fix the stators at the four corners and provide a gentle and adjustable pressing force. The multi-layered disk TENG is mainly composed of two groups: rotors with Al film as the attached triboelectric layers, and stators with the purposely chosen PTFE film as the other triboelectric layers, with 8 segmentations. They are coaxial with the input rotation motion, as schematically depicted in Figure 3.15a. The multiple-layered structure was

obtained by stacking three stators and two rotors in an alternating sequence, with the D-shape shaft going through all the center-holes. Each pair of PTFE film and aluminum film next to each other constitutes a disk-TENG unit. When the D-shape shaft is connected to a rotating object, e.g. a rotary motor in the experimental measurement, all the Al layers on the rotors will be driven to rotate with the same phase, while the PTFE layers on the stators will stay still. In this manner, the relative rotation between the adjacent layers enables periodic contact-separation cycles of the opposite triboelectric charges, and thus generates electricity in each layer. When all of the four layers of the multi-layered disk TENG are connected in parallel, the current with the same phase can be added up, contributing to a multiplied power output. It is worth noting that, in order to enhance the surface roughness and promote the triboelectrification intensity, the aluminum films on the rotor part were coated with silver nanoparticles.[85] Figure 3.15c shows the SEM images of the assembled silver nanoparticles on Al film, which uniformly distribute across the whole surface with an average diameter of 50 nm. In this experimental demonstration, the projected surface area of the TENG device is 34.2 cm^2.

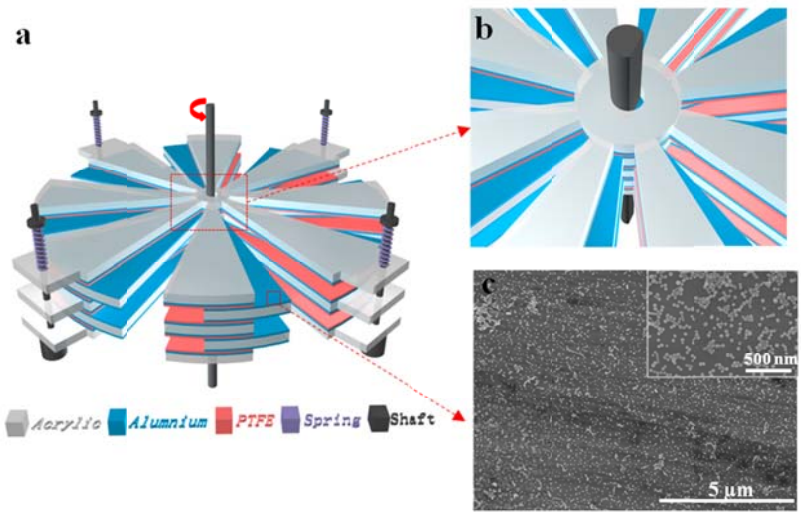

Figure 3.15 Device structure of the multi-layered disk TENG. (a) The schematic diagram showing the structure design of the multi-layered disk TENG. (b) The enlarged picture showing the D-shape shaft going through all the center-holes. (c) The SEM image of the silver

nanoparticles coated on the aluminum electrode of the rotor part, the inset is the SEM image in higher magnification.

3.6.2 Enhanced Electrical Output by the Multi-Layered Structure

The electrical outputs of the four-layered disk TENG, were measured by connecting the shaft to a spinning motor with a rotation speed of 10 rpm (Fig. 3.16). The rotors were driven to make a relative rotation movement against the stators. At first, the V_{oc}, short-circuit current density (J_{sc}), and $\Delta\sigma$ of each individual units (named as Unit 1~4, respectively) were measured separately (the outputs from Unit 1 are shown in Figure 3.16a as typical results). By connecting the layers in parallel, the obtained output from each layer can add up to give a multiplied output. As shown in Figure 3.16b, when two triboelectric units were connected, the transferred charge density was increase to 110 $\mu C/m^2$ with an enhanced J_{sc} of 0.9 mA/m^2 (Fig. 3.16c), both of which are about twice of the one-layer results, while there is very little change on the V_{oc} (427V). If three units were integrated, the $\Delta\sigma$ and J_{sc} were triply enhanced to 169 $\mu C/m^2$ and 1.2 mA/m^2, respectively, and V_{oc} still stayed comparable to that from an individual layer. After connecting all of the four units together, the $\Delta\sigma$ and J_{sc} were further scaled up and reached the highest values of 234 $\mu C/m^2$ and 1.5 mA/m^2, respectively. At this time, the V_{oc} only had a small increase to 470 V. From the above results, we can conclude that the multi-layered integration with parallel electric connection gives transferred charge density and short-circuit current density a good superposition relationship, while the open-circuit voltage will remain on the same level. Furthermore, based on the output enhancement trend from increased layers, we should be able to further improve the electrical outputs by integrating more units into a whole device. Therefore, the multi-layered parallelly-connected structure is an effective and indispensable method to achieve high electrical output, especially large current density.

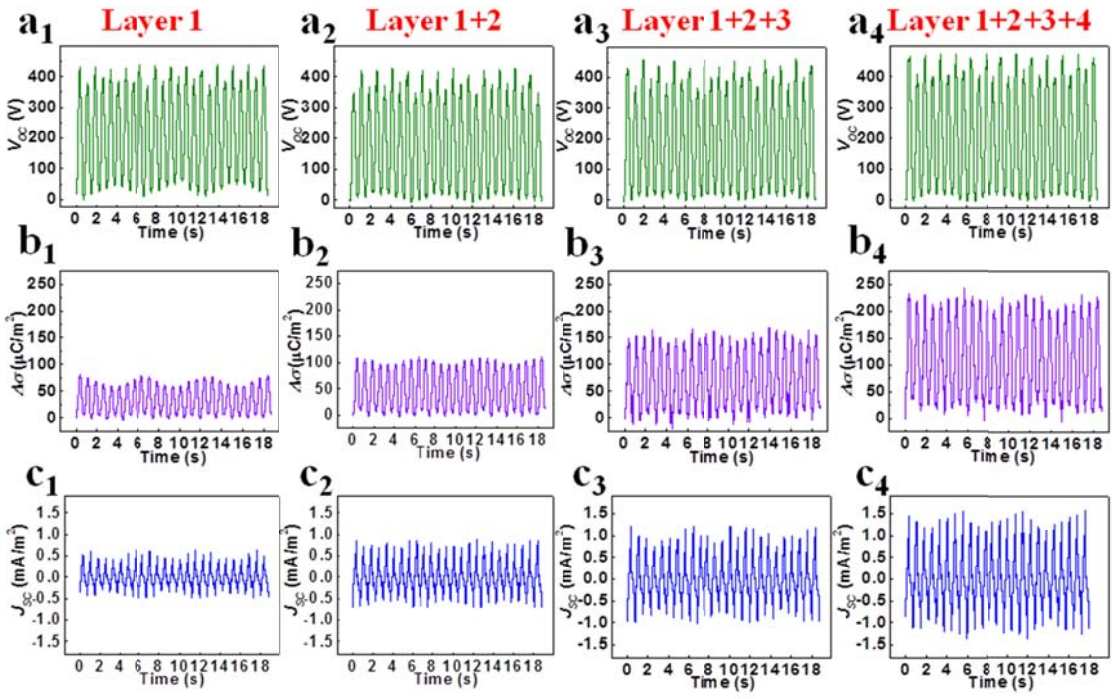

Figure 3.16 Electrical output of the disk TENG with different configurations under the rotation speed of 10 rpm. (a_1-a_4) The open-circuit voltage (V_{oc}), (b_1-b_4) the transferred charges density ($\Delta\sigma$), and (c_1-c_4) the short-circuit current density (J_{sc}) of the disk TENG with one, two, three, and four tribo-charged units.

With the integration of four layers disk-TENG units, the electrical output of the device can reach a high level at an increased rotation speed of the rotors, since a larger rotation speed will lead to faster tribo-charge transfer process, which increases the current density and thus the output power density. As shown in Figure 3.17a, when the rotation speed was set at 1000 rpm, the J_{sc} of the TENG reached 86.8 mA/m^2, which is about 4 times as large as the previously-reported single-layered disk TENG.[78] To characterize the power output of the device, we also measured the V_{oc} under the rotation speed of 1000 rpm. As shown in Figure 3.17b, the voltage remains the same value with that at low-speed condition (10 rpm), which implies that the indispensable intimate contact of the triboelectric surfaces during rotation is not affected by the high rotary speed. In practical applications, the energy harvester is usually connected to external loads with different

resistances, so that we systematically studied the voltage and current outputs on a series of different resistances, from 100 Ω to 150 MΩ. As depicted in Figure 3.17c, the current density drops with the increase of the external resistance, while the voltage across the load shows a reversed tendency. Figure 3.17d illustrates the power density as a function of load resistance. The power density initially rises at a low resistance region and then declines significantly at a higher resistance region, showing a peak value of ~5 W/m^2 at ~1 MΩ (Fig. 3.17d).

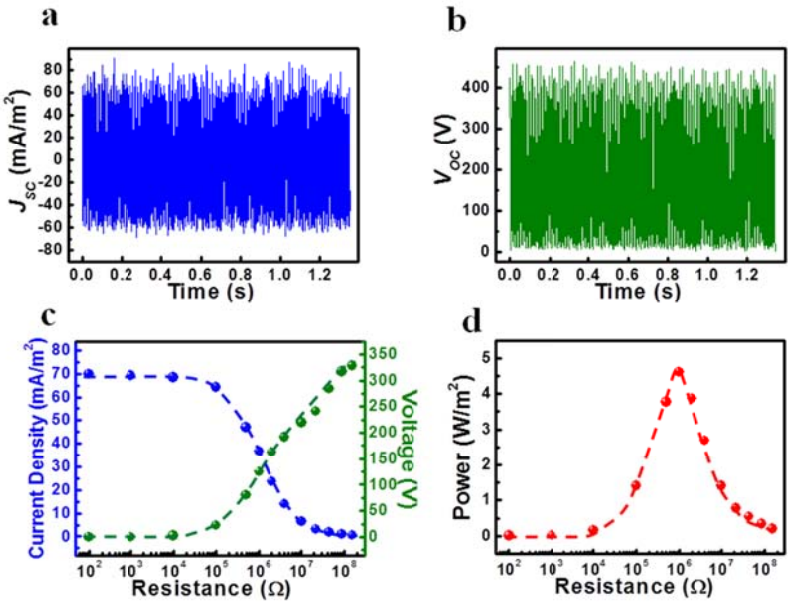

Figure 3.17 Output performance of the four-layer disk TENG at 1000 rpm. (a) The J_{sc}, and (b) V_{oc} of the device. The dependence of (c) the output voltage (green) and current (blue) and (d) the power density on the resistance of the external load.

3.7 Rotary TENG Based on Hybridized Mode for Harvesting Wind Energy

Through hybridizing the two basic working modes of TENG—the vertical contact mode and the lateral sliding mode, we developed a rotary structured triboelectric nanogenerator (R-TENG) for scavenging weak wind energy in our environment.[80]

The conventional approach of generating electricity from wind relies on the structure of wind turbines and the principle of electromagnetic induction.[48] However,

there are several drawbacks of this kind of devices, including large size and weight, high cost of installation, difficulty to be driven under low wind speeds, and thus low efficiency, which limits its usability especially for the weak wind in our daily living environment such as around houses and in the city.[86] Recently, piezoelectric windmills employing piezoelectric bimorph transducer structures have been reported with low start-up speed and small sizes.[87-89] However, the structures are still complex and the outputs are relatively low.

In the demonstrated R-TENG, under the wind flow, the wind-cup structure will be driven to rotate and thus the soft and flexible PTFE film based rotor blade will sweep across the Al sheets based stators consecutively, so that a repeating process of contact-sliding-separation-contact between the two charged surfaces can be achieved by hybridizing the two modes.

3.7.1 Structural Design of the Rotary TENG

The structure of the R-TENG springs from the conventional wind cup structure, which includes a framework, a shaft, a flexible rotor blade, two stators, as illustrated in Figure 3.18a. A flexible and soft rotor blade structurally made of a polyester (PET) film is connected to the shaft, thus can rotate with the shaft. Around the circumference of the device, two Al covered plates as the symmetric stators stretch out from the framework towards the shaft direction. On top of the shaft, the wind cup setup is mounted to convert the wind flow into the rotation of the shaft and the flexible rotor, during which the rotor blade will periodically sweep across the stators with small resistance. In this process, a consecutive face-to-face contact (in area of 2.5 cm × 6.4 cm) and separation between the rotor and the stator will be enabled, which can serve as the basic TENG-based process for generating electricity. A PTFE film was chosen to adhere at the end of the PET blade as a triboelectric layer to get into contact with Al. A layer of metal film was deposited between the PTFE and PET as the electrode. In order to enhance the surface roughness

and therefore improve the triboelectric charge density,[42,44] the PTFE film was dry-etched through ICP-RIE to prepare nanowire-like structures on the surface[81] (with the magnified scheme in Figure 3.18a). As shown in the SEM images, after a 40-second etching, the nanowire-like structures were uniformly distributed on the surface of PTFE, with an average length of ~700 nm (Figure 3.18b). The photograph of an as-fabricated R-TENG device is shown in Figure 3.18c.

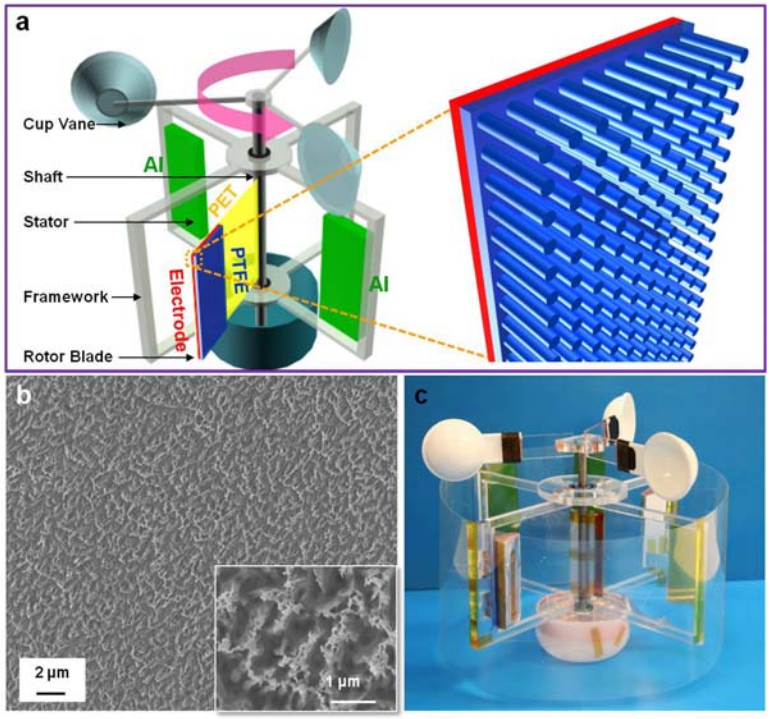

Figure 3.18 Device structure of the rotary TENG (R-TENG). (a) The schematic diagram showing the structural design of the R-TENG, with the enlarged picture showing the nanowire-like structures on the surface of PTFE. (b) The SEM image of the PTFE surface with etched nanowire-like structures; the inset is an SEM image of the nanowires. (c) A photograph of the fabricated R-TENG.

3.7.2 Working Mechanism of the Rotary TENG Based on Hybridized Contact-Sliding Mode

The electricity generation of the R-TENG is a hybridization of contact-sliding-separation-contact processes, as schematically depicted in Figure 3.19. In the original

state where the rotor blade is stationary and the triboelectric layers are separated from each other (Fig. 3.19a), there is no tribo-charges generated on the surfaces. When the wind blows on the wind cups, the rotor blade will be driven to rotate around the shaft, which will bring the PTFE film into full contact with the Al on either one of the stators (Fig. 3.19b). As a result of triboelectric effect, the PTFE film will have net negative charges and the Al with positive charges. At this very moment, there is little electric potential difference generated in the space. As the polymeric rotor blade continues to rotate, the flexible blade will be bent in order to sweep across the rigid stator (Fig. 3.19c). Because of the strong electrostatic attraction between the two tribo-charged surfaces, the PTFE film has the tendency to keep the intimate contact with the Al stator, so that most of the bending happens on the PET portion of the rotor blade. The PTFE plate will be guided to slide outwards across the Al surface, leading to a continuous decrease in the overlapping area of the two tribo-charged surfaces and thus the in-plane charge separation. The lateral dipole moment will generate a higher potential on the Al surface, thus drives a current flow in the external load from the Al to the electrode of PTFE. This process will last until the PTFE fully slides out of the Al surface, and the total transferred charges will equal the amount of the triboelectric charges on each surface. This is the working mechanism of the TENG in the sliding mode, which can help to generate higher triboelectric charge densities because the sliding provides much more friction than the contact mode, and it is more effective for triboelectrification.[77] Subsequently, the rotor blade will continue to rotate towards the other stator, with the attached electrode having positive charges with equal density of the negative tribo-charges on the PTFE surfaces (Fig. 3.19d). When the rotor blade approaches the other Al blade, the two surfaces will get into contact momentarily in vertical direction (Fig. 3.19e). An electric potential difference pointing from the electrode on the PTFE to the Al sheet will be generated, driving a reversal current flow. This is the working mechanism of the TENG in the contact-separation mode. At this point, a cycle is completed. Thus, the entire electricity

generation process of the R-TENG hybridizes the in-plane contact-sliding mode and the separation-contact mode in vertical direction as a full cycle process and generates a pair of alternating current: one lower-magnitude but wider peak corresponding to the in-plane charge separation and one sharper but narrower peak corresponding to the vertical charge re-contact (Figure 3.19f).

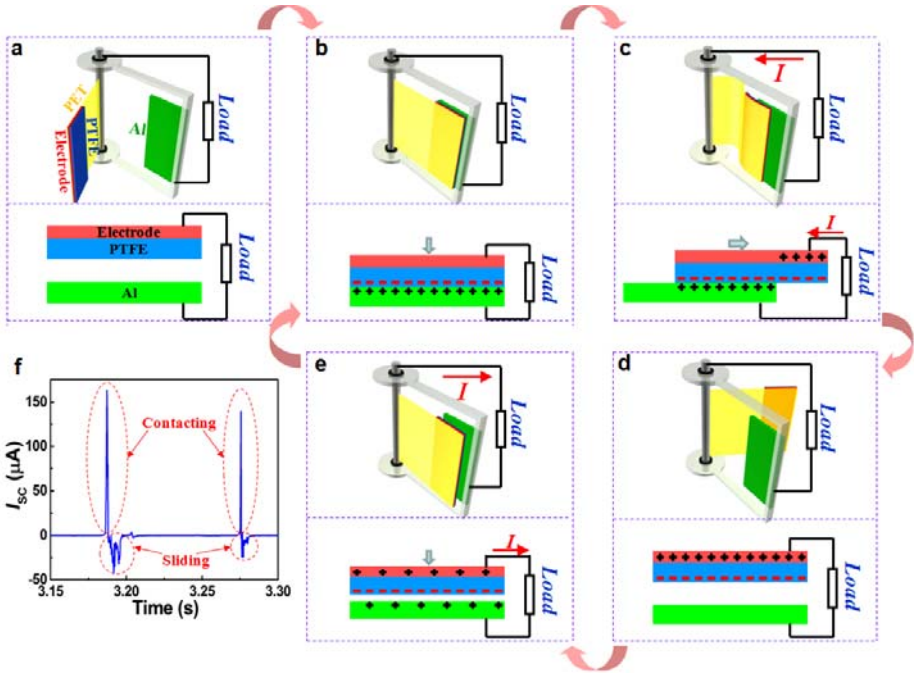

Figure 3.19 Working mechanism of the R-TENG based on a hybridization of contact-sliding-separation-contact processes. Three-dimensional (upper) and cross-sectional (bottom) sketches of: (a) original position without wind blow; (b) PTFE is brought into contact with Al stator; (c) PTFE is sliding apart from the Al surface; (d) PTFE is separated from Al stator; and (e) PTFE approaching to the next Al stator. (f) The typical profile of the current output from the R-TENG.

3.7.3 Electricity Generated by Wind Energy

The electrical output measurement of the R-TENG was carried out under a wind speed under different wind speeds from 6.3 m/s (4 BF in Beaufort wind force scale) to 20.1 m/s (8 BF). As shown in Figure 3.20a, with the wind speeds being raised, the V_{OC} firstly shows a small increase trend at lower wind speeds and then reaches a saturated value of 250 V. This result can be explained by the change in the surface charge density.

The higher the wind speed, the larger rotational torque obtained by the polymer films, which means a larger contacting force. Since the PTFE surface was patterned with nanowire-like structures, a larger force applied will make the two surfaces contact more intimately, resulting in a higher surface charge density. But this will reach a saturated value after the contacting force is large enough.[90] As for the I_{SC}, the peak heights present a very obvious increasing tendency with the increased wind speeds (Fig. 3.20b), because a higher wind speed will not only results in more transferred charges as discussed before, but also more importantly contributes a higher charge transfer rate. This set of results not only indicate a high power output of the R-TENG as driven by a stronger wind, but also show the potential of the R-TENG as a self-powered wind speed sensor. Besides the magnitudes of the electrical outputs from the R-TENG, the information of the wind speed is also reflected by the time interval between two adjacent peaks, in other words, the number of peaks in a certain time. This is because the higher wind speed will drive a faster rotation of the rotor blade so that it will increase the frequency of the output. Thus, by using a counter to calculate the number of peaks within a certain time, the corresponding wind speed can also be accurately obtained. Based on the above discussion, the R-TENG can be used as a self-powered active sensor for real-time wind speed detection.

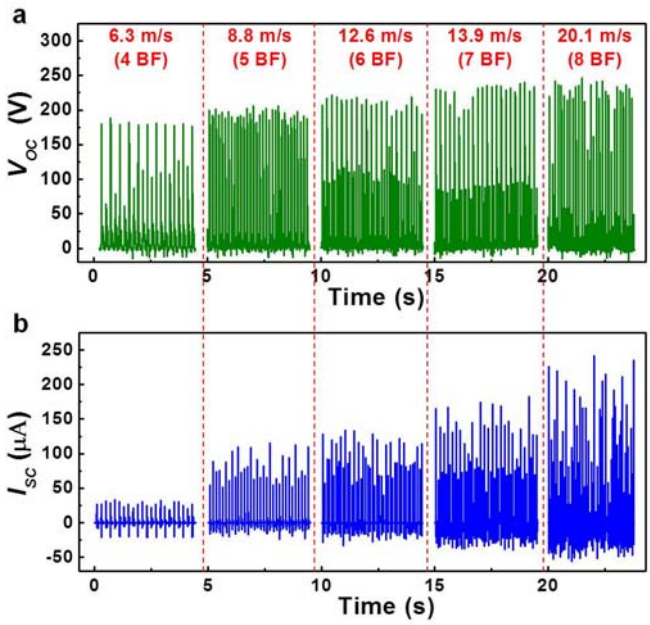

Figure 3.20 Influence of the wind speed on the electrical outputs. (a) The V_{OC} and (b) the I_{SC} under different wind speeds from 6.3 m/s (4 BF) to 20.1 m/s (8 BF).

Because of the viability to work at relatively low wind speed, this demonstrated R-TENG can be used to effectively harvest the energy from natural wind outside of office building! As shown in Figure 3.21a, when the modest wind blew through R-TENG, it generated electricity with a maximum I_{SC} over 50 μA. In a lot of cases, the fluctuated electrical output generated from the natural wind needs to be stored for further use. Figure 3.21b shows the charging curves of two capacitors (2.2μF and 22 μF, respectively) by the R-TENG at a wind scale of ~6 BF, indicating a high efficiency of converting the wind energy to the stored electrical energy. Besides, in some other cases, the instantaneous output of the R-TENG can be used to directly drive a number of electronic devices simultaneously. As shown in Figure 3.21c, 164 serial-connected commercial LEDs were lit up by the wind-generated electricity from the R-TENG.

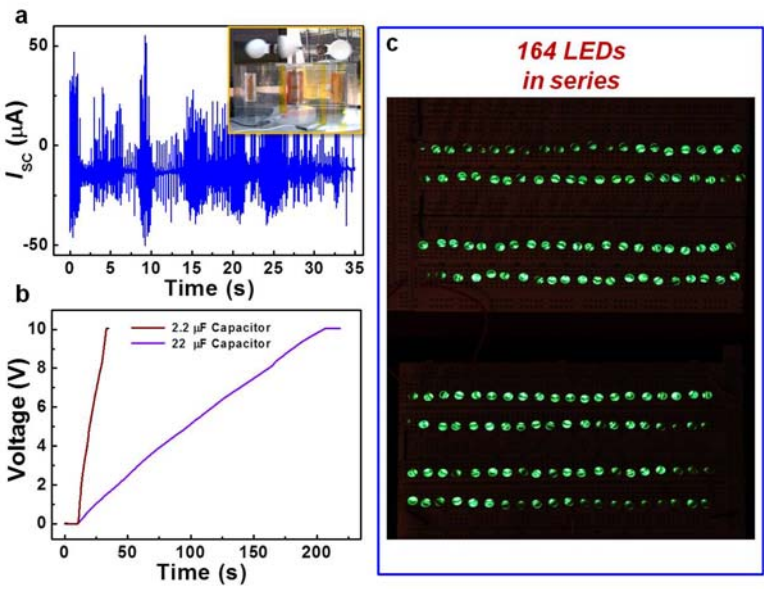

Figure 3.21 Applications of the R-TENG. (a) The R-TENG generating electricity from the wind blow in outdoor area, the inset is the picture of the R-TENG working under the wind blow in outdoor area (b-c) The R-TENG used as a power source to (b) charge capacitors and (c) directly light up 164 commercial LEDs.

This structure design introduced a novel operation mechanism for wind generators and created a new development area of the wind power using nanostructured surfaces of conventional materials. Furthermore, this technology can also be extended for harvesting energy from ocean current.

CHAPTER 4

FREESTANDING-LAYER-MODE BASED TRIBOELECTRIC NANOGENERATOR

In the real application of TENG in harvesting applied mechanical energy, in order to maximize the energy conversion efficiency under such mechanism, one of these triboelectric layers needs be bonded with a moving object as the mechanical energy source. However, in the previous two basic modes of TENGs—the contact mode[43,44,68] and the sliding mode,[77,78] each triboelectric layer is attached with an electrode and a lead wire. Such a device configuration largely limits TENGs' versatility and applicability for harvesting energy from an arbitrary moving object or a walking human, because the object has to be connected to the entire system by an interconnect. Thus, it is highly desirable to develop a new mode of TENG based on a new mechanism that can scavenge energy from the mechanical motion of a freestanding triboelectric layer, without an attached electrode.

The kernel of TENG-based electricity generation is a periodic change of the induced potential difference (IPD) between two electrodes as a result of the relative position change of the tribo-charged surfaces.[44,68] This general principle can be achieved by a new type of design and operation mode: a TENG with two stationary electrodes and one freestanding triboelectric layer that moves in between under the guidance of external mechanical energy.[91] In this mode, the dielectric layer can alternatively get in direct contact with either one of metal electrodes (or just within a short distance), which enables periodic changing of IPD to drive the flow of charges in the external load. The triboelectric layer can be either pre-charged or charged during contact, because the electrostatic charges on an insulator film surface can be preserved for hours even days.

4.1 Dielectric-Conductor Based Freestanding-Layer-Mode TENG

The first type of the FTENG is based on the triboelectric effect between a freestanding dielectric layer and two metal films that serve not only as the counter triboelectric material, but also as two electrodes.

4.1.1 Device Structure and Working Mechanism

The basic device structure of the conductor-dielectric based TENG is shown in Figure 4.1a. In order to maximize the electrification between the two layers, we purposely chose materials with a large difference in triboelectric polarity—Al as the conducting films and fluorinated ethylene propylene (FEP) as the freestanding triboelectric layer. The FEP film was tailored into a 7 cm × 5 cm rectangle, and then adhered on the supporting substrate (made of acrylic) of the same size. In order to further improve the triboelectric charge (tribo-charge) density, the downside surface of the FEP film was treated by ICP to create nanorod structures.[44,81] On the other side, two rectangular Al electrodes of this exact size were deposited on another acrylic substrate perpendicular to the sliding direction. The length (L) of the electrode along the sliding direction is 5 cm, and the in-plane distance (d) between the two electrodes is purposely controlled as one of the most important parameters in the device structure (Fig. 4.1b<i>). Driven by a tangential force, the freestanding FEP layer can slide back and forth between the two electrodes (Fig. 4.1), through which alternating-current is provided to the load connected between the two electrodes.

When the FEP slides against the Al electrodes with surfaces in contact, the triboelectric effect will render FEP surface with negative charges, and Al electrodes with positive charges. There are two sceneries. In the first case, if the dielectric FEP and the electrodes are uncharged at the first place, all of the static charges are then to be generated by the triboelectrification after their physical contact. The negative charges on the FEP surface should have an equal amount with the positive charges in the electrodes.

When the FEP is at the position fully overlapped with the first electrode (e.g., the left electrode as shown in Fig. 4.1b<i>), all of the positive charges in the loop will be attracted to the upper surface of the left-hand electrode (LE). Then, when the FEP layer slides towards the right-hand electrode (RE) (Fig. 4.1b<ii>), the positive charges in the loop will flow from the LE to the RE via the load to screen the local field of the non-mobile negative charges on the dielectric, which is the first half cycle of electricity generation. When the FEP reaches the overlapping position of the RE (Fig. 4.1b<iii>), all of the positive charges will then be driven to the RE. Subsequently, a backward sliding of the FEP layer from the RE to the LE should drive the flow of the positive charges in the same direction, forming a reverse current in the load (Fig. 4.1b<iv>). This is the second half of electricity generation process.

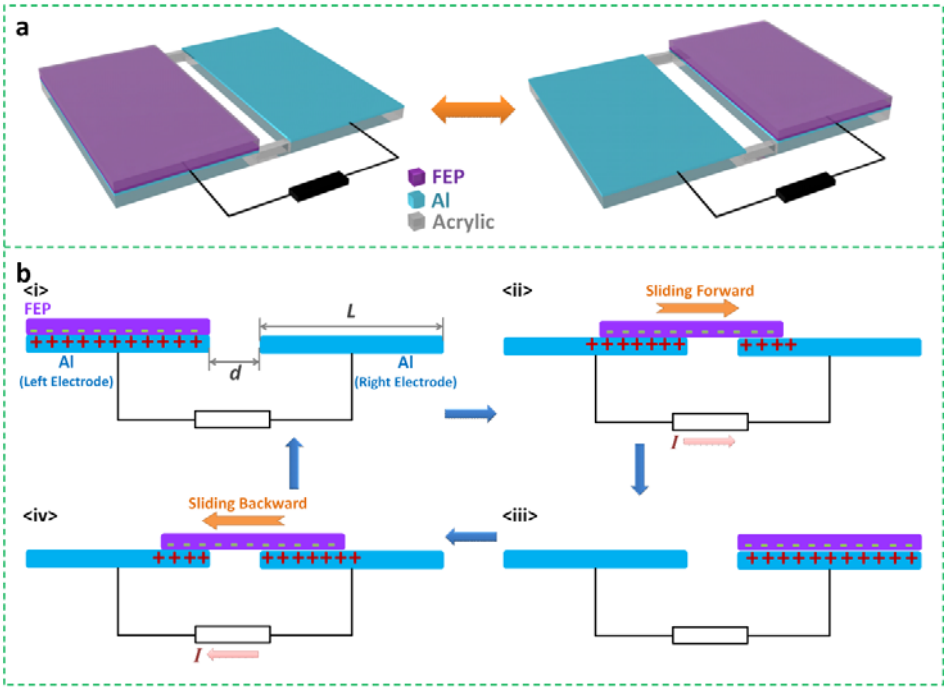

Figure 4.1 Device structure, basic operations and working principles of the dielectric-conductor based freestanding-layer-mode TENG (FTENG). (a) Typical device structure. (b) Schematic working principle.

4.1.2 Theoretical Model and Numerical Simulation

The theoretical model of FTENGs has been established to simulate the change of the open-circuit voltage (V_{OC}) between the two electrodes, as induced by the sliding of the freestanding triboelectric layer (Figure 4.2a).[91] In this model constructed in COMSOL, two metal films as the electrodes (with the length L = 5 cm and a thickness of 10 μm) are placed on the same plane, with distance d = 0.02 and L = 0.1 cm. At the initial state, the FEP film (with an assumed tribo-charge density (σ_{Tribo}) of 60 μC/m^2, which is chosen based on the level of the actual σ_{Tribo} on the FEP layer) is sitting on top of the left electrode (LE). All of the positive tribo-charges are assumed to distribute on the LE, in order to reach the electrostatic equilibrium at the initial state. As expected, the simulation result shows no potential difference across the electrodes (Fig. 4.2a<i>). Then, when the FEP film with negative surface charges slides to the middle position (with the displacement x = 0.51L), a large potential difference (V_{OC}) of ~40 kV is generated between the two electrodes in the open-circuit condition (Fig. 4.2a<ii>). Finally, when the FEP gets to the overlapping position of the RE, the V_{OC} will increase to ~86 kV (Fig. 4.2a<iii>). Such an increase of potential difference between the two electrodes is the driving force of the current flowing from the LE to the RE during the sliding.

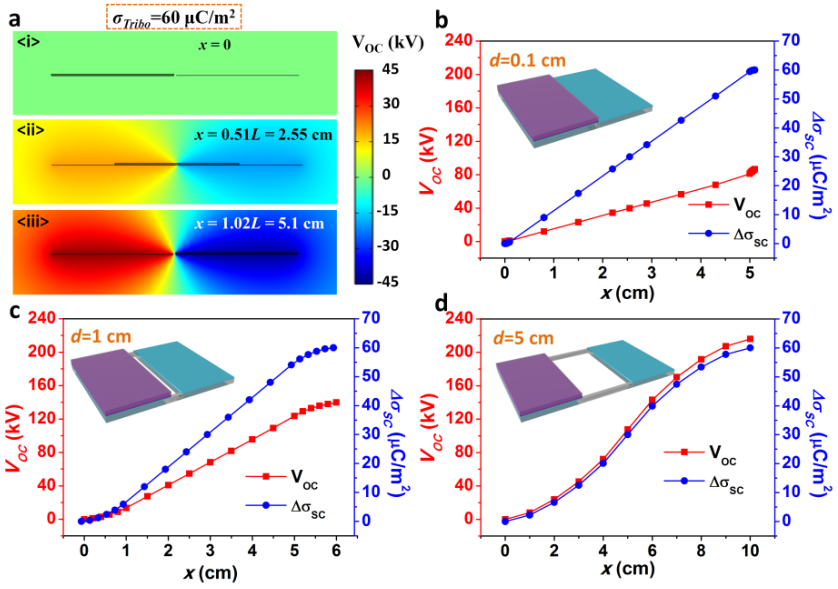

Figure 4.2 Theoretical model and study of FTENGs. (a) The simulated potential distributions at three different sliding displacements (0, 2.55 cm and 5.1 cm) of a FTENG with an electrode length of 5 cm and an electrode distance of 0.1 cm. (b-d) The simulated open-circuit voltages (V_{OC}) and transferred change densities ($\Delta\sigma_{SC}$) at different sliding displacements (x) of 3 FTENGs with the same electrode size (L = 5 cm) but different electrode distances (d): (b) d = 0.1 cm; (c) d = 1 cm; (d) d = 5 cm. The insets are the schematics showing the corresponding FTENG structures.

The most important structural parameter of the FTENGs is the distance (d) between two electrodes, which will also directly determine the necessary sliding displacement for achieving a full cycle of electricity generation. The output characteristics of V_{OC} and $\Delta\sigma_{SC}$ (the transferred charge density in each sliding motion) with the increase of the sliding displacements (x) were theoretically studied for three typical structures with different electrode distances of 0.1 cm (Fig. 4.2b), 1 cm (Fig. 4.2c), and 5 cm (Fig. 4.2d), respectively. As shown in the COMSOL simulation results (Fig. 2b-d), V_{OC} and $\Delta\sigma_{SC}$ generated by all of the three structures gradually increase with the increase of x, following symmetric profiles. As for charge transfer, $\Delta\sigma_{SC}$ will approach the same value (60 μC/m^2) of the tribo-charge density on FEP film, when a full sliding motion is completed. As for the calculated V_{OC}, the electrode distance does have a direct influence: when d increases from 0.1 cm to 5 cm, V_{OC} goes up from 86 kV to 216 kV. This effect can be understood from the general relationship of V_{OC} and $\Delta\sigma_{SC}$ in a TENG device,[72,83] shown as follows:

$$V_{OC} = \frac{\Delta\sigma_{SC} \cdot S}{C} \tag{4.1}$$

where S is the area of one electrode, and C is the capacitance between the two electrodes. Since $\Delta\sigma_{SC}$ and S are both constant, V_{OC} is inversely proportional to C. Because a larger distance between two electrodes will lower the value of C, V_{OC} should get higher as a result. Moreover, since two electrodes in a FTENG are stationary, C is approximately

kept as constant. Thus, V_{OC} and $\Delta\sigma_{SC}$ are proportional to each other and follow the same increasing trend in each device, which can be observed from Figure 4.2b-d. This inversely proportional relationship also clearly explains the reason for FTENGs' capability of generating such an extremely-high V_{OC}: that is the very small C from the two in-plane displaced metal plates. From this theoretical study, the FTENG is twice as efficient as the single-electrode TENG for mechanical energy harvesting.[92,93]

4.1.3 Electrical Outputs under Different Structural Parameters

The electrical outputs were measured from 5 devices with different electrode distances (0.1 cm, 0.3 cm, 1 cm, 3 cm, and 5 cm). As shown in Figure 4.3a, the 5 sets of $\Delta\sigma_{SC}$ all stay at the level around 65 μC/m^2, which is very similar to the theoretical expectation that d doesn't have an influence on the charge transfer. There is only a minor decreasing trend when d gets larger, probably because of a larger tribo-charge density (σ_{Tribo}) on FEP surface resulted from a more intensive friction when two electrodes get closer. However, the measured V_{OC} has a very different trend from the simulation results (Fig. 4.3b). Rather than showing a significant increase along with the elevation of d, the magnitudes of V_{OC} from these 5 devices are all around the level of 15 kV, only presenting a bit enhancement from the increase of d. Actually, the measured results are much smaller than the simulated values of V_{OC} by almost an order of magnitude. The possible cause of this difference is that the inner resistance of the electrometer is not infinitely large, so that real V_{OC} cannot be accurately recorded due to the internal leakage under such a high voltage. Thus, the measured results could not reflect the influence of d. As for the short-circuit current densities (J_{SC}) provided by these 5 FTENGs, since the total amounts of transferred charge densities are about the same for one sliding motion, J_{SC} should be mostly determined by the time span of one sliding. Therefore, the increase of d, which will lead to a longer sliding time, should be unfavorable for the magnitude of J_{SC}. This agrees with the measurement results of J_{SC} (Fig. 4.3c): the device with the smallest d

of 0.1 cm generates the highest J_{SC} of ~3.5 mA/m^2. Thus, from this influence of d, a smaller electrode distance is preferred in structural design for a high output power.

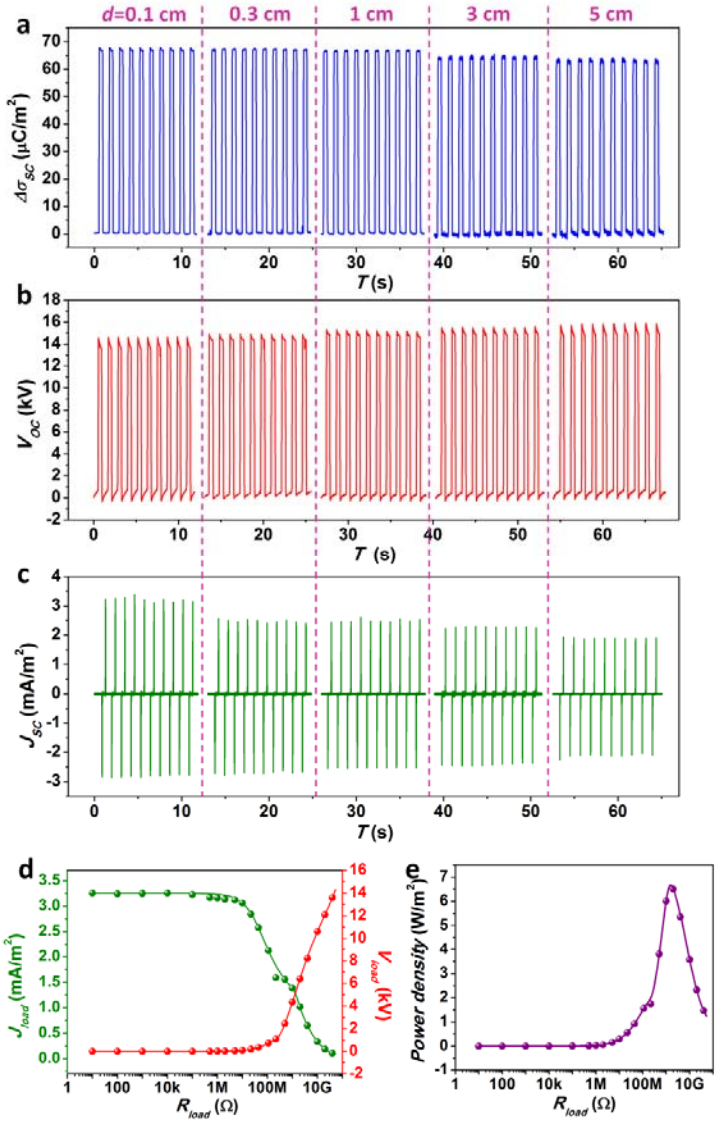

Figure 4.3 Measurement results of FTENGs' electrical outputs. (a) The transferred charge densities ($\Delta\sigma_{SC}$) of 5 FTENGs with different electrode distances (0.1 cm, 0.3 cm, 1 cm, 3 cm, 5 cm). (b) The open-circuit voltage (V_{OC}) of the above 5 FTENGs. (c) The short-circuit current density (J_{SC}) of the above 5 FTENGs. (d-e) The dependence of the electrical outputs on the load resistance, obtained from the FTENG with the electrode distance of 0.1 cm: (d) the voltage and the current density; (e) the power density.

For a comprehensively characterization of the demonstrated FTENG as a power source, we measured the actual voltages and current densities of a FTENG with d = 0.02L under a series of different load resistance. As shown in Figure 4.3d, at the range below 10 MΩ, both the voltage and the current density have little variation from the short-circuit condition. Then, a further increase of the resistance beyond 10 MΩ will lead to the increase of the voltage and the decrease of the current density. At the resistance of ~1 GΩ, the FTENG provides the maximum power density to a load, which is ~6.7 W/m^2 (Fig. 4.3e).

4.2 Dielectric-Dielectric Based Freestanding-Layer-Mode TENG

The other basic design of FTENGs is based on the triboelectrification between two different dielectric films, e.g. FEP as the freestanding layer and polyamide (Nylon) as the film fully covering the two stationary electrodes. This type of dielectric-to-dielectric (D-D) FTENG can be fabricated by simply depositing two electrode patches at the back side of the other dielectric film, which is chosen as Nylon because of its complete reverse triboelectric polarity with FEP film (Figure 4.4a). When the freestanding FEP film is driven to slide on top of the Nylon film, negative charges will be injected from the Nylon surface to the FEP surface. As for the positive static charges on the Nylon surface, since they are stationary all the time, their induced potentials on the two electrodes remain as constant, which cannot provide any driving force to the charge flow in the external load. Thus, all of the driving force of the current still comes from the sliding of the negatively-charged FEP film, which is the same as the demonstrated dielectric-conductor FTENG structure. Therefore, this dielectric-dielectric structure should generate electricity in a similar manner. The full schematic working principle is shown in Figure 4.4b.

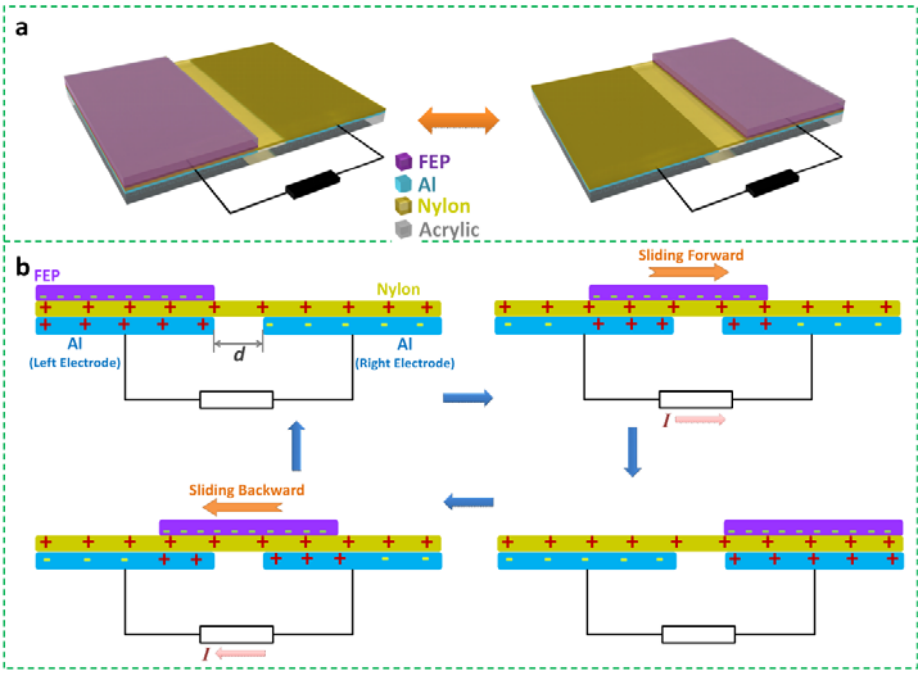

Figure 4.4 Device structure, basic operations and working principles of the dielectric-dielectric based freestanding-layer-mode TENG (FTENG). (a) Typical device structure. (b) Schematic working principle.

Similarly to the discussed dielectric-to-conductor (D-C) FTENG, a smaller distance between the two electrodes should be favorable. Thus, we studied the D-D FTENG with the same size (7 cm × 5 cm) as the D-C type and an electrode distance of 0.1 cm. Its basic working principle can be verified by the numerical calculation of the V_{OC} and the $\Delta\sigma_{SC}$ at different sliding displacements. From Figure 4.5a, they have very similar behaviors to those from the corresponding D-C FTENG structure of the same d (Fig. 4.2b). The addition of the dielectric layer attached to the two electrodes only leads to small decreases on V_{OC} (from 86.5 kV to 66.9 kV) and $\Delta\sigma_{SC}$ (from 60 μC/m^2 to 59.9 μC/m^2), which are possibly resulted from the slight separation of the sliding FEP layer and the electrode by the Nylon film. The D-D FTENG was also studied experimentally by measuring the electrical outputs from a real device. As shown in Figure 4.5b, the back-and-forth sliding of the FEP layer on the Nylon surface drove the alternating charge

flow with a density of ~55 μC/m^2. An open-voltage of ~12 kV (Fig. 4.5c) and a short-circuit current density of ~3 mA/m^2 (Fig. 4.5d) were obtained from the device. All of these three parameters are a little bit smaller than those from the D-C FTENG device.

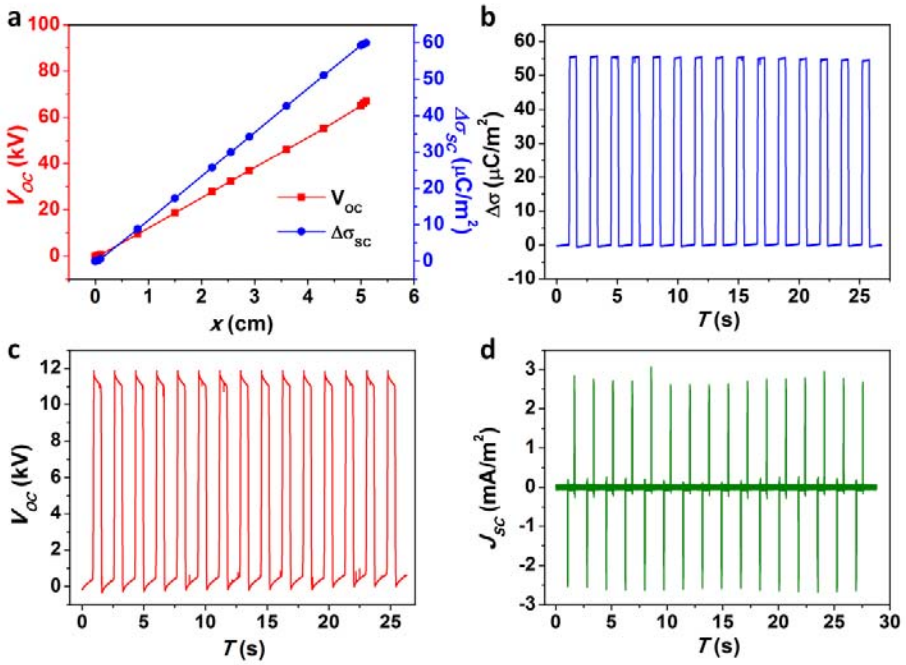

Figure 4.5 Simulation results and electrical measurements of dielectric-to-dielectric (D-D) FTENG. (a) The FEM simulated V_{OC} and $\Delta\sigma_{SC}$ at difference x, which are calculated from a D-D FTENG with an electrode length of 5 cm and an electrode distance of 0.1 cm. (b-d) The measured electrical outputs of a D-D FTENG with the above structural parameters: (b) the transferred charge densities ($\Delta\sigma_{SC}$); (c) the open-circuit voltage (V_{OC}); (d) the short-circuit current density (J_{SC}).

4.3 Non-Contact Sliding Mode for the Freestanding-Layer TENG

In order to design an efficient TENG, it is desirable to maintain an intimate contact between the freestanding triboelectric layer and the electrode films during sliding. However, in real applications of such sliding-based TENGs, it is sometimes difficult to keep a good in-plane contact during sliding, due to possible irregularities of input mechanical motions. In this freestanding-layer-mode TENG, if the dielectric FEP is

already charged due to prior-triboelectrification before approaching the electrodes, which may have or may not have electrostatic charges, electricity can be generated by swing the FEP between the two electrodes even without direct contact, with the full schematic working principle showing in Figure 4.6.[91] This is feasible because triboelectric charges can be preserved on insulator surfaces for hours and even days. As long as the vertical separation is much smaller than the relative displacement of the two electrodes (which could be on the order of several centimeters or even larger), the sliding of the non-mobile charges on the FEP film still can induce a significant portion of charges to flow. Thus, unlike existing TENGs, this new mode of FTENG should be able to operate in non-contact sliding mode.

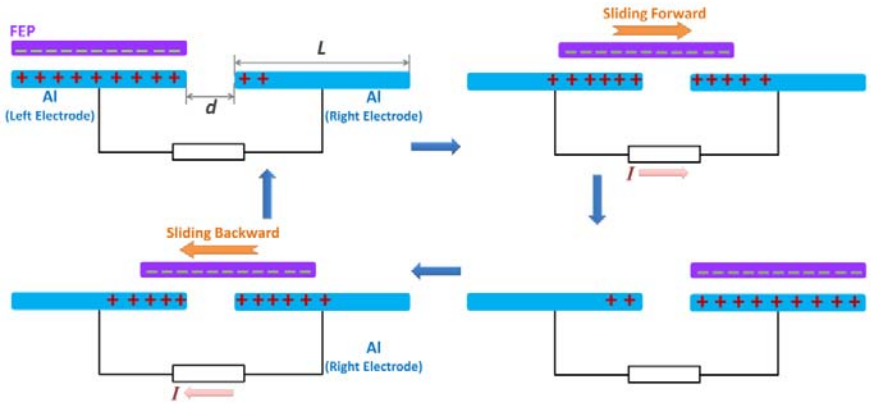

Figure 4.6 The schematics showing the basic working principle of a conductor-to-dielectric FTENG in non-contact mode.

Such a feature of operation in non-contact sliding mode comes from a good tolerance of a vertical separation between the two layers in electricity generation, which is critical for expanding TENGs' applications. We theoretically studied the influence of the vertical gap distance (H) between the two facing surfaces. As shown in Figure 4.7a, when H is increased from 0 to 10 mm, the calculated transferred charge densities ($\Delta\sigma_{SC}$) in one sliding motion still preserve a considerable portion of the maximum value ($\Delta\sigma_o$): 61% for the structure with d = 0.1 cm, and 77% for d = 5 cm. This set of calculation results gives us a good prediction that the presence of a vertical gap during sliding will

not have a severe influence on the effectiveness of mechanical energy harvesting. In order to verify this prediction experimentally, the transferred charge densities were measured from those two devices, under a series of different H between 0 and 10 mm. From the data in Figure 4.7b, although the measured outputs show a faster decay than the simulation results, the $\Delta\sigma_{SC}$ from the case of H = 10 mm still retains more than 20% of the maximum value (24% for d = 0.1 cm, and 29% for d = 5 cm). This higher decay rate of the measured output possibly comes from the reverse electrostatic-induction effect of the upper side of the acrylic substrate (with a thickness of 6.3 mm), which could carry some positive static charges due to its triboelectric polarity. The FTENGs' tolerance of the vertical separation between the sliding surface and the electrode should improve when the device dimensional (L) along the sliding direction increases. This tolerance of non-contact sliding is much better than traditional sliding-mode TENG in which one electrode is attached with the sliding triboelectric layer.[77] As shown in Figure 4.7c, when H increases to merely 2 mm, the $\Delta\sigma_{SC}$ from the traditional sliding TENG dramatically decays to almost 0. Therefore, a good tolerance of vertical separation is a unique feature of FTENGs.

With this capability of generating electricity by non-contact sliding, if the charges on the dielectric surface can preserve for a sufficiently long time, the FTENG will be able to continuously operate in this non-contact condition, under which there is no friction so that the energy conversion efficiency could achieve theoretically expected 100% (Supporting Information) although the actual output power is lowered. In the FTENG structure demonstrated in this paper, the material used for the freestanding triboelectric layer—FEP—is a type of electret (the category of materials that can quasi-permanently retain the static charges on them).[94,95] Thus, once the tribo-charges are generated on FEP by the contact sliding in the first few cycles, they can stay on the FEP surface to drive the flow of electricity without any further contact or friction between the two surfaces needed. In order to test the stability of the FTENG in the non-contact mode, we

continuously ran one FTENG for ~20,000 cycles with a vertical distance of 5 mm. As shown in Figure 4.7d, the generated short-circuit charge density of ~25 μC/m^2 didn't have an obvious decay after these ~20,000 cycles. The capability of working in non-contact mode provides a number of advantages for mechanical energy harvesting: extremely-high energy conversion efficiency (theoretically 100%) due to a low mechanical energy input that doesn't need to overcome the sliding friction; the minimized surface wearing from sliding friction; expanded types of applicable mechanical energies.

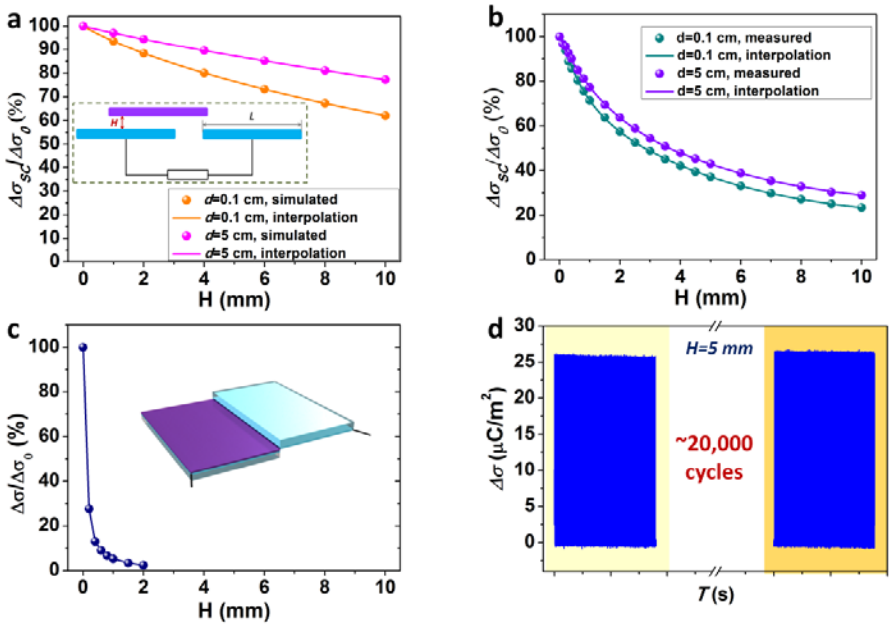

Figure 4.7 FTENGs' tolerance of vertical separation between the sliding triboelectric layer and the electrode surface. (a) The FEM simulated influence of the vertical separation (H) on the $\Delta\sigma_{SC}$ of two FTENG structures with d of 0.1 cm and 5 cm respectively. The dots are simulated $\Delta\sigma_{SC}$ at certain H, and the lines are the interpolation results. The inset is a 2-dimensional diagram showing the FTENG with a vertical gap. (b) The experimentally measured influence of the vertical separation (H) on the $\Delta\sigma_{SC}$ of the above two FTENGs. The dots are measurement results, and the lines are the interpolation results. (c) The influence of vertical separation on the traditional sliding TENG, in which one electrode is attached with the sliding triboelectric layer. The inset shows the structure of the tested sliding TENG of the same size and materials. In all the above three figures (a-c), $\Delta\sigma_0$ is the maximum transferred charge density of each FTENG in

contact-sliding mode. (d) The output stability of the FTENG working in non-contact sliding mode, over ~20,000 continuous cycles.

4.4 Application of the Freestanding-Layer-Mode TENG for Harvesting Energy from Free-Moving Objects

With the unique advantages of being able to be triggered by freestanding and non-contact sliding motions, the development of this new mode FTENG will largely expand the applications of this new technology for versatile mechanical energy harvesting.[91] Without a connection to the system by a lead wire, the objects as the energy sources can move freely without any constraint. This advantage has been demonstrated on generating electricity from the free sliding motions of a human hand. As covered by a FEP film on a hand, the sliding of the hand between two electrodes can effectively produce electricity, which is capable of instantaneously driving 100 commercial LEDs (Figure 4.8a). From the real-time measurement results shown in Figure 4.8b, the current through these 100 LEDs reaches ~8 μA. Because there is no electrical wire extending out, the hand can move to any place, without suffering from any inconvenience caused by the energy harvesting device. Another important feature of the FTENG is its capability to generate electricity from non-contact sliding. As shown in Figure 4.8c, the FTENG still can act as a direct power source for 100 LEDs, with a gap existing between the FEP surface and the electrode plane . These two features make FTENG an effective technology for harvesting mechanical energy from human walking without a constraint or contact (Fig. 4.8d). During the contacts with the ground while waking, the bottoms of human shoes are naturally charged. With a group of electrode patches laminated on the road surface along people's walking track, the feet can bring the shoe-sole-attached FEP films from one electrode to another, through which a current flow will be generated (as indicated by the LEDs connected between any two adjacent electrodes). Although the motion of people's foot is not a perfect in-plane sliding, it still can be effectively harvested by FTENGs in

non-contact mode. Moreover, because there is no need to connect a lead to a human foot, such a group of electrodes on the road can harvest the walking energy from anyone who steps on the pads. Such design can be extended to automobiles and trains.

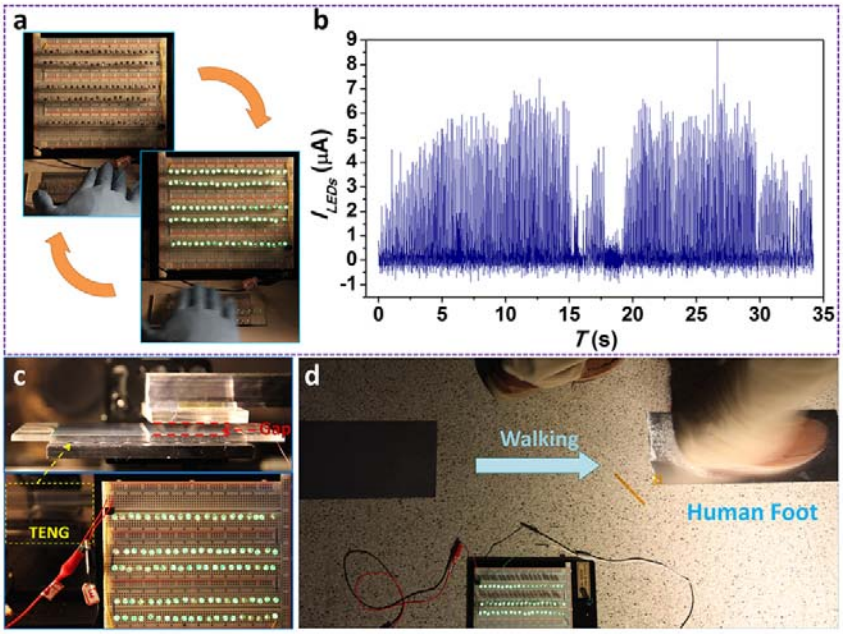

Figure 4.8 Niche applications of FTENGs for versatile mechanical energy harvesting. (a) Electrical energy generated by the sliding of a human hand without lead connection, which is capable of instantaneously driving 100 LEDs. (b) Real-time measurement of the current through these 100 LEDs, which is generated by the human hand. (c) 100 LEDs driven by a FTENG (marked by the yellow square in the lower picture) working in non-contact mode, with a vertical gap distance of 3 mm. The upper picture is the magnified portrait of the FTENG, clearly showing the gap between the two layers. (d) The concept of FTENG used for harvesting the walking energy from any people who step on the pads.

4.5 Grating-Structured Freestanding Triboelectric-Layer Nanogenerator

In the above demonstration of basic mechanism and structural design for the freestanding-layer-mode TENG, the device with two plate-electrodes and one entire triboelectric layer requires a relative large sliding displacement (the whole length of one electrode) to realize an effective electricity generation, which is unfavorable for its

achievable power output and energy scavenging in practical use. Since mechanical vibration in our environment is always irregular and varying in amplitude and frequency. For the improvement in the above two important aspects, we further demonstrated a linear grating-structured freestanding triboelectric-layer nanogenerator (GF-TENG) with largely-elevated output, high efficiency, and broad range of applications. This new design is composed of a grating-segmented triboelectric layer and two pairs of interdigitated electrodes, all in the same periodicity. Both of the theoretical analysis and experimental study indicated significant enhancement in the amount of collectable charges, current density, and output frequency through introducing finer grating segments.[96]

4.5.1 Structural Design and Basic Operation of the Grating-Structured Freestanding Triboelectric-Layer Nanogenerator (GF-TENG)

The structure of the GF-TENG is depicted in Figure 4.9a. The device mainly consists of two groups of components: a freestanding triboelectric layer with grating segments and two interdigitated metal electrodes. To enable an intensive electrification during contact, FEP and Al were chosen as the materials for the freestanding triboelectric layer and metal electrodes, respectively. In the fabrication of the freestanding part, an acrylic sheet was laser-cut into grating structures with N segments (N=8 for Figure 4.9a) as the supporting substrate for the triboelectric layer. Then, the FEP film was adhered to the substrate and cut into the same configuration. To enhance the contact electrification, nanorod structures (Fig. 4.9b) was introduced onto the surface of FEP film through ICP-RIE.[81] As for the metal-electrode part, another acrylic was patterned to N units of interdigitated structures with the same periodicity as the freestanding layer. After the deposition of Al film, two groups of grated-electrodes with the complimentary shape were obtained. The spacing between two adjacent electrode fingers was 1 mm in all the devices. For the GF-TENGs with different N, we maintained the total effective lengths (l_0) of the freestanding layer and each electrode group with the same value of 6.4 cm,

which makes sure these devices having the same total effective area (38.4 cm^2). Thus, the larger number of segments only brings about the smaller length (l) of each grating unit, with a relationship of $l=l_0/N$.

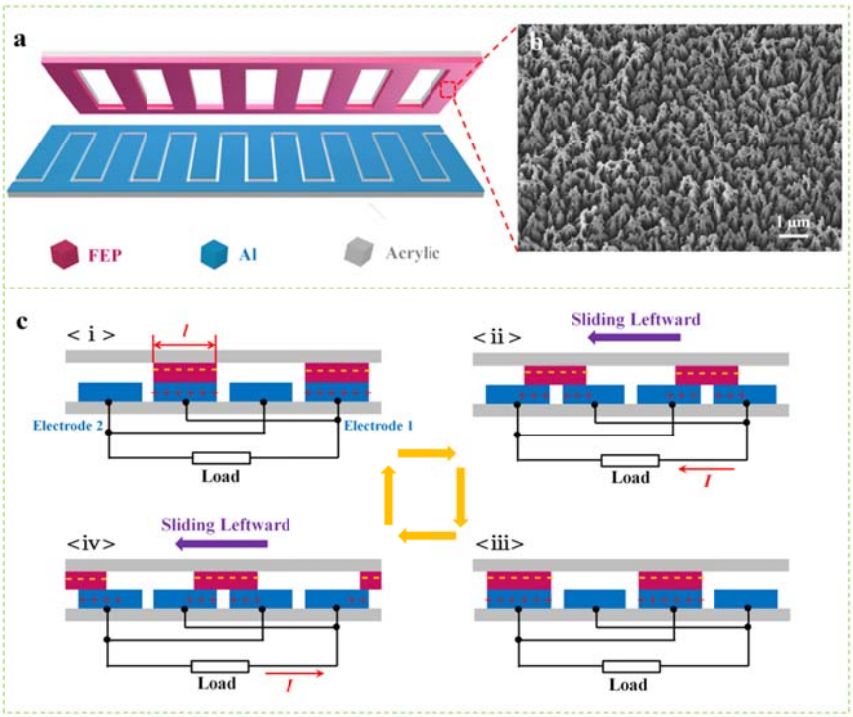

Figure 4.9 Device structure and operation mechanism of grating-structured freestanding triboelectric-layer nanogenerator (GF-TENG). (a) Typical structure design of GF-TENG. (b) SEM image of nanorod structure on the FEP surface. (c) Working mechanism of the GF-TENG.

The operation principle of the GF-TENG can be explained as the coupling of contact electrification and in-plane-sliding-induced charge transfer, as shown in Figure 1c. Initially, the grating rows of the FEP layer are brought into contact with the fingers of the electrode group (EG) 1 at a fully overlapping position (Fig. 4.9c<i>). The contact electrification between two surfaces occurs results in negative charges on the FEP surface and positive charges on the EG 1 with the equal amount. In this state, there is no charge flowing between the two electrodes due to the electrostatic equilibrium. When the FEP layer starts to slide leftward, this grated layer gradually moves from the overlapping

position of EG 1 to that of EG 2 (Fig. 4.9c<ii>). In this case, an electric potential drop is generated and drives positive charges flow from the EG 1 to the EG 2 along with the sliding motion, which produces a transient current in the external load. Once the FEP layer reaches the fully overlapping position with EG 2 (Fig. 4.9c<iii>), all of the positive charges transfer to this electrode, with another electrostatic equilibrium being achieved. This is one unit step of sliding. When the FEP continues to slide leftward to the EG 1 by another step (Fig. 4.9c<iv>), the positive charges will be electrostatically attracted to flow back to EG 1, bringing about a reverse current in the circuit. Therefore, an electricity generation cycle is completed. If the FEP is driven to slide rightward, a reverse process will take place.

4.5.2 Enhancement on the Electrical Output by the Grating Structure

To experimentally study the influence of the grating segmentations on the output performance, five devices with different grating segments (N=1, 2, 4, 8, 16) but the same effective area were fabricated, and their electrical characteristics were measured. Figure 4.10a shows the transferred charge density of the GF-TENGs with insets showing the enlargement profiles of one sliding cycle of each structure. A full sliding cycle is composed of two parts with the left part corresponding to a one-way sliding and the right one representing the backward process. It can be observed that tribo-charges are transferred (2N-1) times for the N segments device (e.g., 31 times for 16 segments) in a one-way process, which is accordant with the simulation work, although the maximum $\Delta\sigma_{SC}$ from the first step declines slightly with the increase of N. The trends may be ascribed to the uneven surface induced by the procedure of laser cutting of grating structure, which affects the effective contact area. By connecting the GF-TENGs with a bridge rectifier, all of the transferred charges can be accumulatively collected, e.g. in an energy storage device. As shown in Figure 4.10b, the accumulated charges have a largely-enhanced amount by increasing segment numbers because of multiplied charge

transfer cycles. When 16 segments are introduced, the $\Delta\sigma_{SC\text{-}Rec}$ goes up to 640 μC/m^2 which is over 10 times larger than that of 1 segment structure, demonstrating huge enhancement for the multiple segments device. As for the V_{OC}, the profiles display similar oscillation behaviors as the $\Delta\sigma_{SC}$ with a much more severe decaying tendency by the increase of N. This reflects the prediction in the theoretical analysis. The characteristics of the short-circuit current density (J_{SC}) were shown in Figure 4.10d, which were measured at a sliding acceleration of 10 m/s^2. For 1 segment device, only one low and wide current peak was generated by one unidirectional sliding step; when it comes to 16 segments structure, 31 sharp and narrow peaks are produced with a peak value of ~4.0 mA/m^2 from a similar one-way sliding step. The mean frequencies of the two GF-TENGs are about 7 and 130 Hz, respectively. The enhanced performance can be explained by the following equation:

$$J_{SC} = \frac{\mathrm{d}\Delta\sigma_{SC}}{\mathrm{d}t} \tag{4.2}$$

where t is the time. Since both of the length and the time for each unit step will be shorter when the segmentation number increases, tribo-charges can be transferred faster and hence the higher amplitude and frequency are achieved for the current. Therefore, introducing more grating segments in the structure will be favorable for the accumulation of charges, current density and frequency.

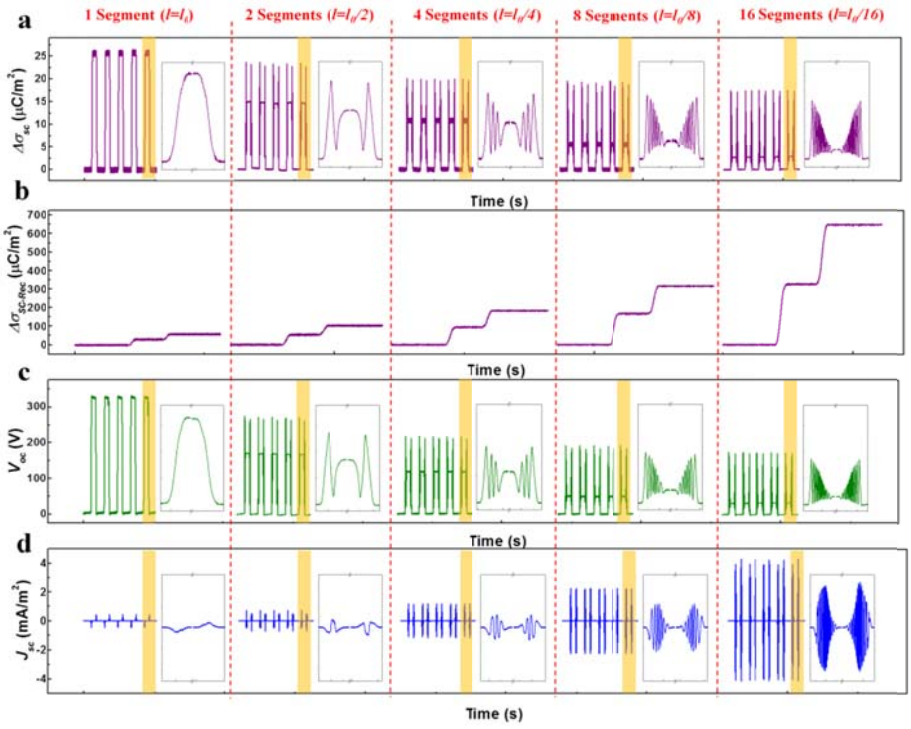

Figure 4.10 Electrical measurement results of GF-TENGs with different segment strucutres (N=1, 2, 4, 8, 16). (a) The measured $\Delta\sigma_{SC}$. (b) The measured $\Delta\sigma_{SC\text{-}Rec}$. (c) The simulated V_{OC}. (d) The simulated short-circuit current density (J_{SC}). The insets show the enlargement of the corresponding highlighted parts.

In the above case where the FEP layer and the electrode groups have the same number of units, the total effective area decreases while the FEP slides outwards, resulting in a damped oscillation behavior of $\Delta\sigma_{SC}$. In order to make the electricity generation more effective through maintaining the same effective area during the sliding of FEP, we fabricated an extended GF-TENG in which electrode part has the doubled number of units compared with the FEP layer. In this design, the FEP will always slides within the range of the electrodes (Fig. 4.11a). Figure 4.11b-e present the output performance of the extended GF-TENG with 16 grating segments. It can be observed that each unit step of sliding transfers almost the same amount of charges ($\Delta\sigma_{SC}$ = 16.5μC/m^2) between the two electrodes without any decay during an entire unidirectional sliding process (Fig. 4.11b). If these transferred charges are accumulated, $\Delta\sigma_{SC\text{-}Rec}$ can reach 1100

$\mu C/m^2$ in the process (Fig. 4.11c), which is nearly twice as large as that from the previous non-extended structure. A similar undamped oscillation behavior is observed for V_{OC}, although the amplitude (135 V) becomes smaller than the original one (Fig. 4.11d). The decrease can be ascribed to the increase of the total capacitance between two electrodes from the doubled number of electrode fingers, according to the equation 1. As for the current, keeping the acceleration at 10 m/s^2, the peak value of J_{SC} increases to 5.5 mA/m^2 due to the enhanced amount of the transferred charges. As a power source in practical use, the TENG will be connected with external loads. Therefore, the actual voltages and current densities on varied load resistances were measured and the results are summarized in Figure 4.11f. The current density (at the acceleration of 30 m/s^2) drops at larger external resistances, while the voltage across the load exhibits a reversed tendency. Accordingly, the power density that the device provides firstly rises at low resistance region and then declines at high resistance, showing a maximum value of 0.72 W/m^2 at the resistance of 5 MΩ (Fig. 4.11g).

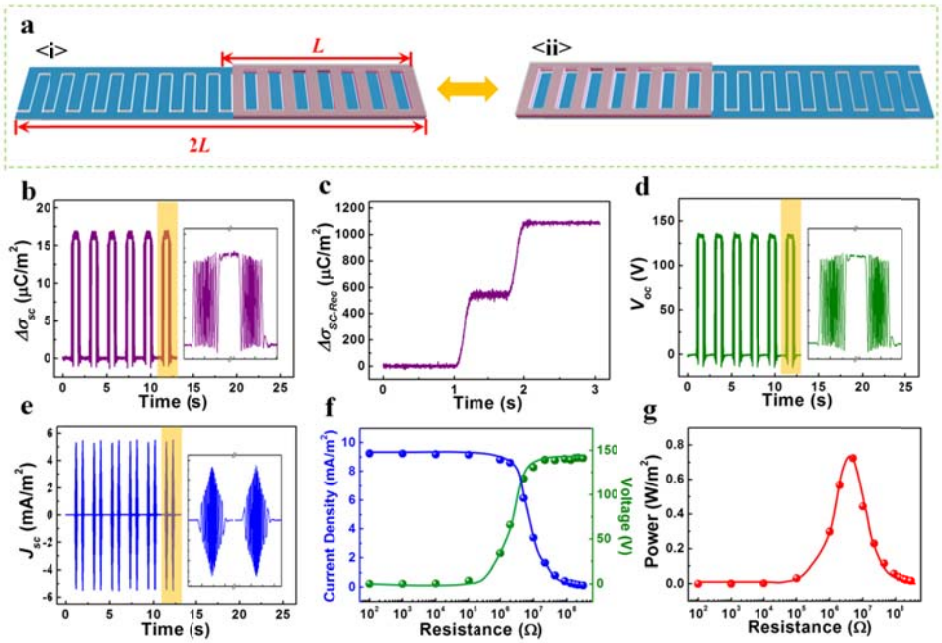

Figure 4.11 Electrical measurement results of the extended GF-TENGs. (a) The initial and final states of one-way sliding for a typical extended GF-TENG. (b-g) The measured results for the

extended GF-TENG with 16 segments: (b) The $\Delta\sigma_{SC}$; (c) The $\Delta\sigma_{SC\text{-}Rec}$; (d) The V_{OC}; (e) The J_{SC}; (f) The dependence of the output voltage, current density, and (g) power density on the resistance of the external load.

4.5.3 Application of the GF-TENG and the Total Energy Conversion Efficiency

With the unique advantages as demonstrated above, the GF-TENGs can be employed to harvest numerous kinds of mechanical energy existing in our environment and act as direct power sources for electronics. As shown in Figure 4.12a, after attaching a freestanding FEP film to a human hand, the hand can slide freely across the electrodes without any constrain. This movement can effectively generate electricity to light up 60 commercial LEDs instantaneously even under a slow speed and a small displacement. The GF-TENG can also be potentially utilized to harvest the vibration energies from moving vehicles. For the demonstration, a GF-TENG is installed to a remote control car. When the car was in the acceleration or deceleration, the GF-TENG can generate electricity for powering electronic components on the vehicle (Fig. 4.12b). The GF-TENG could also be used as a self-powered sensor for detecting the acceleration of moving vehicles. If the generator is fully sealed, it can be further applied to harvest wave/tidal energy from the sea.

Furthermore, the GF-TENG working in non-contact mode can harvest mechanical energy with high conversion efficiency. As shown in Figure 4.12c, four identical extension springs are used to position the FEP within the parallel plane to the surface of the electrodes with a distance of 1.6 mm. When the external mechanical motion applies onto the device along the spring direction, the FEP will oscillate around the equilibrium position for a long term without extra mechanical input, converting the stored mechanical energy in the spring into electricity. As shown in Figure 4.12d, this design can scavenge the mechanical energy from people's walking motion when it is bonded to human legs. It is noticed that each walking step will produce lasting and decaying electrical outputs in a

certain period, which corresponds to the damped oscillation of the FEP around the equilibrium position.

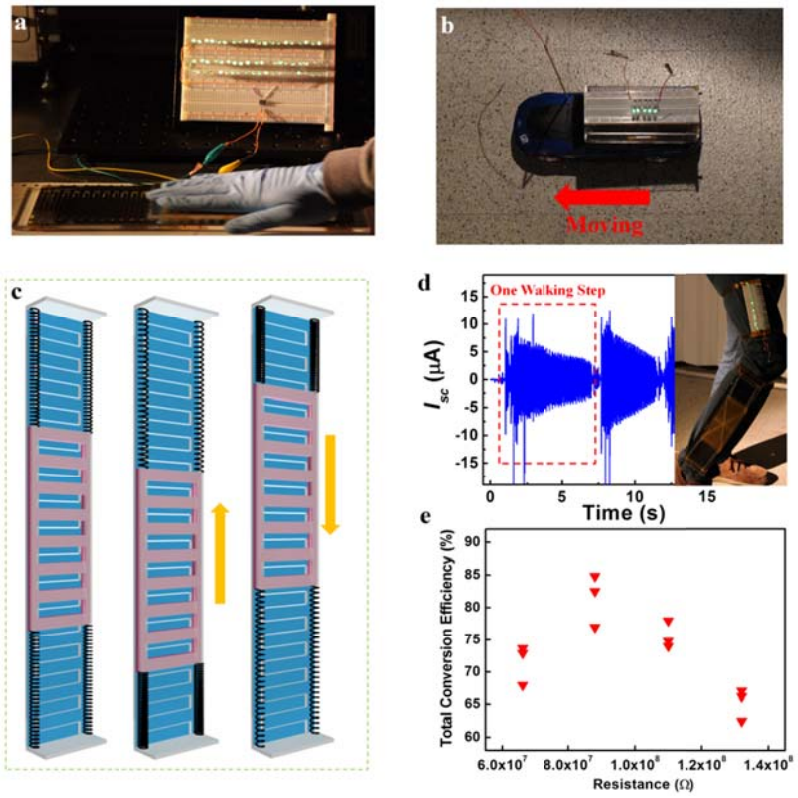

Figure 4.12 Applications of GF-TENG for harvesting a wide range of mechanical energy. (a) Harvesting energy from sliding of a human hand. (b) Harvesting energy from acceleration or deceleration of a remote control car. (c) Device structure for non-contact GF-TENG. (d) Harvesting energy from people walking by non-contact GF-TENG and the real-time measurement of short-circuit current (I_{SC}). (e) Total conversion efficiency of non-contact GF-TENG for harvesting slight vibration under different load resistances.

This spring-based device can also be utilized to estimate the conversion efficiency of the GF-TENG in non-contact mode. Here, total conversion efficiency is introduced and defined as the ratio of the total generated electrical power (by the instantaneous triggering and the residual mechanical vibration after the triggering) to the input mechanical power. Ideally, if there is not any friction in the environment, the theoretical total conversion efficiency of non-contact mode is expected to be 100%. During the

measurement, the FEP is initially pulled to a position with a small displacement (x=1 mm) relative to the equilibrium point, through which the mechanical energy is stored in the springs. When the FEP layer is released at this point, it will oscillate around the equilibrium position with gradually damping amplitude for ~4 min. In this process, the stored mechanical energy is gradually converted firstly to kinetic energy of the FEP and then to the electrical energy. Through measuring the electrical output on the external load, the total amount of electrical energy can be calculated. Similar to the power measurement in Figure 4.11g, the electrical energy obtained by the load reaches the maximum values at a certain resistance. Thus, we measured the current on a series of loads with different resistances in order to get the highest-achievable electrical energy and hence the efficiency. Therefore, the total generated electrical power can be calculated as:

$$E_{electrical} = \int I^2 \cdot R \cdot dt \tag{4.3}$$

where I is the instantaneous current which can be recorded by electrometer, R is the load resistance. As for the input mechanical energy, it will be determined by the difference between potential energy at initial position (x=1 mm) and finial position (equilibrium point), which can be calculated as:

$$E_{mechanical} = 2 \cdot k \cdot x^2 \tag{4.4}$$

where k is the spring constant (k = 15.76 N/m), x is the displacement (x = 1 mm). Figure 4.12e shows the estimated total conversion efficiency under different resistances from a number of repeated measurements. It can be observed that the highest efficiency reaches 85% at an external load of 88 MΩ! It clearly demonstrates the capability of harvesting mechanical energy at a very high efficiency by the freestanding-layer-mode triboelectric nanogenerator.

On basis of these advantages, the GF-TENG is capable of harvesting energy from a variety of ambient sources, such as sliding of human hand, acceleration of vehicles, and

people walking. This work represents a significant progress of TENG and exhibits huge potential of the GF-TENG as a high-efficiency energy harvester for practical applications.

4.6 Non-Contact Free-Rotating Disk TENG Based on Freestanding-Layer-Mode

We further expanded this freestanding-layer-mode mechanism to segmentally-patterned disk structures for harvesting energy from free-rotating objects in possibly non-contact mode.[97] This can overcome the two limitations of the previously-demonstrated sliding-mode based disk TENG: 1) both the rotational and stationary triboelectric layers require deposition of metal electrodes and connection with electrical leads, leading to inconvenient operation of the rotational part; 2) intimate contact is mandatory to achieve efficient electricity generation, which results in possible material abrasion, instability of output, and limited life time of the TENG.

4.6.1 Structural Design of the Free-Rotating Disk TENG

As schematically illustrated in Figure 4.13a, the basic structure of the FRD-TENG consists of two parts: the freestanding rotational part of tribo-charged layer, and the stationary part of metal electrodes. The rotational part was fabricated from a piece of FEP thin film (~ 50 μm in thickness), which was tailored into a four-segment structure and attached onto an acrylic supporting substrate with same shape. In this new structure, there is no need to deposit electrode on the back surface of the FEP membrane. The stationary part is composed of two separated aluminum foils with complementary four-segment shapes attached on a round-shape acrylic disk, which act as the two stationary electrodes. To increase the density of triboelectric charges through enhanced electrification process, micro-patterned structures were introduced on the inner surface of both triboelectric layers, respectively, as shown in Figures 4.13b and c. The two triboelectric layers were first brought into contact to produce triboelectric charges through the transfer of electrons from the surface of aluminum to FEP. The surface charges on the dielectric FEP would

remain almost unchanged for days, and then the device could be continuously working even when the two layers were not in contact. This is the initial step to have the two surfaces being electrostatically charged with opposite signs of charges, respectively. The length of time that the electrostatic charges are preserved on the surfaces depends on the nature of the materials and condition in environment such as humidity.

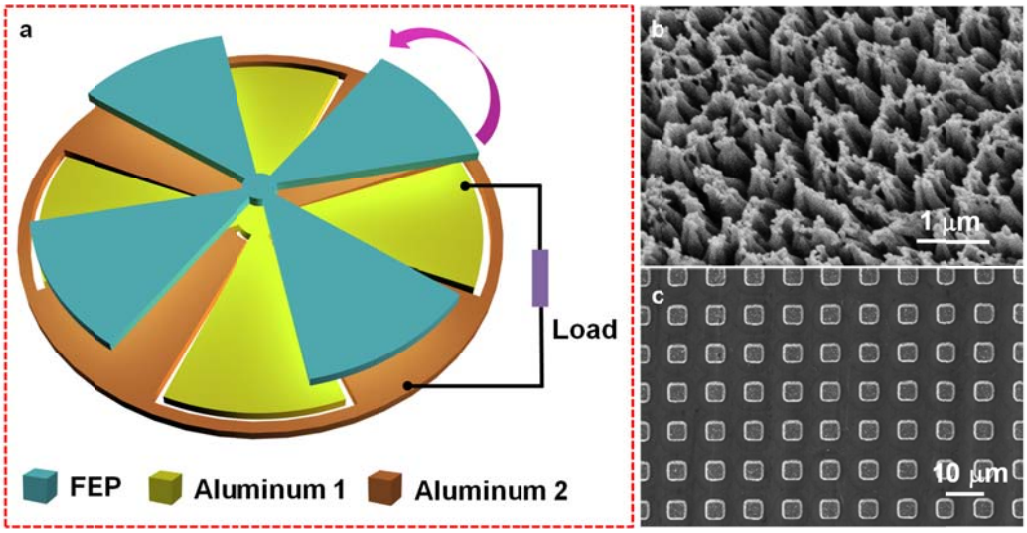

Figure 4.13 Device structure of the non-contact free-rotating disk triboelectric nanogenerator. (a) The schematic of the basic structure of the FRD-TENG composed of the freestanding FEP layer and the stationary aluminum layer. The bottom inset is the figure legend. (b) A 30˚-tilted-view SEM image of the nanorod structure created on the surface of the FEP thin film. (c) A top view SEM image of the cubic micro-patterned structures on the aluminum foil.

The working principle of the FRD-TENG is very similar with the freestanding-layer-based TENG for harvesting energy from sliding motion. After the freestanding FEP layer on the rotor part gets triboelectrically-charged through rotating against the Al electrode, it can generate electricity in both contact and non-contact rotation mode. The negative charges on the segmentally-patterned FEP surfaces rotate from the overlapping position of one electrode group to the other, the positive charges in the electrode loop will be electrostatically attracted to transfer through the external load along with the rotation of the FEP layer. When the FEP layer keeps rotating under the driving of surrounding

mechanical energy, the continuous alternating-current flow will be generated in the external load. This working principle is schematically depicted in Figure 4.14.

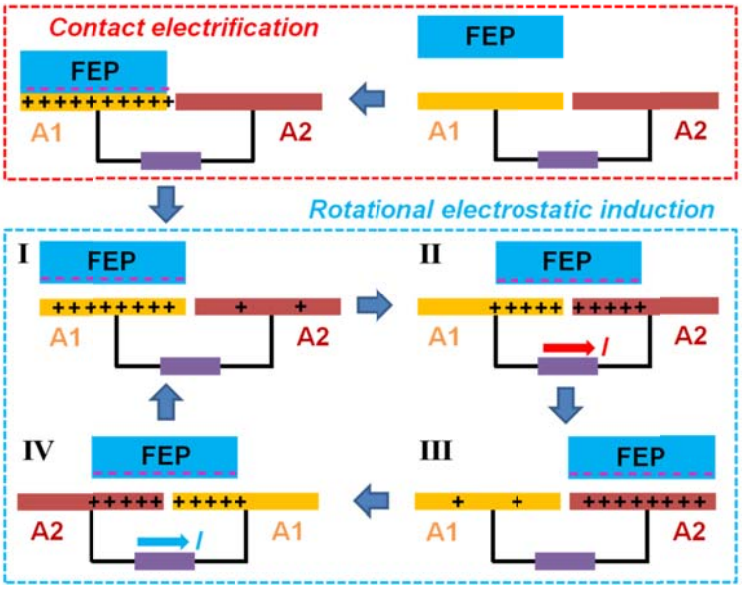

Figure 4.14 The working principle of the FRD-TENG in a full cyclic motion of the rotational disk.

4.6.2 Electrical Output of the Free-Rotating Disk TENG in both Contact and Non-Contact Mode

The typical output characteristics of the FRD-TENG operated at 500 rpm are presented in Figure 4.15b, and were compared with the corresponding output performances at contact-mode (Fig. 4.15a). Figure 4.15a1-3 shows the open-circuit voltage (V_{OC}), the transferred charge density (Q_{SC}), and the short-circuit current density (J_{SC}) of the TENG under contact mode (d = 0), respectively. Under this condition it can be found that V_{OC} = 250 V, Q_{SC} =21 μC/m^2, and J_{SC} =2.0 mA/m^2. The corresponding measurement results of the non-contact mode (d = 0.5 mm) are shown in Figure 4.15b1-3. The output performances for the non-contact mode are only slightly lower than those for the contact mode, with V_{OC} = 220 V, Q_{SC} =20 μC/m^2, and J_{SC} =1.8 mA/m^2. These results elucidate the FRD-TENG's capability of effectively generating electricity without further friction, indicating that a tight contact during the energy conversion process is no-

longer necessary. Specifically, it can be found that the output profiles of both the V_{OC} and the Q_{SC} are triangular waveform, while the J_{SC} yields square waveform (Insets of Figure 4.15b), which reflects the time-differentiation relationship between the transferred charges and the current. To gain a comprehensive view of the effective output power on the external load, we conducted the measurement of the output voltage and current with variable load resistances, as shown in Figure 4.15c. Generally, the output voltage increases with the loading resistance while the output current exhibits an opposite trend. Both curves have a quasi-linear region between 0.1 Mohm and 100 Mohm, where their variations with the loading resistance become significant. The output power with different resistances could be calculated by simply multiplying the as-measured data of the output current and voltage, as summarized in Figure 4.15d. Based on this result, it can be found that the maximum output power density of the FRD-TENG is 1.22 W/m^2, at a load resistance of ~ 2 Mohm. The high output power of the FRD-TENG can be utilized for instantaneously and continuously driving 100 LEDs in serial connection, as shown in Figure 4.15e, implying its applications as a self-lighting disk for security monitoring, wind detection, or amusement purposes.

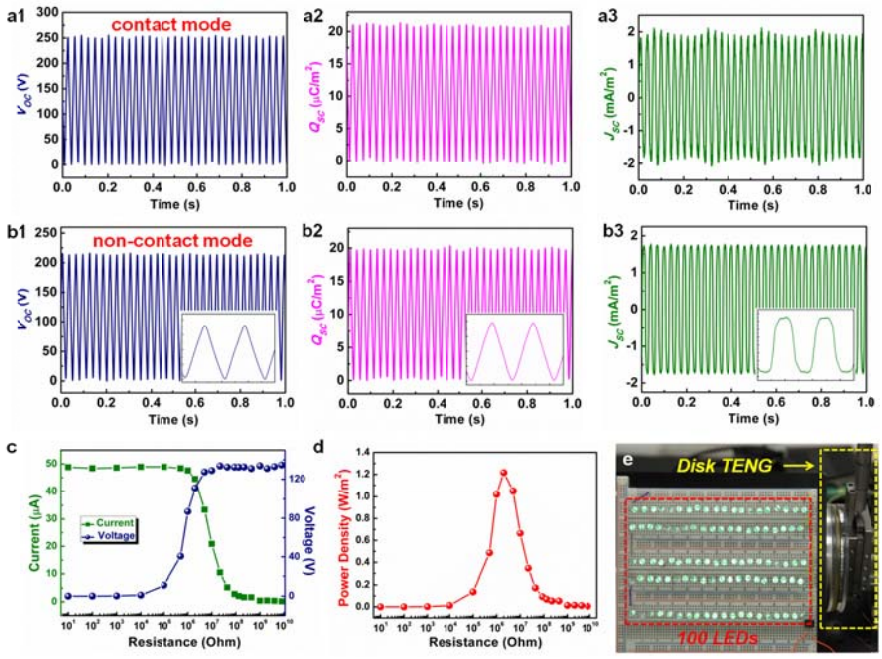

Figure 4.15 Electrical output characteristics of the FRD-TENG. (a1-a3) The measured V_{OC}, Q_{SC}, and J_{SC} of the FRD-TENG at contact mode, respectively. (b1-b3) The measured V_{OC}, Q_{SC}, and J_{SC} of the FRD-TENG at non-contact mode, respectively. The insets are the enlarged view showing the detailed shape of each output profile. (c) The measured output voltage and current across an external load with variable resistances. (d) The calculated effective power output of the FRD-TENG with variable resistances. (e) A snapshot from the video showing that the FRD-TENG is able to power up 100 serially-connected LED instantaneously and continuously.

4.6.3 Supreme Stability of the Free-Rotating Disk TENG in Non-Contact Mode

Owing to its unique working principle and the non-contact operation capability, the FRD-TENG has significant advantages compared to the previously-demonstrated D-TENG, in the durability of device structure, the stability of its electrical output (especially at very high rotation speed), and the energy conversion efficiency. To demonstrate this superiority of the FRD-TENG, the stability tests were carried out on a device with an eight-segment structure (inset of Fig. 4.16a), at a rotation speed of 3000 rpm. At first, all of the three output parameters of the FRD-TENG were measured before and after a 500,000-cycle continuous operation, and it is obvious that they all (Fig. 4.16a-b) display little drops after the 500,000 cycles of operation. Such a supreme stability is resulted from the elimination of the surface abrasion during the non-contact operation. The SEM images of the FEP microstructures were taken after 10, 20, and 50 hours of operation in the FRD-TENG, as shown in Figure 4.16c. It can be observed that the polymer nanorods were rarely affected by the huge numbers of electricity generation cycles, indicating the super-high durability of the device structure at the micro-scale.

For most of the energy harvesting techniques, it is needed to store the power scavenged from the environment in an energy storage unit, like a capacitor or a LIB. Because of the unique stability of the FRD-TENG, it can effectively charge a home-made LIB ($LiFePO_4$ as the cathode and TiO_2 as the anode) after rectification, which takes much longer charging time than a capacitor. The charging circuit diagram is shown in Figure

4.12d. From the measured charging curve in Figure 4.16e, it can be found that the LIB was successfully charged from 0.7 V (indicating an empty capacity for this battery system) to over 2.5 V (indicating a full capacity) in less than 1.5 hours, by the FRD-TENG operated under the rotation speed of 1000 rpm. The fully charged LIB can provide a constant current of 1 μA for around 10 hours. From this battery charging-discharging cycle, the the equivalent constant DC current (I_{equ}) of the TENG can be estimated as 7.5 μA, which is ~ 41% of the peak value of the rectified current (Fig. 4.16f).

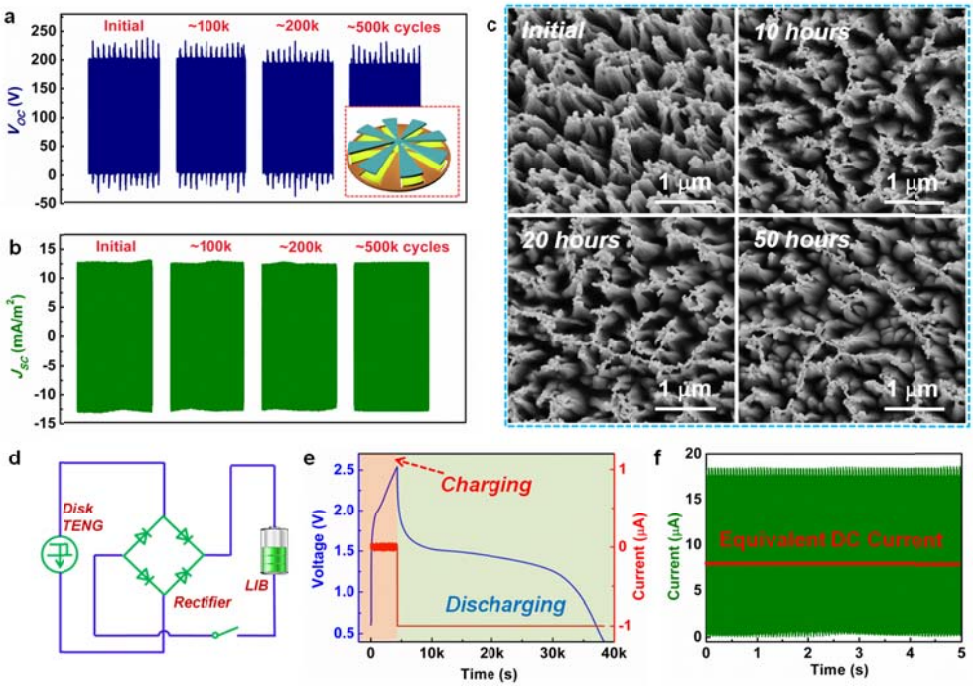

Figure 4.16 Stability tests of the FRD-TENG and its application for charging a lithium ion battery. (a) The measured results of the V_{OC} after the FRD-TENG had been continuously working for 100,000, 200,000, and 500,000 cycles, respectively. The inset shows the schematic structure of the eight-segment device used in this test. (b) The measured results of the J_{SC} after the FRD-TENG has been continuously working for 100,000, 200,000, and 500,000 cycles, respectively. (c) The SEM images of the nanorod structures on the FEP thin film after the FRD-TENG was continuously operated for 10, 20, and 50 hours, respectively. (d) The schematic circuit diagram for charging a LIB using the FRD-TENG. (e) The measured charging and discharging curve of the LIB as it was first charged by the FRD-TENG at 1000 rpm and consequently discharged at a

constant current of 1 μA. (f) The measured rectified output current of the FRD-TENG at 1000 rpm. The red line indicates the equivalent DC charging current calculated from the charging curve of the LIB.

From the above results, we can find that the free-rotating disk TENG is an efficient, stable and versatile structure to convert rotational mechanical energy into electricity.[97]

CHAPTER 5

MAXIMUM SURFACE CHARGE DENSITY FOR TRIBOELECTRIC NANOGENERATORS

From the previous theoretical analysis and experimental demonstrations of the three fundamental modes for triboelectric nanogenerators, it can be noticed that the surface triboelectric charge density is the most important factor for the output power density. This density of the static surface charges on the triboelectric layer not only directly determines the amount of the transferred charges through the external load (or stored in energy storage units) in each operation cycle, but also proportionally influences both the short-circuit current density and the open-circuit voltage.[44,77,91] As a result, a TENG's power density has a quadratic dependence on the surface charge density. Thus, in order to improve the output performance of TENGs, increasing the surface charge density is one of the most effective and indispensable approaches. On the other hand, because surface charges will generate the electrical field in the surrounding media, the achievable charge density will be limited by the breakdown of the air in the proximity region. Thus, in a certain TENG structure, there should exist a maximum surface charge density that results in the electrical field equaling to the threshold for air breakdown. For the purpose of improving the surface charge density to a level as high as possible, it is highly desirable to know the theoretical value and the influencing structural factors of this maximum surface charge density. Therefore, both the theoretical analysis and the experimental study of the maximum surface charge density is critically important.

In triboelectric nanogenerators, the static surface charges are brought by the triboelectrification process between the two different surfaces while they are in contact. According to the current understanding of the triboelectrification, the driving force for the charge transfer from one surface to the other is the difference of the surface chemical potentials. Thus, the density of the generated surface charges is primarily determined by

the intrinsic properties of the materials and/or surfaces. For example, in most of the previously demonstrated TENG designs, the triboelectric layers are FEP (or PTFE) and Al respectively. The FEP is the polymer that terminated with the functional group of fluoro (Fig. 5.1a), which is the most electronegative functional group and thus provides the strongest attraction to electrons. When a FEP layer gets into contact with an Al film—the metal that is easy to lose electrons, the difference in the surface chemical potentials will drive the electrons to transfer from Al to FEP. After the two films being separated, the FEP film will have negative surface charges as a result of the above electron transfer process. Although this triboelectrification process is very effective in generate the static surface charges to harvest mechanical energy, it is not best choice for the study of the maximum surface charges for TENG, for the reasons lying in the following aspects. First, limited by the surface potential difference between conventional materials, the triboelectric charge density generally cannot reach a very high level to approach the maximum surface charge density. Also, as determined by the intrinsic property of the two surfaces, the triboelectric charge density cannot be directly controlled or varied without changing the utilized materials, which is very inconvenient for the experimental study of the maximum surface charge density. More importantly, in the triboelectrification-enabled generator, the generation of the surface charge and the conversion of the mechanical energy are taking place concurrently, so that it can hardly be told whether the surface charge density is limited by the chemical potential difference or by the air breakdown. Thus, it is important to use new approach to introduce the surface charges that can facilitate the study of the maximum surface charge density for TENGs

5.1 Introduction of Static Surface Charges by the Injection of Ions from the Corona Discharging of the Air

Because the kernel operation principle of the TENG is an electrostatic induction process under the relative movement of the surface with static charges, the static charges

on the surface could be introduced by other approaches than the triboelectrification, to enable the same electricity generation process. One possible method is to directly inject single-polarity charged particles or ions on to the surface. In the dielectric materials, there is one category named as electret, that can quasi-permanently preserve the charges on the surface for a very long time (could be as long as several years). After the surfaces of these materials being pre-injected with charged particles and ions, they can operate as the induction source for the mechanical energy harvesting for a sufficiently long time, without the need of charging the surface again. In this way, the static charge generation process and the electricity generation process could be sequentially-separated, which will make the study of the maximum surface charge density for TENGs much easier. Also, without being limited by the chemical potential difference between the two surfaces, the surface charge density could reach an unprecedentedly high level, which could not only facilitate the study of the maximum charge density, but also help to build ultra-high-output TENGs.

From this regard, we chose to inject ions formed from the electrostatic/corona discharging of air onto the electret surface, for the introduction of the surface charges.[98] This was achieved by utilizing a special tool—an electrostatic gun, which can produces ions of both polarities through triggering the discharge of air inside the gun. The polarity of the ions injected from the gun's outlet can be manually controlled by either squeezing or releasing of the trigger bar. Using this method, the negative charges were brought onto the surface of FEP (which is also an electret material), as shown in Figure 5.1b. The trigger of the gun was firstly squeezed with the outlet of the gun facing away from the surface of FEP, during which the positive ions (mainly composed of $(H_2O)_2H^+$)[99] were injected from the outlet. Subsequently, while keeping the trigger at the squeezed position, we moved the outlet of the gun to directly face the FEP surface with a vertical distance of ~3 cm. Then the trigger will be gently released. During this process, the negative ions (CO_3^-, NO_3^-, NO_2^-, O_3^- and O_2^-)[99] were injected onto the surface of FEP, making it

negatively charged. This surface charges introduced by this method do not rely on the chemical property of the surface. Through injecting the ions for multiple times, the negative charges on the surface can reach a very high level, which can possibly approach the level for the breakdown of the air. Then, by assembling the negatively pre-charged film into a TENG structure, these negative static charges can electrostatically induce the electricity generation process under the application of surrounding mechanical motions.

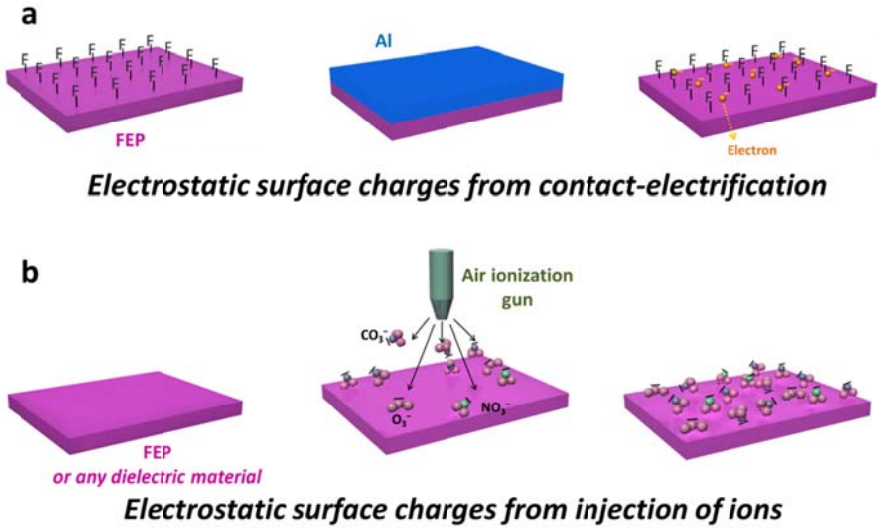

Figure 5.1 The comparison between the generation of the static surface charges on the FEP film by (a) the triboelectrification process and (b) the injection of the ions from corona discharging of the air.

5.2 The Ion Injection Process and Its Utilization in a TENG for Harvesting Mechanical Energy

5.2.1 Ion-Injection Process for the FEP Film Utilized in a Contact-Mode TENG

Using this method, we enhanced the power output and studied the maximum surface charge density for the vertical contact-separation-mode TENG. In the basic structural design of the TENG in this mode, the dielectric layer (e.g. the FEP film used in this study) is deposited with a layer of electrode on the back. During the ion-injection

process, it is critically important to connect the bottom electrode to the ground in order to reach a high surface charge density. In this way, the arrival of the negative ions onto the surface will electrostatically induce the electrons in the bottom electrode to transfer to the ground, thus making the bottom electrode positively charged (Fig. 5.2a). In order to achieve a zero potential difference between the bottom electrode and the ground, the induced positive charges in the bottom electrode will be equal to the amount of negative charges brought to the FEP surface by ion injection. As a result, the double-layered opposite charges will confine the electrical field within the FEP layer, leaving no electrical field in the proximity region of air. Because the dielectric strength ($\sim 2.6\times10^{8}$ V/m) of FEP is almost two orders higher than that (3×10^{6} V/m) of the air, the charge density on FEP surface from this ion-injection process can reach a much higher level than that on an electrode-free FEP layer in which the achievable charge density through ion-injection will be limited by the breakdown of the air. After such an ion-injection process is taken for a few times, the negative surfaces charges on the FEP will reach a large density, which equals to the density of the positive charges on the bottom electrode (Fig. 5.2b).

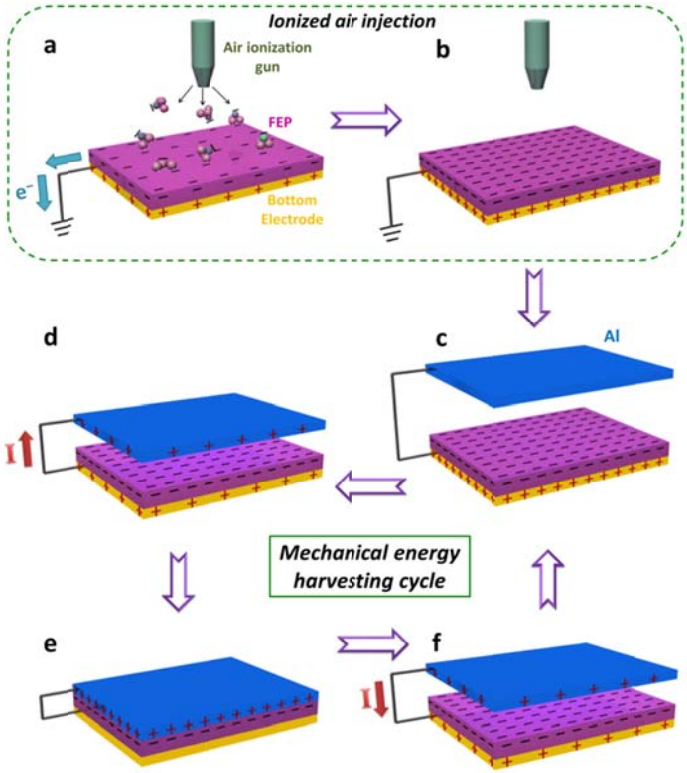

Figure 5.2 Basic processes of the ion injection on the FEP film and the operation of the contact-mode TENG built using this FEP film. (a) Injecting the negative ions onto the FEP surface from an air ionization gun. The bottom electrode attached to the FEP film is grounded during this process so that the positive charges can be induced onto the electrode to screen the electrical field from the injected negative charges on the FEP surface. (b) When the ion-injection is completed, the FEP surface and its bottom electrode have the opposite charges with the same density. (c-f) The ion-injected FEP/electrode double layer is assembled with an Al layer to form a contact-mode TENG, with 4 springs supported in between to get them separated (not shown in the figure). The electricity generation cycle of this contact-mode TENG under the periodic deformation force is shown in these four schematic images.

5.2.2 Mechanical Energy Harvesting Process of the Contact-Mode TENG with the Ion-Injected FEP film

Then, this FEP/electrode double layer will be assembled with an Al layer of the same size in a face-to-face configuration to form a vertical contact-separation mode

TENG, as shown in Figure 5.2c. A set of four springs will work with two acrylic supporting substrates to keep the Al plate separated from the FEP layer at deformation-free condition. The vertical-to-plane distance is much larger than the thickness of the FEP film. The Al plate as the top electrode is connected to the bottom electrode through external load. Then, under the triggering of surrounding mechanical motion, the negative charges on the FEP layer can generate the electricity in the load, following the similar mechanism of a vertical contact-separation mode TENG. When the mechanical motion of the surrounding objects provides a pressing force onto the Al plate, it will move towards the FEP layer. As their vertical-to-plane distance reaches the level that can be comparable to the thickness of the FEP film, the induced potential difference between the two electrodes will drive the positive charges on the bottom electrode to transfer onto the Al layer through the external circuitry, which generates the electricity in the first half cycle (Fig. 5.2d). This electricity generation process will last until the Al layer gets into fully contact with the FEP surface. At this very moment, all the positive charges have transferred from the bottom electrode onto the lower surface of the Al, so that they will locate at the same plane with the negative charges on the FEP surface (Fig. 5.2e). Subsequently, when the pressing force is released, the Al layer will start to get separated from the FEP surface due to the resilience of the springs, creating a potential difference between the two electrodes because of the separation of the opposite charges. As a result, the positive charges will transfer back from the Al layer to the bottom electrode of FEP, producing the second current pulse in the reverse direction (Fig. 5.2f). When the separation distance between the two plates gets much larger than the FEP film thickness, all the positive charges will return back to the bottom electrode and the TENG will reach the state shown in Figure 5.2c. Such a mechanical energy harvesting cycle can keep taking place as long as the triggering from the mechanical motion continues. In each deformation process (either pressing or releasing), the amount of charge transferred across the load equals to the amount of the negative charges on the FEP layer.

5.3 The Study of the Maximum Surface Charge Density for the TENG

5.3.1 The In-Situ Measurement of the Ion-Injection Process and the Enhancement of the TENG's output

Through using the ion injection method to introduce static charges on the dielectric surface, the charge density can be manually controlled. Moreover, this charge generation process is independent of the electricity generation process. Thus, this method makes it possible to systematically study the maximum surface charge density for TENGs. In the charge injection process as shown in Figure 5.2a, because the amount of the negative charges injected onto the FEP surface equals to the amount of electrons flowing from the bottom electrode to the ground, this charge injection process can be monitored by using a coulomb meter to measure the instantaneous charge flow from the ground to the bottom electrode (inset of Fig. 5.3a). As shown in Figure 5.3a, each time of ion injection will cause a transfer of charge with an area density of ~40 $\mu C/m^2$ from the ground to the bottom electrode, implying the same density of charges introduced onto the FEP surface. When we kept injecting the negative ions for multiple cycles, the charges transferred from the ground to the bottom electrode accumulated step by step, reflecting the accumulation of the negative charges on the FEP surface. We conducted the ion-injection process for 17 times, during which there is no charge saturation observed. Finally, the density of the positive charges on the electrode reaches ~630 $\mu C/m^2$, which stands for density of the negative static charges obtained by the FEP surface. This is over ten times higher than the maximum surface charge density (53.1 $\mu C/m^2$) that could be obtained by an electrode-free dielectric film.

Such a step-by-step ion injection for the enhancement of surface charge density has also been studied in a TENG structure. After the FEP surface has been injected with the negative ions by one further time, the FEP/electrode double layer is assembled with an Al plate into a vertical contact-separation mode TENG. Then the short-circuit charge

density ($\Delta\sigma_{SC}$) from the TENG is measured, which equals to the surface charge density on the FEP layer. In this set of experiments, the thickness of the utilized FEP film is 50 μm. We first tested the output of the TENG before the FEP film was injected with negative ions, in which the static surface charges were generated by triboelectrification with Al. As shown in Figure 5.3b, in this initial group, the TENG only produced a $\Delta\sigma_{SC}$ of ~50 μC/m^2, which stands for the triboelectric surface charge density on the FEP surface. Then, we utilized the air-ionization gun to inject negative ions onto the FEP surface. As shown in Figure 5.3b, the $\Delta\sigma_{SC}$ from the TENG gradually increased step by step after the negative ions were injected onto the FEP surface time by time. This directly reflects the enhancement of surface charge density by the ion injection. After the first few times of injection, the $\Delta\sigma_{SC}$ approached the level around 250 μC/m^2. Then every time of injection will only lead to a small increase on $\Delta\sigma_{SC}$. After the 9th time of injection, there appeared a distinctive difference in the charge transfer behavior, as marked by the red square box in Figure 5.3b. After the additional cycle of ion-injection, the first pressing motion led to a charge transfer with the density of ~260 μC/m^2. Subsequently, when the Al layer was released by to get separated from the FEP layer, the reverse charge transfer only has an amount of ~230 μC/m^2, so that the $\Delta\sigma_{SC}$ curve cannot return to the base line after the first full deformation cycle. In the following cycles, the $\Delta\sigma_{SC}$ stayed at the level of 230 μC/m^2. Since the amount of charge flow in each deformation process should equal to that of the surface charges on FEP, this abrupt decrease of $\Delta\sigma_{SC}$ in the first deformation cycle after the 9th ion injection should come from the loss of the static surface charges as a result of air breakdown during the first releasing process. This should come from the voltage drop across the air gap between the Al layer and the FEP surface, when these two surfaces starts to get separated (Fig. 5.3c). The existence of this voltage drop can be verified by the numerical simulation of the potential distribution in this TENG system. As shown in the bottom image in Figure 5.3c, when the vertical-to-plane distance between the Al and the FEP is half the thickness of the FEP (set as 50 μm in the simulation model), a voltage

drop of ~300 V exists in the air gap at the short-circuit condition. This voltage drop (V_{gap}) should be proportional to the surface charge density on the FEP. So if the surface charge density leads to a V_{gap} higher than the threshold voltage for the air breakdown at a certain gap distance, the air in the gap will get discharged so that the positive ions from the corona will partially screen the negative surface charges on the FEP. This will result in the loss of the surface charges in the first cycle of deformation after the ion injection, as shown in the last set of TENG operation in Figure 5.3b.

5.3.2 The Experimental Study of the Maximum Surface Charge Density

With the help of this ion injection method, this unique charge transfer behavior in the last set of operation shown in Figure 5.3b can serve as an indication of the air breakdown during the operation of the TENG, which provides an effective way to study the maximum surface charge density for a TENG structure. In such an operation group of TENG, the density of the initial short-circuit charge transfer ($\Delta\sigma_{SC\text{-}I}$) from the first pressing deformation is evidently larger than the density of charge transfer ($\Delta\sigma_{SC\text{-}R}$) in the remaining deformation cycles thereafter, as shown in such a magnified charge transfer curve in the inset of Figure 3d. Through changing the times of ion injection, we introduced widely-varied surface charge densities onto the FEP layer. After each set of ion injections, the FEP film was assembled into the TENG to test the charge transfer behavior. From each group of charge transfer curve, the $\Delta\sigma_{SC\text{-}I}$ and $\Delta\sigma_{SC\text{-}R}$ can be obtained, which were then plotted in the same figure, with the $\Delta\sigma_{SC\text{-}I}$ value as the horizontal axis and the $\Delta\sigma_{SC\text{-}R}$ as the vertical axis. As shown in Figure 5.3d, in the Region I where $\Delta\sigma_{SC\text{-}I}$ is within the relatively small range, the plotted points are almost on the line of $\Delta\sigma_{SC\text{-}I} = \Delta\sigma_{SC\text{-}R}$. This is the normal charge transfer behavior we observed from the TENG in which there is no air breakdown happening. Then, when the $\Delta\sigma_{SC\text{-}I}$ is further increased to the range over 200 μC/m^2, the points deviate downward from the line of $\Delta\sigma_{SC\text{-}I} = \Delta\sigma_{SC\text{-}R}$. This means that the surface charge density on the FEP starts to cause the air breakdown and

thus approaches the maximum charge density, from which $\Delta\sigma_{SC\text{-}I}$ get into Region II. In this region, the $\Delta\sigma_{SC\text{-}R}$ of all the points are smaller than the $\Delta\sigma_{SC\text{-}I}$. And a higher $\Delta\sigma_{SC\text{-}I}$ leads to a smaller $\Delta\sigma_{SC\text{-}R}$. The possible reason is that when the surface charge density on the FEP exceeds the maximum charge density by a larger extend, the air breakdown caused during the first operation cycle of the TENG will be more intensive, which could probably cause a stronger screening to the negative surface charges on the FEP. From this plot, the maximum surface charge density can be easily obtained either as the border between the Region I and Region II, or as the highest achievable value of the $\Delta\sigma_{SC\text{-}R}$. From this plot, the maximum charge density (σ_{max}) for this TENG structure with the FEP thickness of 50 μm is ~240 μC/m^2.

5.3.3 The Theoretical Study of the Maximum Surface Charge Density

The maximum charge density for the contact-mode TENG can also be obtained from the theoretical analysis through comparing the threshold voltage for the air breakdown between a gap and the actual voltage drop across the gap in the contact-mode TENG. We firstly derive the equilibrium charge density (σ_x) on the bottom electrode at a gap distance of x. The potential difference between the two electrodes is:

$$\Delta V_E = \frac{(\sigma_0-\sigma_x)}{2\varepsilon_0}\left(x+\frac{d}{\varepsilon_r}\right) - \frac{\sigma_0}{2\varepsilon_0}\left(-x+\frac{d}{\varepsilon_r}\right) + \frac{\sigma_x}{2\varepsilon_0}\left(-x-\frac{d}{\varepsilon_r}\right) \quad (5.1)$$

where d is the thickness of the FEP film, σ_0 is the surface charge density on the FEP film, and $\varepsilon_r$is the relative permittivity of the FEP layer. When the two electrodes are in short-circuit condition, we have:

$$\Delta V_E = 0 \quad (5.2)$$

From this, we can get:

$$\sigma_x = \frac{x\varepsilon_r}{d+x\varepsilon_r}\sigma_0 \quad (5.3)$$

Thus, the potential difference across the air gap between the triboelectric surfaces:

$$V_{gap} = \frac{(\sigma_0-\sigma_x)}{2\varepsilon_0}x + \frac{\sigma_0}{2\varepsilon_0}x - \frac{\sigma_x}{2\varepsilon_0}x = \frac{(\sigma_0-\sigma_x)}{\varepsilon_0}x = \frac{d\sigma_0 x}{\varepsilon_0(d+x\varepsilon_r)} \quad (5.4)$$

For the breakdown voltage of a gas between two plates at a small gap distance, it follows the Paschen curve—an empirical law showing the relationship of the breakdown voltage and the gap distance between the two plates[100,101]:

$$V_{a-b} = \frac{A(Px)}{\ln(Px)+B} \tag{5.5}$$

in which P is the pressure of the gas, A and B are the constants that determined by the composition and the pressure of the gas. For air at standard atmospheric pressure of 101 kPa as the surrounding condition of a TENG, $A = 2.87\times10^5$ V/(atm·m), and $B = 12.6$.[101]

Thus, during the releasing half cycle of the TENG, when x starts to increase from 0, the V_{gap} needs to be kept smaller than $V_{a\text{-}b}$ at any $x > 0$ in order to avoid breakdown of air. So the following relationship should be satisfied:

$$\frac{A(Px)}{\ln(Px)+B} - \frac{d\sigma_0 x}{\varepsilon_0(d+x\varepsilon_r)} > 0 \tag{5.6}$$

From this, we can get,

$$\sigma_0 < \left(\frac{AP\varepsilon_0(d+x\varepsilon_r)}{d(\ln(Px)+B)}\right)_{min} \tag{5.7}$$

Thus, the maximum surface charge density (σ_{max}) for a TENG with the dielectric thickness of d is:

$$\sigma_{max} = \left(\frac{AP\varepsilon_0(d+x\varepsilon_r)}{d(\ln(Px)+B)}\right)_{min} \tag{5.8}$$

From this equation, when d = 50 μm for the FEP layer used in this experimentally studied case, the theoretical σ_{max} is 241.05 μC/m^2, which matches very well with the experimentally obtained value of ~240 μC/m^2.

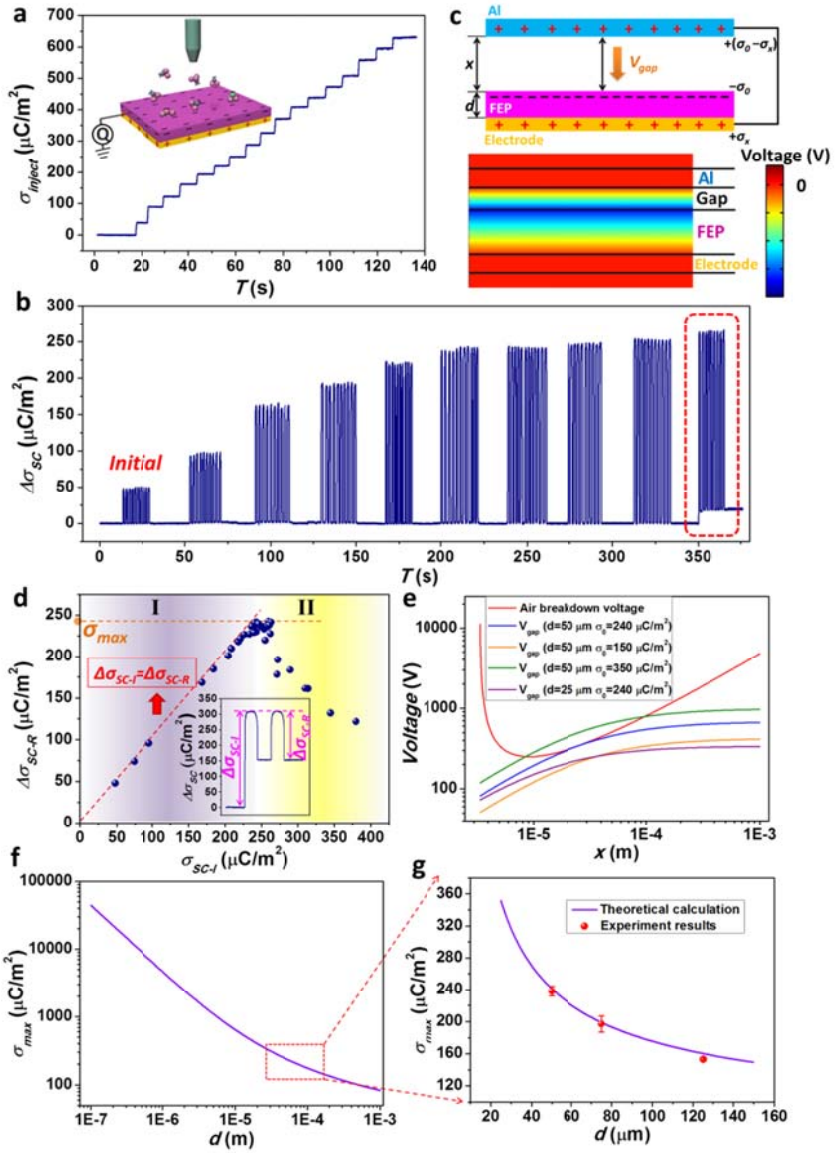

Figure 5.3 Step-by-step measurement of the ion-injection process and the study of the maximum surface charge density for the TENG. (a) The in-situ measurement of the charge flowing from the ground to the bottom electrode of the FEP film during the step-by-step ion injection process. (b) The increase of the short-circuit charge density ($\Delta\sigma_{SC}$) from the TENG when the FEP film was injected with ions time-by-time. (c) The schematic and the numerical simulation results showing the voltage drop (V_{gap}) in the air gap between the Al and the FEP layers, which could cause the breakdown of the air. (d) The plot showing the relationship between the initial short-circuit charge density ($\Delta\sigma_{SC\text{-}I}$) from the first pressing motion of the TENG right after the ion-injection

process on the FEP film, and the short-circuit charge density ($\Delta\sigma_{SC\text{-}R}$) in the remaining cycles. The inset is the magnified curve for the short-circuit charge density when the air-breakdown happens in the first deformation cycle so that $\Delta\sigma_{SC\text{-}R}$ is smaller than $\Delta\sigma_{SC\text{-}I}$. (e) The plot of the air-breakdown voltage and the voltage drop (V_{gap}) across the gap in the TENG system, with the relationship to the gap distance (x). (f) The theoretical relationship between the maximum surface charge density (σ_{max}) and the thickness (d) of the FEP film. (g) The plot of the above theoretical relationship in the range of 20-150 μm, with the three points of the experimentally obtained σ_{max} for the d of 50, 75 and 125 μm, respectively.

This theoretical analysis of the maximum surface charge density can also be achieved by the plotting the threshold voltage curve for the air breakdown and the V_{gap} in the TENG with different σ_0 and d in the same figure, as shown in Figure 5.3e. The curve of the air breakdown voltage has a very unique shape in that the voltage will have a minimum value at certain gap distance of x. As for the curves for the V_{gap} in the TENG system with specific d and σ_0, if the curve is below air breakdown voltage curve at any x value, without any intersections, the V_{gap} will not cause the breakdown of the air in the gap. When the σ_0 is increased with the d kept at the same value of 50 μm, the curve of the V_{gap} will proportionally go up, as shown by the orange, the blue and the green curves for the σ_0 of 150 μC/m^2, 240 μC/m^2 and 350 μC/m^2 respectively. Among them, the blue curve has the tangential contact with the air breakdown voltage curve, reflecting that the corresponding σ_0 of 240 μC/m^2 is the maximum surface charge density for this TENG. But if we keep the σ_0 in the same value of 240 μC/m^2, but decrease the d to only 25 μm, the plotted purple curve will move downward compared to the blue curve, making it located below the air breakdown curve. Thus, the σ_0 of 240 μC/m^2 is smaller than the σ_{max} for this film thickness. This clearly tells that a smaller film thickness will lead to a larger maximum surface charge density for the contact-mode TENG.

Such a relationship between the σ_{max} and the d can be also directly obtained by numerically plotting the curve of σ_{max}-d according to Eq. (5.8). As shown in Figure 5.3f, when the film thickness decreases from the range of tens of microns to the range of hundreds of nanometers, the σ_{max} will increase by two orders to over 10 mC/m^2. Such a theoretical relationship between the σ_{max} and the d can be verified by experiments. We carried out the similar sets of experiments on the FEP films with the thicknesses of 75 μm and 150 μm, respectively, to determine the corresponding σ_{max} for them. Then we plotted the three points representing the σ_{max} for these three thicknesses in Figure 5.3g, and together with the theoretical σ_{max}-d curve in the range of 20-150 μm. From this plot, we can find that these three experimental points coincide with the theoretical curve very well. So this relationship of maximum surface charge density was illustrated both theoretically and experimentally. Such a relationship clearly tells that a smaller thickness of the dielectric film is favorable for building a high-output TENG by improving the surface charge density.

5.4 Enhancement of TENGs' Power Output by the Ion-Injection Method

5.4.1 The Enhancement of the TENG's Power Output

This ion injection method for the introduction of the surface charges can largely enhance the power output of the TENG for mechanical energy harvesting, through effectively increasing the surface charge density on the FEP. From the measured $\Delta\sigma_{SC}$ of the TENG with the FEP film before and after the ion injections as shown in Figure 5.3b, the ion injection can lead to a five-fold enhancement of the surface charge density (also the $\Delta\sigma_{SC}$) compared to that generated by the triboelectrification process. This increase of surface charge density should lead to a proportional increase of both the V_{OC} and the J_{SC}. As shown in Figure 5.4a, before the ion injection, the TENG can only produce a V_{OC} of ~ 200 V. After the ion injection that increased the charge density to the maximum value

(240 μC/m^2) for this film thickness, the V_{OC} from the TENG increased to ~1000 V. As for the current signals before and after the ion injection both generated by gentle hand pressing (with an approximate pressing force of 20 N), the J_{SC} increased from ~18 mA/m^2 to ~78 mA/m^2 (Figs. 5.4c&d). If the ion-injection-enhanced TENG was triggered by a much higher pressing force that leads to a much faster deformation process, the generated J_{SC} will have a very large magnitude. As shown in Figure 5.4e, under the pressing force of ~300 N, the TENG generated a J_{SC} as high as 900 mA/m^2. Under this deformation condition, this actual power output from this ion-injection-enhanced TENG was tested by connecting the TENG to a series of loads with different resistances. As shown in Figure 5.4f, the current density through the load will gradually decrease with the increase of the resistance, while the voltage follows a reverse trend. The power output density of this TENG reached the maximum value of ~315 W/m^2 at the resistance of 300 MΩ. Therefore, the ion-injection is a very effective method for the improvement of TENGs' power output. Considering that the maximum surface charge density becomes larger when the film thickness gets smaller, the power output of the TENG can possibly be enhanced to a much higher level by the ion-injection method if a thinner FEP film is used.

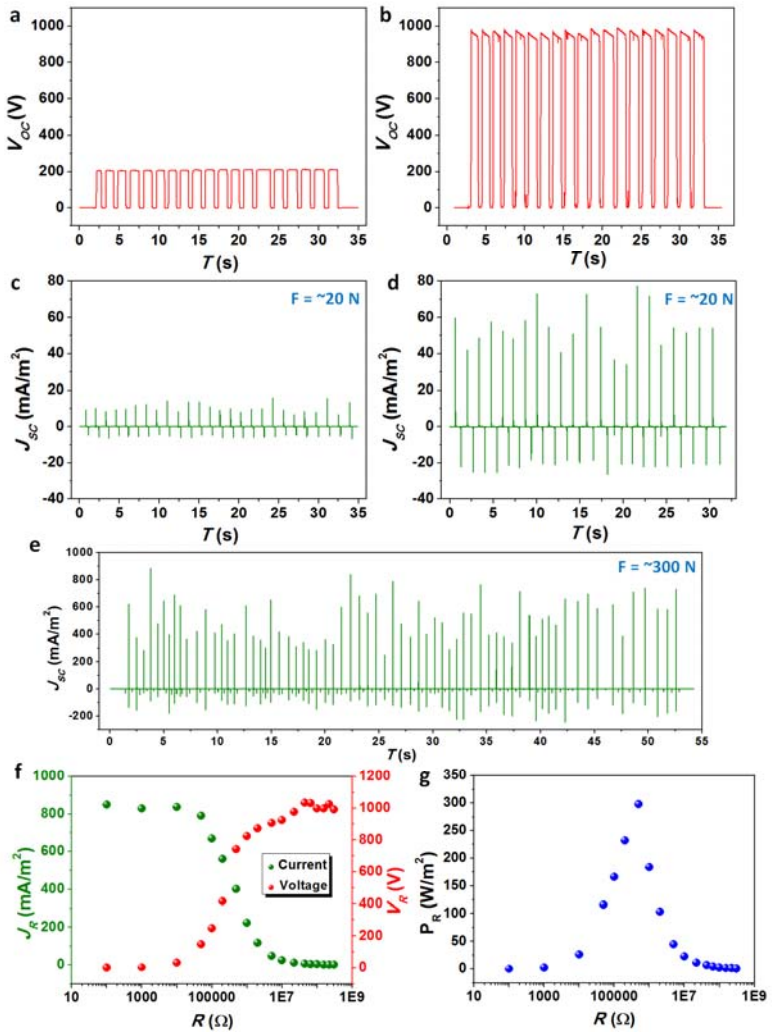

Figure 5.4 The enhancement of the TENG's output performance by the ion injection method. (a-b) The open-circuit voltage (a) of the TENG before any ion injection process, in which is the surface charges are only generated by triboelectrification with Al, (b) of the TENG after the ion-injection process, making the surface charge density on the FEP reach the maximum value. (c-d) The short-circuit current density of the TENG under the gentle pressing of hand with the force of ~20 N: (c) before any ion injection process; (d) after the ion-injection process, making the surface charge density on the FEP reach the maximum value. (e) The short-circuit current density of the TENG after the ion injection, under the deformation force of ~300 N. (f) When the above TENG after the ion-injection was connected to the loads with different resistances, the current density and the voltage on the loads. (g) The power density obtained by the loads with difference resistances.

5.4.2 The Stability of the Enhanced Output by the Ion-Injection

When the TENG is constructed by an electret film, which is the experimental demonstration in this work, the negative surface charges brought by the ion-injection method can preserve for a very long, so that the TENG can deliver a high output in a long-term after its dielectric surface gets pre-charged. The FEP we used in this study is a very good electret, the negative surface charges on the FEP film from the ion injection should be able to preserve for a long time. In order to study the stability of the surface charge on the FEP, we regularly measured the $\Delta\sigma_{SC}$ from the TENG constructed using this FEP film in a time range of 160 days. From the results in Figure 5.5a, the $\Delta\sigma_{SC}$ only decayed from the initial 240 $\mu C/m^2$ that was measured right after the ion injection, to ~200 $\mu C/m^2$ after 160 days, and almost got stabilized at this value. Thus, there is only ~16.6% loss of the surface charges, and the remained $\Delta\sigma_{SC}$ after 160 days is still 4 times as high as the $\Delta\sigma_{SC}$ generated by the TENG without the ion injection process. The stability of the TENG performance was also investigated under a continuous operation case. As shown in Figure 5.5b, when the TENG was continuously deformed by the external pressing force, the generated $\Delta\sigma_{SC}$ only has a little decay in the continuous operation of ~400,000 cycles. Both of the above two groups of measurements clearly show that the ion injection method is an effective and practical method for building the TENG that can deliver a largely-enhanced output for a sufficiently long time.

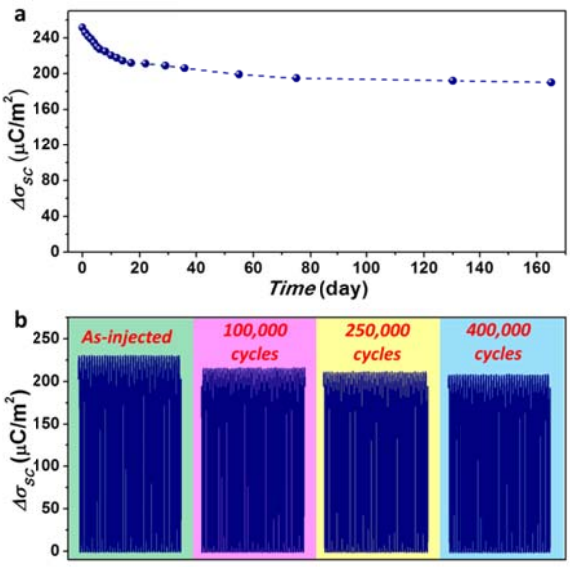

Figure 5.5 Stability of the electret-based TENG with the dielectric surface injected with ions. (a) The stability of the surface charge on the FEP layer from the ion injection process, tested through measuring the $\Delta\sigma_{SC}$ from the TENG. (b) The stability of the TENG when it was continuously operating for ~400,000 cycles.

This study not only provides an effective method for the enhancement of the TENG's output for mechanical energy harvesting, but also for the first time observed the existence of the maximum surface charge density for the TENG. The relationship between the maximum surface charge density and the thickness of the dielectric film clearly reveals an important guideline for the structural design when trying to enhance the surface charge density through material or surface modification. Under a small film thickness, the maximum surface charge density largely increases, creating a much bigger room for the improvement of the triboelectric charge density. Therefore, this study clearly tells us that through optimization of the materials' property, the power output of the TENG can be largely enhanced by as high as 4 orders!

CHAPTER 6

SELF-CHARING POWER CELL BASED ON THE HYBRIDIZATION OF PIEZOELECTRIC NANOGENERATOR AND LI-ION BATTERY

Energy conversion and storage[8,16,60] are two most important technologies in today's green and renewable energy science, which are usually separated units designed based on vastly different approaches. As for energy harvesting, depending on the nature of energy sources, such as solar,[10-15] thermal,[16-18] chemical,[20-22] and mechanical, various mechanisms have been developed for effectively converting them into electricity. Take smaller scale mechanical energy as an example, piezoelectric nanogenerators (NGs) have been developed into a powerful approach for converting low-frequency, biomechanical energy into electricity. The mechanism of the NG relies on the piezoelectric potential created by an externally applied strain in the piezoelectric material for driving the flow of electrons in the external load.[23,35] As for energy storage, Li-ion battery is one of the most effective approaches,[24,62-65] in which the electric energy is stored as chemical energy through the migration of Li ions under the driving of an externally applied voltage source and the follow up electrochemical reactions occurring at the anode and cathode.[102]

In general, electricity generation and energy storage are two distinct processes that are accomplished through two different and separated physical units achieving the conversions of from mechanical energy to electricity and then from electric energy to chemical energy, respectively. In this dissertation, we introduced a fundamental mechanism that directly hybridizes the two processes into one, through which the mechanical energy is directly converted and simultaneously stored as chemical energy, so that the nanogenerator and the battery are hybridized as a single unit.[103] Such an integrated self-charging power cell (SCPC), which can be charged up by mechanical deformation and vibration from the environment, provides an innovative approach for

developing new mobile power source for both self-powered systems[34] and portable and personal electronics.

6.1 Structural Design and Fabrication of the Self-Charging Power Cell (SCPC)

The experimental design of a self-charging process is based on the characteristics of both piezoelectric and electrochemical properties, as schematically shown in Figure 6.1a. The device is based on a sealed stainless-steel 2016-coin-type cell, as shown in the highlight of Figure 6.1b. The SCPC is composed of three major components: anode, separator and cathode. The anode is aligned TiO_2 nanotube (NT) arrays that are directly grown on a Ti foil.[104] Instead of using the polyethylene (PE) separator[105] as for traditional lithium ion battery, a layer of polarized poly(vinylidene fluoride) (PVDF) film (Measurement Specialties, Inc., U. S. A.) is located above the TiO_2 nanotube arrays as the separator. This PVDF film can establish a piezoelectric potential across its thickness under externally applied stress, which not only converts mechanical energy into electricity, but also serves as the driving force for the migration of Li ions. The cathodes are $LiCoO_2$/conductive carbon/binder mixtures on aluminum foils. Figure 6.1c is a cross-sectional SEM image of the sandwich structure of the device. The TiO_2 nanotube arrays with anatase crystal structure (Fig. 6.2a) were fabricated on Ti substrate using an anodization method with a post-annealing process in air.[106] The detailed growth process of the TiO_2 nanotube array is described below. As shown in Figure 6.1d, the height and diameter of the nanotubes are about 20 μm and 100 nm, respectively. A commercial piezoelectric PVDF film with a thickness of ~110 μm is predominantly composed of β phase, which generates the strong piezoelectric effect, and with a small fraction of α phase (Fig. 6.2b).[107] The PVDF film has been prior poled before assembly into the battery. After placing $LiCoO_2$ cathode with a thickness of 20 μm on the other side, the system was filled with electrolyte (1M $LiPF_6$ in 1:1 ethylene carbonate: dimethyl carbonate) and finally sealed for measurements. Periodic deformations were applied onto

the device in order to charge it up (Fig. 6.1b), and the voltage and current were monitored simultaneously in both charging and discharging processes.

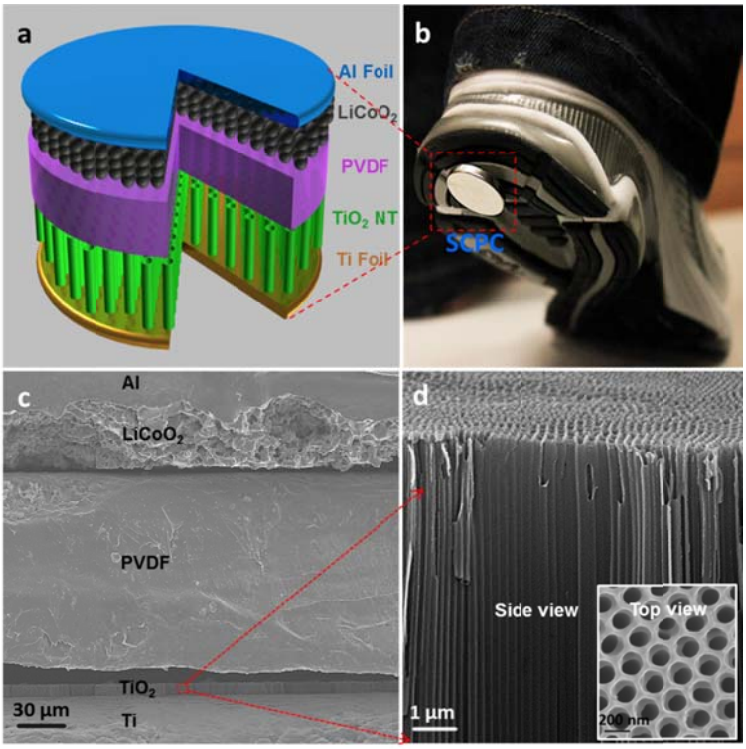

Figure 6.1 Structure design of a self-charging power cell by hybridizing a piezoelectric nanogenerator and a Li-ion battery. (a) Schematic diagram showing the design and structure of the self-charging power cell. The anode is aligned TiO_2 nanotube arrays that are directly grown on Ti foils; a layer of polarized PVDF film performs as the separator; the cathode is $LiCoO_2$ mixture on aluminum foil. This structure is sealed in stainless-steel 2016-coin-type cells, as shown in the inset. (b) Sticking a power cell on the bottom of a shoe, the compressive energy generated by walking can be converted and stored directly by SCPC. (c) Cross-sectional SEM image of the self-charging power cell, which is composed of aligned nanotubes as anode, piezoelectric polymer film as separator and cathode. (d) Enlarged view of the aligned TiO_2 nanotubes. The inset is a top view SEM image of the nanotubes.

TiO_2 nanotube arrays were directly grown on Ti foils (0.05mm thick, 99.6% purity; Alfa Aesar) by electrochemical anodizing in ethylene glycol solution containing 0.3 wt % NH_4F and 2 vol % H_2O, with Pt as counter electrode. Prior to growth, all Ti

foils were ultrasonically cleaned in acetone, water, and ethanol consecutively, and then dried in air. A thin layer of PMMA was spin-coated on one side of the foil to protect it from the etching solution. The prepared Ti foil was anodized at 50 V for 5 hours, and then treated by ultrasonication in acetone for a few seconds, leaving hexagon-like footprints on the surface of Ti foil. A second anodization was then performed under the same condition for 2 h to produce well-aligned TiO_2. Finally, the two-step anodized nanotubes were annealed at 450 ℃ for 2 hours in the air to form anatase crystalline phase and remove PMMA on the back of Ti foils.[106]

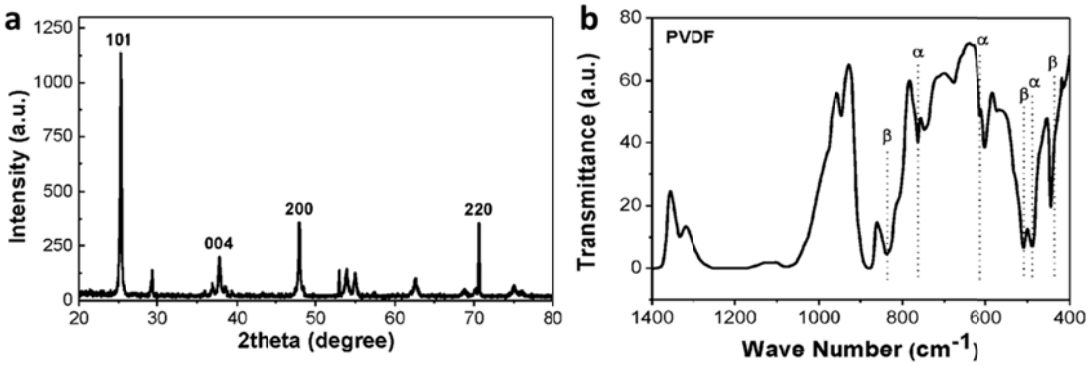

Figure 6.2 Structural Characterization of the TiO_2 nanotubes and the PVDF film. (a) XRD pattern of as-synthesized TiO_2 nanotubes to define their phase. All of the main peaks can be indexed to anatase TiO_2 crystal (JCPDS File No. 21-1272). (b) FTIR spectrum of PVDF separator film.

6.2 Mechanical-to-Electrochemical Process as Working Mechanism for the SCPC

Based on the nature of piezoelectricity and electrochemistry-based energy storage process, we proposed the working mechanism of the SCPC as an electrochemical process driven by deformation created piezoelectric potential (Fig. 6.3).[103] At the very beginning, the device is at a discharged state, with $LiCoO_2$ as the positive electrode (cathode) material and TiO_2 NTs as the negative electrode (anode), which is the originally fabricated structure of the device, and the $LiPF_6$ electrolyte is evenly distributed across the entire space, as shown in Figure 6.3a. A PVDF film, which has intimate contacts with

both electrodes, serves as the separator and it has the smallest Young's modules among all of the components in the device, thus, it suffers from the most severe compressive strain when a compressive stress is applied onto the device, as shown in Figure 6.3b. We purposely use the PVDF film with the polarity that results in a positive piezoelectric potential (piezopotential) at the cathode ($LiCoO_2$) side and negative piezopotential at the anode (TiO_2) under compressive strain for separating the charges. Under the driving of the piezoelectric field with a direction from the cathode to the anode, the Li ions in the electrolyte will migrate along the direction through the ionic conduction paths present in the PVDF film separator for ion conduction[108,109] in order to screen the piezoelectric field, and finally reach the anode, as shown in Figure 6.3c. The decreased concentration of Li^+ at the cathode will break the chemical equilibrium of the cathode electrode reaction ($LiCoO_2 \leftrightarrow Li_{1-x}CoO_2 + xLi^+ + xe^-$),[110] so that Li^+ will deintercalate from $LiCoO_2$, turning it into $Li_{1-x}CoO_2$ and leaving free electrons at the current collector (Al foil) of the cathode electrode. This process is driven by the tendency of establishing new chemical equilibrium. In the meanwhile, under the elevated concentration of Li^+ at the anode, the reaction at the other electrode ($TiO_2 + xLi^+ + xe^- \leftrightarrow Li_xTiO_2$)[111] will move to the forward direction for the same reason, enabling Li^+ to react with TiO_2 so that Li_xTiO_2 will be produced at the anode electrode, leaving the positive charges at the Ti foil as the current collector. During this process, Li^+ will continuously migrate from the cathode to the anode and the device is charged up a little bit owing to the large volume of the device. During the progress of charging electrochemical reactions at the two electrodes, extra free electrons could be suggested to transfer across the two electrodes through some internal mechanisms. Under the mechanical deformation, the piezopotential continues to drive the migration of Li^+ ions until to a point when the chemical equilibriums of the two electrodes are re-established and the distribution of the Li^+ can balance the piezoelectric-field in the PVDF film, with no Li^+ drifting through PVDF, (Figure 6.3d); that is to say, a

new equilibrium is achieved and self-charging process will cease. This is the process of converting mechanical energy directly into chemical energy.

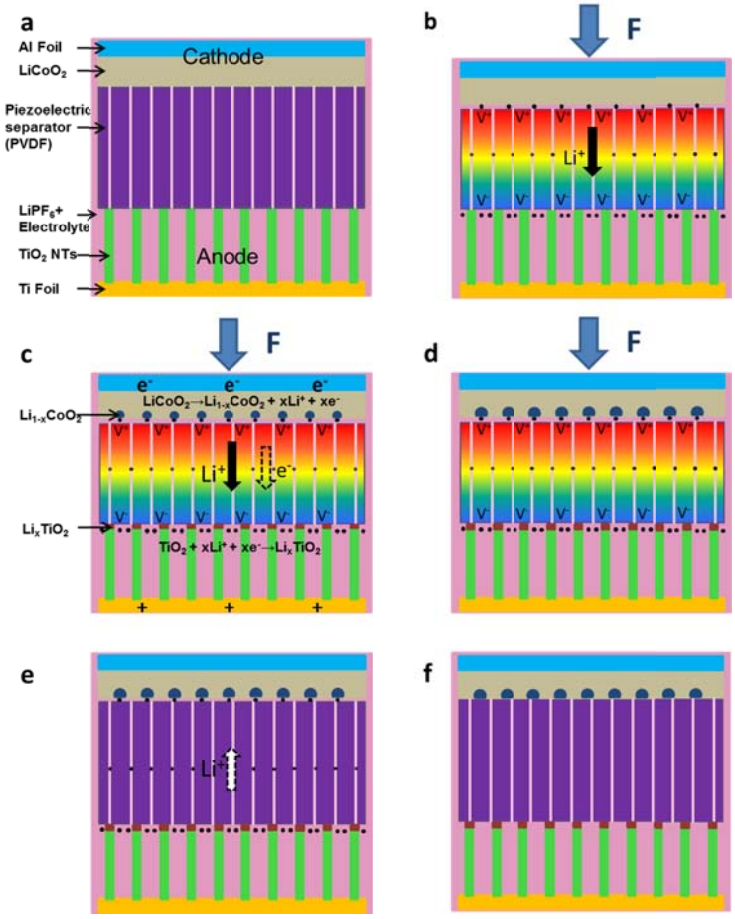

Figure 6.3 The working mechanism of the self-charging power cell driven by compressive straining. (a) Schematic illustration of the self-charging power cell in discharged state with $LiCoO_2$ as cathode and TiO_2 nanotubes as anode. (b) When a compressive stress is applied onto the device, the piezoelectric separator layer (e.g., PVDF film) creates a piezopotential, with the positive polarity at the cathode side and negative piezopotential at the anode. (c) Under the driving of the piezoelectric field, the Li ions from the cathode will migrate through the PVDF film separator in the electrolyte toward the anode, leading to the corresponding charging reactions at the two electrodes. The free electrons at the cathode and positive charges at the anode will dissipate inside the device system. (d) The status where chemical equilibrium of the two electrodes is re-established and the self-charging process ceases. (e) When the applied force is released, the piezoelectric field of the PVDF disappears, which breaks the electrostatic

equilibrium, so that a portion of the Li ions will diffuse back to the cathode. (f) This electrochemical system reaches a new equilibrium, and a cycle of self-charging is completed.

In the second step, when the applied force is released, the piezoelectric field of the PVDF disappears, which breaks the electrostatic equilibrium, so that a portion of the Li ions diffuse back from the anode to the cathode (Fig. 6.3e) and reach an even distribution of Li^+ all over the space in the device again (Fig. 6.3f). Then, a cycle of charging is completed through an electrochemical process of oxidizing a small amount of $LiCoO_2$ at cathode to $Li_{1-x}CoO_2$ and reducing a bit of TiO_2 to Li_xTiO_2 at the anode. When the device is mechanically deformed again, the process presented above is repeated, resulting in another cycle of charging by converting mechanical energy directly into chemical energy.

In this self-charging mechanism, the role played by the piezoelectric material (PVDF) is similar to the DC power supply used in the conventional charging process of a Li battery. Both of them can be deemed as charge pumps, but the specific mechanisms are different. As for the conventional charging method, the DC power supply will pump the electrons from the positive electrode to the negative electrode through the external circuit and the Li ions will go in the same direction but within the cell, in order to remain a neutral charge balance. Thus the electrochemical reactions on the two electrodes occur and the battery is charged up. But for our SCPC proposed here, the piezoelectric material pumps the Li^+ ions, rather than the electrons, from the positive to the negative electrode, which also accomplishes the charging of the device. This mechanism can also be explained by thermodynamics. According to Nernst's theory,[112] the relative electrode potentials of the two electrodes have the following relationships with Li^+ concentration:

$$\varphi_{Li_{1-x}CoO_2/LiCoO_2} = \varphi^o_{Li_{1-x}CoO_2/LiCoO_2} - \frac{RT}{F}\ln\frac{1}{[a_c(Li^+)]^x}$$

$$\varphi_{TiO_2/Li_xTiO_2} = \varphi^o_{TiO_2/Li_xTiO_2} - \frac{RT}{F}\ln\frac{1}{[a_a(Li^+)]^x}$$

where $\varphi_{Li_{1-x}CoO_2/LiCoO_2}$ and $\varphi_{TiO_2/Li_xTiO_2}$ are actual electrode potentials of cathode and anode, $\varphi^o_{Li_{1-x}CoO_2/LiCoO_2}$ and $\varphi^o_{TiO_2/Li_xTiO_2}$ are standard electrode potentials of these two electrodes, and $a_c(Li^+)$ and $a_a(Li^+)$ are the activities of Li^+ around cathode and anode, respectively, which can be approximately equated to the concentrations, R is the gas constant, T is the temperature, and F is the Faraday constant. Thus, under the driving of piezoelectric field, because of depleting of Li^+ concentration near the positive electrode, the electrode potential $\varphi_{Li_{1-x}CoO_2/LiCoO_2}$ will decrease; likewise, the elevation of Li^+ concentration will result in an increase of $\varphi_{TiO_2/Li_xTiO_2}$ at the negative electrode. For conventional Li-ion battery, the electrode potential $\varphi_{Li_{1-x}CoO_2/LiCoO_2}$ is larger than $\varphi_{TiO_2/Li_xTiO_2}$, so that the battery can discharge spontaneously through the reduction of $Li_{1-x}CoO_2$ and oxidization of Li_xTiO_2. But for the self-charging process, because the change of Li^+ concentration will possibly make $\varphi_{TiO_2/Li_xTiO_2}$ larger than $\varphi_{Li_{1-x}CoO_2/LiCoO_2}$, the device is self-charged through the reduction of TiO_2 and oxidization of $LiCoO_2$.

6.3 Experimentally Measured Self-Charging Process

By using a mechanical setup that can provide a periodic compressive stress onto the device, we demonstrated the self-charging process of the power cell. Figure 6.4a is a typical self-charging and discharging cycle. Under the compressive force applied to the SCPC at a frequency of 2.3 Hz, the voltage of the device increased from 327 to 395 mV in 240 s. After the self-charging process, the device was discharged back to its original voltage of 327 mV under a discharge current of 1 μA, which lasted for about 130 s. So we proved that the proposed power cell can be charged up under the repeated deformation by directly converting mechanical energy to chemical energy. In this experimental case, the stored electric capacity of the power cell was about 0.036 μAh.

From the theory of piezoelectricity, within elastic deformation regime, the magnitude of the piezopotential is linearly proportional to the magnitude of strain, thus also to the magnitude of the compressive force. Figure 6.4b shows that, as we solely increased the mechanical force applied to the device, the self-charging effect would be enhanced. Thus, an increased piezopotential can give an enhanced charging effect. In addition, the self-charging effect is also affected by the frequency at which the deformation is applied, as shown in Figure 6.4b. Under a constant applied force of impact, a higher frequency resulted in an increased charging voltage simply due to higher input power. When the force and the frequency were both kept as constant, the rate at which the voltage was increased was relatively stable. The above results are additional proofs that the self-charging process is due to the piezoelectric effect. We have demonstrated that a series connection of several SCPCs drove the operation of a commercial calculator for more than ten minutes, as shown in the inset of Figure 6.4b.

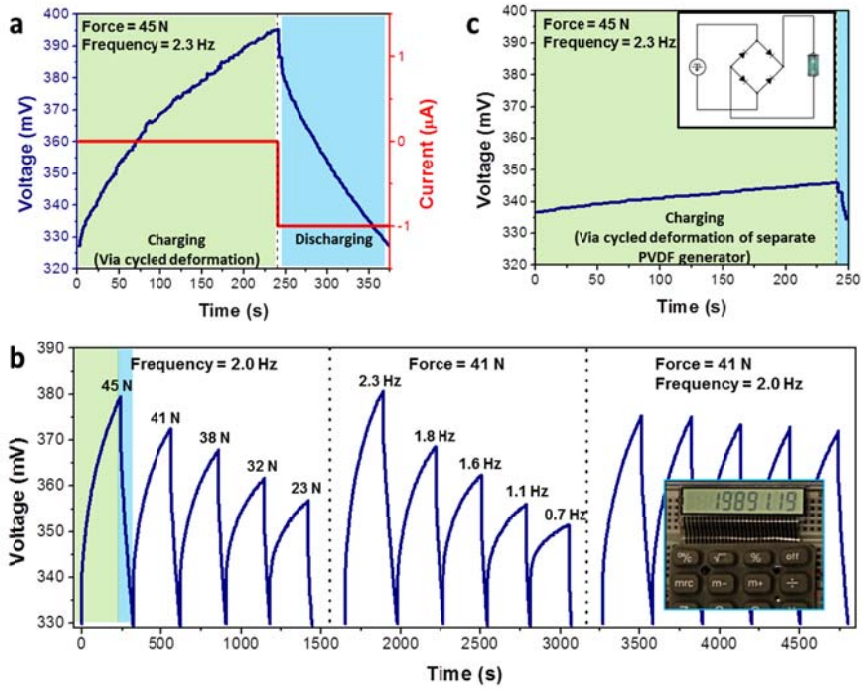

Figure 6.4 Self-charging process of SCPC under periodic compressive straining and the corresponding discharging process. (a) A typical self-charging process simply by applying cycled

mechanical compressive strain to the device (green shadowed region). In the discharge process (blue shadowed region), the stored power is released in the form of electron flow in the external load as indicated by the measured current and drop of voltage. (b) Self-charging and discharge cycles of SCPC under different force and frequencies, respectively. Inset shows the operation of a commercial calculator using the SCPCs as the power source. (c) As a comparison of efficiency, the SCPC is separated into two individual units: a PVDF piezoelectric generator and a Li-ion battery by using PE as a separator. The inset is a schematic circuit of the traditional charging methods with separated generator and storage units connected by a bridge rectifier.

The overall efficiency of our proposed SCPC has two parts—the energy converting efficiency of piezoelectric material and the energy storage efficiency of this mechanical-to-electrochemical process. We compared this with the efficiency of the traditional charging method, which is composed of a separated generator and a storage unit connected though a bridge rectifier (inset of Fig. 6.4c). The generator unit was fabricated by sealing the PVDF film in the same coin cell to create a similar straining condition as SCPC. After being charged for 4 min via cycled deformation of the separate PVDF generator, the voltage of the battery has only increased by ~10 mV (Fig. 6.4c), which is a lot lower than that of SCPC (65 mV) (Fig. 6.4a). Therefore, the single mechanical to chemical process for SCPC is much more efficient than the mechanical to electric and then electrical to chemical double-processes for charging a traditional battery. This is because our current study demonstrated a new approach for directly converting mechanical energy into chemical energy without going through the generation of electricity as an intermediate state, which saves at least the energy wasted on the outer circuitry, including the rectifying component. This is the innovation of the power cell. Thus, the SCPC we proposed here could be a powerful device to simultaneously harvest and store mechanical energy, after making several improvements on piezoelectric separators, device structure, fabrication techniques and development of flexible devices. The rigid stainless steel coin cell, which consumed a large portion of mechanical energy,

is apparently not an optimal way for the packaging of SCPC. This could be solved by designing flexible devices in the future.

6.4 Control Experiments for the Validation of the Proposed Mechanism

As a comparison and control experiment, we measured the response of a conventional Li-ion battery under the same deformation condition, which had the same structure as the power cell except using PE film as the separator instead of the piezoelectric PVDF film. As shown in Figure 6.5a, the voltage remained the same at ~325 mV during the ~4000 cycles of deformation that lasted for ~0.5 hour. Thus, the conventional Li-ion battery cannot be charged up at all by applying cycled mechanical deformation. This is because there is no piezoelectric potential that drives the migration of Li ions. This comparison experiment rules out the possible contribution from the electrostatic noise or the measurement system to the charging process presented in Figure 6.4a for SCPC.

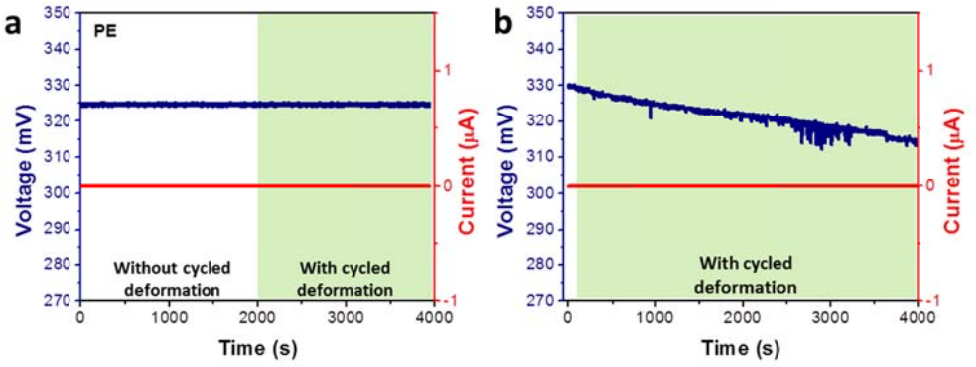

Figure 6.5 Response of devices of the similar structure as self-charging power cell, but with different films as separators. (a) For a conventional Li-ion battery using PE as the separator, no charging effect is observed by applying cycled mechanical deformation, indicating the result presented in Fig. 6.4a is due to the piezoelectric driven charging process. (b) For a device that has the same structure as a SCPC but with the PVDF film having a piezoelectric field pointing from anode to cathode, no charging effect either, just as expected from the mechanism presented in Fig. 6.3.

Alternatively, if the piezoelectric polarization as presented in Figure 6.3 is reversed, the piezoelectric field in the PVDF film is pointing from anode to cathode, which will drive the migration of Li ions in the opposite direction. As a result, the reverse electrochemical process will take place under the similar mechanism, so that the entire device will be slightly discharged after many cycles of mechanical deformation. The response of the device fabricated using PVDF film with opposite polarization was measured under the same deformation condition, as shown in Figure 6.5b. The voltage slightly decreased from 330 to 315 mV during the ~8000 cycles of deformation that lasted for ~1.1 hour. Rather than self-charging, the self-discharging has been accelerated in such a device simply because the piezopotential drove Li ions to migrate in the opposite direction of the charging process. This further confirmed the working principle of the SCPC, as proposed in Figure 6.3, can continuously drive the progress of electrochemical reactions for the energy storage.

Thus, based on the as-proposed mechanical-to-electrochemical process, the self-charging power cell can simultaneously harvest and store mechanical energy at a higher efficiency. This new concept of device could become a new energy technology for driving personal electronics and self-powered systems.

CHAPTER 7

FLEXIBLE SUSTAINABLE-POWER-UNIT BASED ON THE HYBRIDIZATION OF TRIBOELECTRIC NANOGENERATOR AND LI-ION BATTERY

Energy generation and storage are the two most important areas for developing new power sources, and they are usually two separated units based on two consecutive processes, which have limitations as sustainable power sources. Targeting at the self-powered systems that have a high mobility, excellent working-condition adaptability and stability, energy generators that function by harvesting energy from the working/living environmental usually have uncontrollable fluctuation/instability in their outputs that are greatly influenced by the change in ambient environment. Take the mechanical energy harvesting as an example, although the recently-invented triboelectric nanogenerator (TENG) is proven to be a powerful and promising technology that is highly-efficient, low-cost and environmentally-friendly,[42-44,75,77,78,91] the electricity generated are non-continuous pulses with irregular magnitude, thus, it cannot be directly used to drive most electronic devices that need a constant DC voltage supply. Energy storage devices such as batteries,[24,62-65] on the other hand, can provide a constant voltage at their discharging plateau to act as the direct power sources for most portable and wireless electronic devices. But the intrinsic problem of batteries is the limited lifetime, so that they have to be charged or replaced periodically, otherwise batteries can be "deadly drained".

In order to develop sustainable power sources by complimentarily combining the advantages of these two technologies as presented above, we demonstrated the first flexible self-charging power unit (SCPU) that is capable of simultaneously harvesting and storing ambient mechanical energy, by integrating a TENG-based mechanical energy harvester and a Li-ion battery (LIB) based energy storage. In this SCPU, the Li-ion battery portion can be directly charged by mechanical motions. With this SCPU, we

demonstrated a new working mode for a power source—the "sustainable mode", in which the environmental mechanical energy is scavenged to charge the battery while the battery keeps driving an external load as a DC source.[113]

7.1 Structure Design of the Self-Charging Power Unit (SCPU)

The integration of a LIB and a TENG in the SCPU was achieved through the construction of a flexible LIB, which was made in an arch shape for creating the gap necessary for the TENG structure,[68] as illustrated in Figure 7.1a. To achieve a good flexibility on a LIB, we grew TiO_2 nanowires grown on flexible and conductive carbon cloth as the anode side for the LIB.[104,114,115]

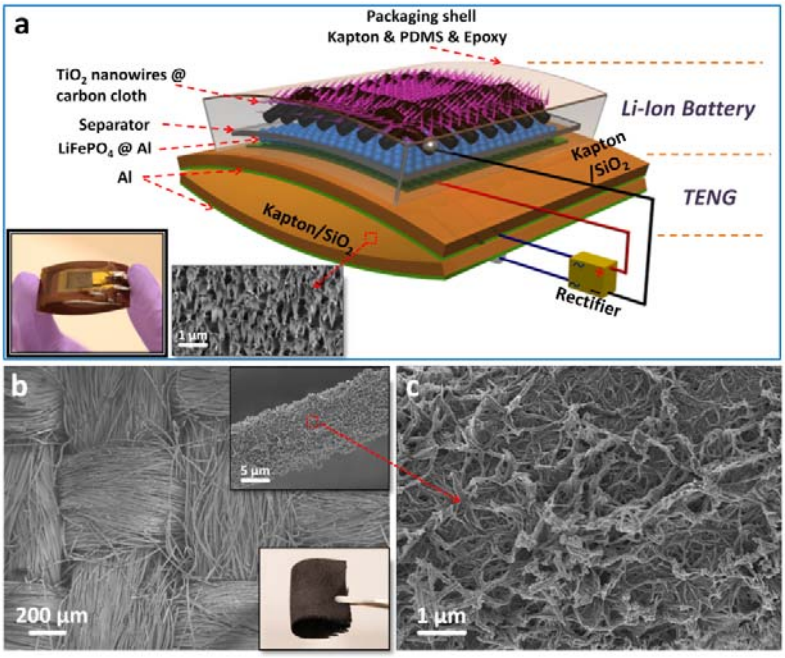

Figure 7.1 Structure design of a flexible self-charging power unit (SCPU). (a) Schematic diagram showing the detailed structure of the SCPU, the inset on the left is a photograph of a typical SCPU device, and the inset on the right is an SEM image of the Kapton nanorod-structure on the concave surface of the bottom Kapton, with 30°-tilted view. (b) SEM image of the carbon cloth grown with TiO_2 nanowire (NW) networks, the top inset is the enlarged SEM image of a single fiber in the fabric, and the bottom inset is a photograph of the TiO_2-covered carbon cloth as the

anode, showing its good flexibility. (c) SEM image with higher magnification showing the detailed morphology of the TiO_2 NW networks on the carbon cloth.

7.1.1 Growth of TiO_2 on Carbon Cloth

The carbon cloth was firstly ultrasonically cleaned in acetone, ethanol, and DI water for 30 min respectively, and then placed in a 50-mL Teflon-lined stainless steel autoclave. Next, 1 g TiO_2 (P25) powder and 40 mL NaOH (10 M) were added into the autoclave and mixed with the carbon cloth for another 30 min. After sealing, the autoclave was kept in an oven at 200 °C for 12 hours, and then cooled down in air. After this first-step hydrothermal reaction, the carbon cloth covered with Na-titanate nanowire networks were washed with water and immersed in HCl solutions (1 M, 40 mL) for 10 min to replace Na^+ with H^+, forming H-titanate nanowire networks. After that, this piece of carbon cloth was washed with water again, and then dried at ambient temperature. After heat treating the sample at 500 °C for 3 hours under Ar atmosphere, TiO_2 nanowire networks (NWN) on the carbon cloth were obtained.[114] The obtained TiO_2 NWN has anatase crystal structure, as identified by XRD (Fig. 7.2).

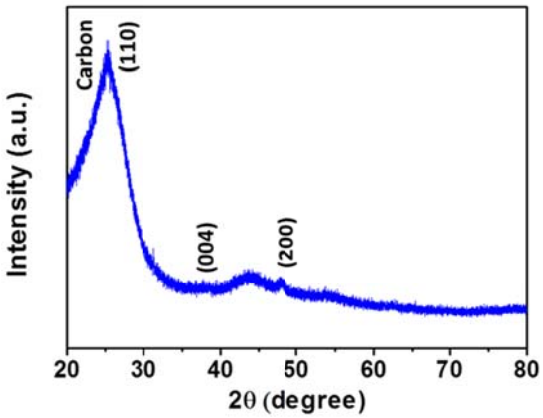

Figure 7.2 XRD pattern of the TiO_2 nanowire networks, showing that the crystal phase is anatase.

7.1.2 Device Structure and Fabrication of the SCPU

For the flexibility of the battery, we designed a polymeric shell for the packaging and sealing, to replace the conventional ridge coin cell (Fig. 7.1a). The supporting

substrate of this polymeric shell is a bent Kapton film (3 cm × 4 cm) with purposely-introduced thermal stress through the deposition of a SiO_2 film at high temperature.[68,69] The three kernel components of the LIB: the TiO_2 nanowires (NWs) anode, the PE separator and the $LiFePO_4$/active carbon/binder mixture cathode on the Al current collector, were laminated on top of the convex surface (the surface deposited with SiO_2) of this Kapton substrate. This kernel structure with an effective area of ~1.5 cm × 1.5 cm was immersed in the electrolyte. The SEM image of the TiO_2 NWs grown in carbon cloth is displayed in Figure 7.1b. From the picture of the TiO_2/carbon cloth composite shown in the inset (bottom) of Figure 7.1b, this anode layer exhibits excellent flexibility. SEM images with higher magnifications are shown at the top inset of Figure 7.1b and Figure 7.1c, from which we can tell that every single fiber in the carbon cloth is uniformly covered by TiO_2 NW networks with an average length of ~1 μm. The battery was isolated from air by covering with a layer of thin Kapton film and sealing with PDMS and epoxy at the sides. For the hybridization with the TENG, this LIB's supporting Kapton substrate was deposited with Al film on the back and bonded with another bent Kapton film of the same size in a face-to-face manner. This forms an arch-shaped TENG structure based on the triboelectrification between the top Al layer and the bottom Kapton that has the corresponding electrode (Al film) deposited on its convex surface. In order to enhance the triboelectric charge density through large surface roughness and increased effective contact area, the concave surface of the bottom Kapton was pretreated with ICP reactive ion etching, to produce the nanorod-covered surface,[81] as shown in the inset (right) of Figure 7.1a. With this hybridized SCPU structure, the LIB can be charged through harnessing ambient mechanical energy, only by rectifying the TENG-generated alternating-current (AC) pulses to DC with a full-wave bridge rectifier. A photo of a typical SCPU device is shown in the inset (left) of Figure 7.1a, clearly revealing its flexibility and arch-shaped structure.

7.2 Individual Performance of TENG Part and Li-Ion Battery Part in the SCPU

The performance of the SCPU is first characterized by the outputs of the TENG and the LIB as individual units (Fig. 7.3). When the arch-shaped structure was periodically flattened under a frequency of 8 Hz, an open-circuit voltage (V_{OC}) of ~220 V was generated between the two electrodes of the TENG part (Fig. 7.3a), which is the potential difference induced by the separation of opposite tribo-charges on the Al and Kapton films. Under a short-circuit condition, this voltage drives ~110 nC of charges (ΔQ) to flow between the two electrodes in each half deformation cycle (as shown in the measured charge transfer in Fig. 7.3b). This value should theoretically equal to the amount of tribo-charges on each triboelectric surface (with an area of ~12 cm^2), corresponding to a charge density of ~91.6 $\mu C/m^2$. This back-and-forth charge transfer produced a pair of AC short-circuit current (I_{SC}) peaks in each cycle. As shown in Figure 7.3c, the positive peak with a larger magnitude of ~150 μA came from the pressing motion, which had a higher deformation rate compared to the elastic releasing process. But these two asymmetric peaks per cycle carry the same amount of charges due to charge conservation (Fig. 7.3b). This AC output can be rectified to DC by a low-loss full wave bridge rectifier (Fig. 7.3d), which generates ~220 nC electricity per cycle to be stored in the LIB.

The capability of the flexible LIB in the SCPU for charge storage was evaluated using deep charging/discharging galvanostatic test between 0.7 and 2.7 V, at a current of 2 μA, as for conventional batteries. As indicated by the voltage profile in the 6 consecutive cycles (Fig. 6.3e), the LIB gave clear voltage plateaus in both charging and discharging processes. The discharging plateau is ~1.53 V, which is the real working voltage of the LIB as a power source. The LIB also has a stable capacity around 17.5 μAh, revealing its expected performance as an energy storage unit.

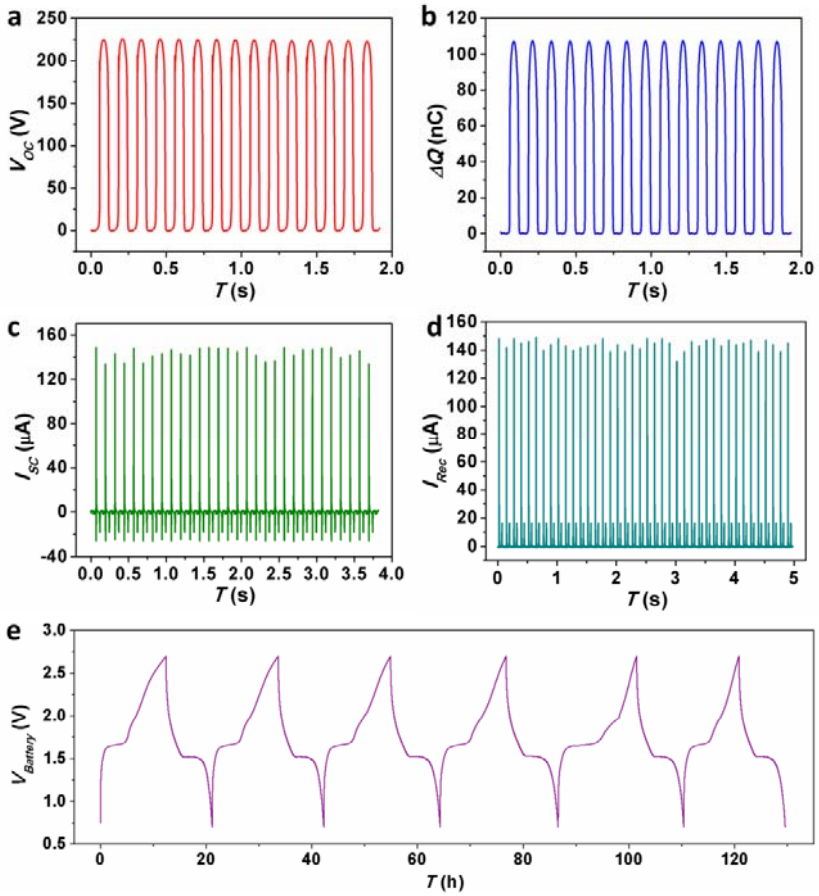

Figure 7.3 Characterizing the individual performances of the TENG part and the LIB part in the SCPU. (a) The open-circuit voltage (V_{OC}), (b) the amount of charges transferred (ΔQ), (c) the short-circuit current (I_{SC}) and (d) the rectified current (I_{Rec}) generated by the TENG part when the SCPU is periodically flattened by external mechanical agitation under the frequency of 8 Hz. (e) The voltage profile of the LIB part during the deep charging/discharging galvanostatic test with a current of 2 μA.

7.3 SCPU Working in "Standby-Active Mode"

When the TENG part and the LIB part work conjunctionally as a full unit, the SCPU will work as a self-sufficient power source. Conventionally, the charging and discharging of an energy storage unit is in two separated and consecutive steps. This working mode for the SCPU is called the "standby-active mode"[54].

7.3.1 Working Mechanism of the SCPU in "Standby-Active Mode"

When external mechanical vibration is applied onto the flexible SCPU to periodically flatten it, the two surfaces across the gap will get into contact from time to time. Coupling of the triboelectric effect with the electrostatic induction will generate a flow of current in the external circuit, which will be stored in the LIB in the same device. At the "standby-state", the LIB part is charged by the TENG part, but disconnected from the external load. We now illustrate the simultaneous charge generation and storage process of the SCPU without connecting to an external load, as shown in Figure 6.4a-e (for clarity, the arch-shaped SCPU is depicted as a flat structure and the periodic change of the gap is expressed as the change of spacing between the two parts). The electricity generation process by the TENG part is similar with that of the arch-shaped TENG described in Chapter 2. When the external pressing force is applied onto the arch-shaped device, the two surfaces (Al and Kapton) will be brought into contact from time to time. As a result, the two oppositely-tribo-charged surfaces will switch between the states of intimate contact and fully separation. The changing induced potential difference between the two electrodes creates the driving force for the electrons to transfer between the two electrodes in order to screen this potential difference. Because of the rectifier, electron flow in either direction between the two electrodes will be rectified to charging direction of the LIB part, thus stores the electrical energy in the LIB. Ideally, the amount of charges stored in the LIB during in each half cycle should equal to the number of tribo-charges on the Kapton surface. When the SCPU is subjected to a lasting mechanical agitation, this cycle from Figure 7.4b to 7.4e will keep taking place so that more and more energy will be stored in the LIB part of the SCPU. After the LIB part got fully charged by the TENG part, the SCPU will switch into the "active state", in which the LIB part is discharged by driving the external load.

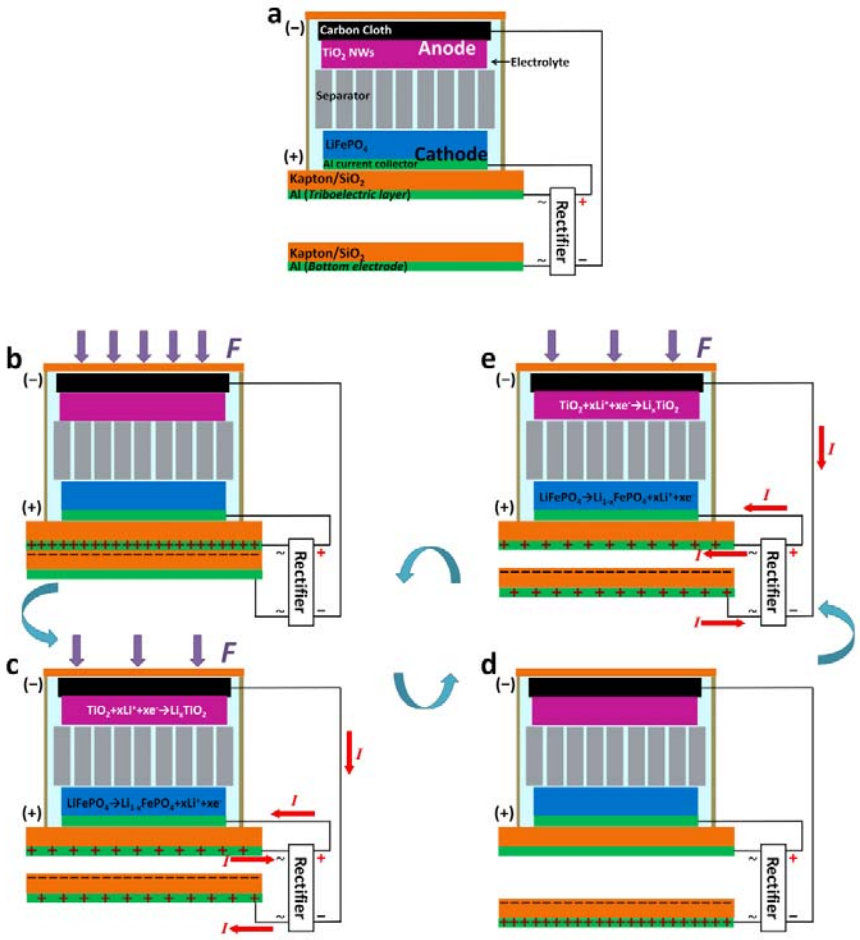

Figure 7.4 Basic working principle of the SCPU in the "standby-active mode". (a) A two-dimensional sketch showing the structure and the original state of the SCPU before mechanical deformation. For clarity, the arch-shape is expressed as a flat structure. (b) Mechanical pressing brings the top Al and the bottom Kapton into contact, generating opposite triboelectric charges on the two surfaces. (c) The force is releasing and the SCPU is reverting to its original arch shape. The induced potential difference generates the first current peak, which charges the LIB part. (d) The SCPU returns to its original shape, with induced potential difference fully screened. (e) The SCPU is pressed again and the redundant charges on the bottom electrodes flows back, generating the second current peak to charge the LIB part.

7.3.2 Performance of the SCPU Working in "Standby-Active Mode"

The "standby-active mode" of the SCPU is shown schematically in the circuit diagrams in Figure 7.5a. In the real demonstration of a typical SCPU device, the LIB is

connected to the TENG through the rectifier but disconnected from the load (with S1 closed and S2 open), during which it is only storing the electrical energy generated by the TENG part. As demonstrated in Figure 7.5b, the LIB was charged to its full capacity in ~11 hours by the TENG under a deformation frequency of 9 Hz, with the voltage ($V_{Battery}$) increasing from 0.7 V to 2.5 V crossing the charging plateau at ~1.62 V. This is the "standby mode" during which the SCPU is charged. Next, the fully-charged SCPU will be used as a battery to drive a device by switching the connection with S1 open and S2 closed. As shown in Figure 7.5b, the fully charged LIB could provide a constant current of 2 μA to the external load for ~ 10 hours (~3 hours at the discharging plateau, which is the actual working time for this LIB as a constant-voltage power source). This is the "active mode" of the SCPU during which it is used to drive a device. In practical applications, the SCPU switches between the "standby mode" and the "active mode", which correspond to the charging and discharging of the LIB, respectively. This operational integration methodology of energy harvesting and storage is particularly suitable for applications where the current required by certain electronic devices is much larger than the average current (rather than the peak current) generated by the TENG, and the electronic devices do not need to work continuously. This meets the requirement of some sensors for intermittent detections.

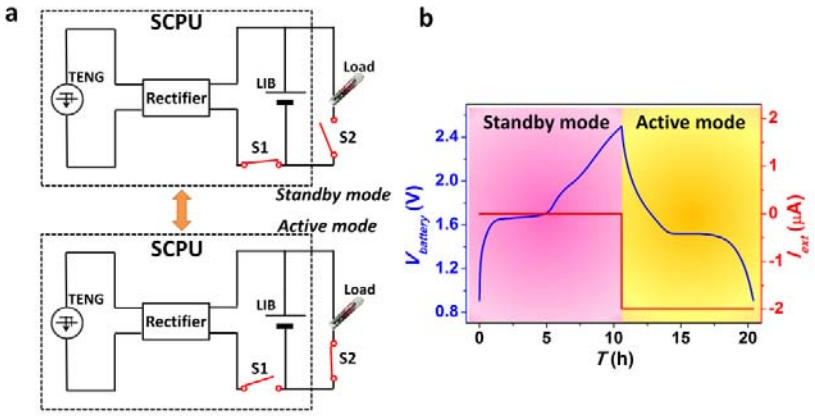

Figure 7.5 Performance of the SCPU in the "standby-active mode" as an integrated DC power source. (a) Electrical circuit diagram showing the "standby-active mode" for the integration of the TENG part and the LIB part. The portion enclosed by the dotted square is the SCPU. (b) The voltage profile showing the LIB part fully charged by the TENG part (the "standby mode") and then discharging under a current of 2 μA (the "active mode").

7.4 SCPU Working in "Sustainable Mode"

Alternatively, in the cases that the electronic devices need to work constantly, the SCPU can work in a "sustainable mode", in which the LIB is being charged by the TENG while it is simultaneously powering an external load. As long as the averaged current converted from the surrounding mechanical energy is approximately the same as the current required by the load, the energy stored in the LIB will remain at a stable level so that the voltage can remain at its discharging plateau "forever" due to the nature of electrochemical reactions.

7.4.1 Working Mechanism of the SCPU in "Sustainable Mode"

In the sustainable mode, the SCPU is being simultaneously charged and discharged due to the connection to an external load, as shown in Figure 7.6. The AC pulses generated by the TENG are first rectified, and then directed into the LIB from its positive electrode. But when the LIB is connected to the external load, the positive electrode is always at a higher potential. This causes the current to flow from the positive electrode to the load, which will be in the reversed direction in reference to the charging current, but flowing through two separated electrical connections. Thus, the electrochemical reactions corresponding to both charging and discharging are occurring simultaneously at each electrode. The voltage applied across the load will be the voltage of the LIB (Fig. 7.6), which is determined by the difference in the electrode potentials of the two half-reactions. Since the electrode potential is not affected by the state of charge (SOC) within the wide-range discharging plateau,[24,112] the irregular and fluctuating

current generated by the TENG due to the change of the surround mechanical motion will not cause an obvious change in the output voltage of the LIB. This stable constant voltage on the load should be able to be maintained for an infinitely long time in principle, as long as the averaged current provided by the TENG over time is about the same as the current consumed by the load, so that the SOC of the LIB does not shift out of the voltage plateau. In this proposed integration mode of mechanical energy harvesting and energy storage, the consumed energy is generated from the surrounding mechanical motion, thus the amount of energy stored in the LIB will not change very much although the load is being driven continuously. Therefore, the battery works not only as an energy storage unit, but more importantly as a power regulator that converts the irregular, unstable and time-dependent input from the TENG (due to the varying ambient condition), to a constant DC output. This is the reason that the SCPU can be a stable DC power source in the "sustainable mode".

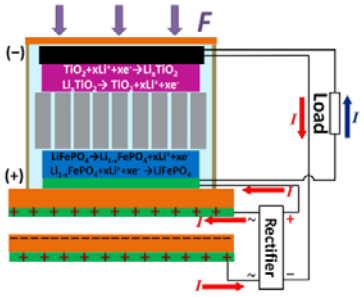

Figure 6.6 Basic working principle of the SCPU in the "sustainable mode", in which the LIB part is driving an external load while being charged by the TENG part. Both the charging and discharging reactions take place at the electrodes (the blue arrow stands for the discharging current through the load).

7.4.2 Performance of the SCPU Working in "Sustainable Mode"

When the above SCPU is working in the "sustainable mode", the TENG and the LIB parts are connected as shown in Figure 7.7a. As shown in Figure 7.7b, when the SCPU was being triggered by a pressing motion at 9 Hz (the averaged current produced

can be estimated as ~1.98 μA according to the result of the measured charge transfer in Fig. 7.2b), the LIB part provided a constant current of 2 μA at the voltage of ~1.55 V for more than 40 hours! Thus, in this proposed "sustainable mode", the SCPU could work as an independent, self-sufficient and sustainable power source for providing a constant voltage.

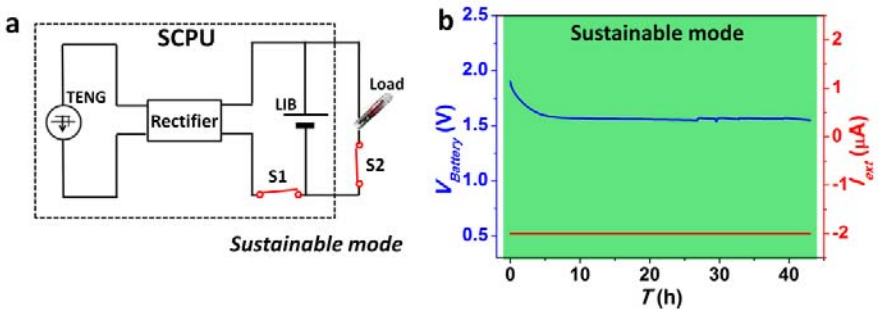

Figure 7.7 Performance of the SCPU in the "sustainable mode" as an integrated DC power source. (a) The electrical circuit diagram showing the newly-proposed "sustainable mode", in which the LIB part is driving the external load while it is being charged by the TENG part. (b) In this sustainable mode, the SCPU provided a 2-μA DC current with a constant voltage of 1.53 V for more than 40 hours, when the SCPU was deformed under a frequency of 9 Hz.

7.4.3 Application of the SCPU as a Sustainable Power Source for Electronics

In a lot of applications, a constant voltage from the power source is needed for the operation of the electronic systems. For example, in a sensing system for detecting the change in the environment through the resulted change of the sensor's effective resistance, the current as the measurable signal should solely depend on the sensor's resistance, so that the whole system can be calibrated. For many sensing purposes, changes in the environment need to be constantly monitored without interruption so that any undesired instances can be detected immediately, thus, the use of battery may have its limitation due to its relatively short lifetime. The demonstrated SCPU under the "sustainable mode" can serve as a non-stop power source for these applications. We used a ZnO-nanowire-based UV sensor[116] to demonstrate this unique capability of the SCPU.

In the sensor, the nanowire is bonded onto the substrate at its two ends with silver paste, forming a metal-semiconductor-metal structure (the left inset of Fig. 7.8a). A Schottky contact is formed so that the I-V has a rectifying behavior. In the first case (Fig. 7.8a), we only used the fully charged LIB portion of the SCPU to power this UV sensor as shown in the inset (right) of Figure 7.8a, which is the "active mode" of the SCPU illustrated in Figure 7.5a. When the UV light is off, with an input voltage of ~1.53 V from the battery at its discharging plateau, the measured current through the sensor was around 1.55 μA. When UV light is turned on, the current jumped to a level of ~2.95 μA. We periodically turned the UV light on and off, and the voltage of the battery remained stable during the first few cycles. However, after ~3.5 hours, the voltage started to drop, which indicated that the battery was running out of charge. As a result, the current levels for the UV-off and UV-on states both decreased to lower levels, and thus could not be an effective indicator for the presence of UV-illumination anymore since it cannot be judged using the calibrated current, which means that this battery has to be replaced after about 4 hours usage.

This problem can be solved using the SCPU in the proposed "sustainable mode". As shown in Figure 7.8b, when the LIB was being charged by the TENG under a deformation frequency of 9 Hz while driving the UV sensor, the output voltage of the battery can stay at the plateau of around 1.55 V with only small fluctuation for over 12 hours, during which the UV light was periodically turned on and off for more than 10 times without obvious decay in current level, which can clearly convey the information of the UV illumination to the calibrated system. Therefore, it has been undoubtedly demonstrated that with the "hybridization" of the mechanical energy harvesting and energy storage in the SCPU, an electronic system could be truly self-powered continuously and sustainable.

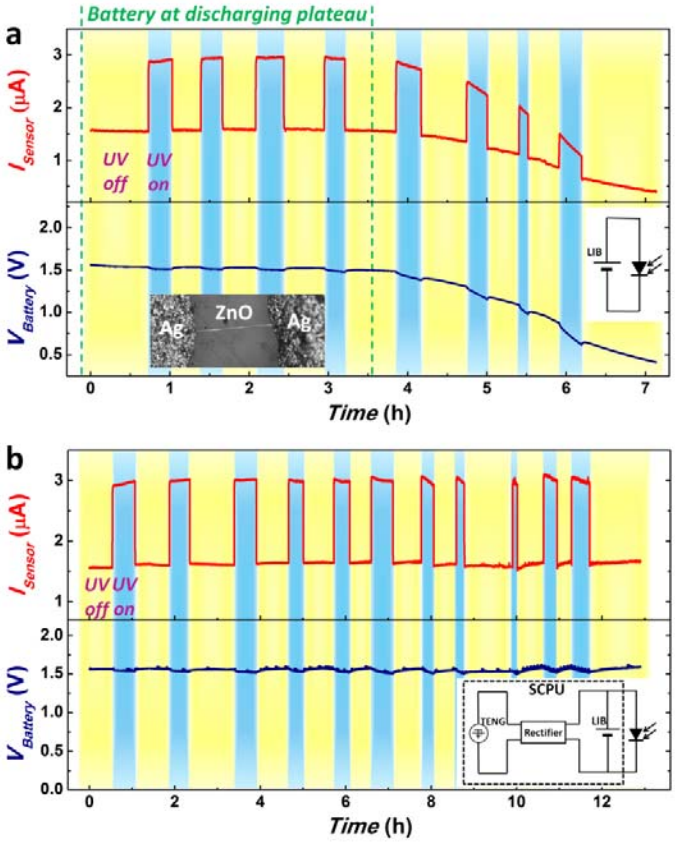

Figure 7.8 The SCPU as a sustainable power source for driving a UV sensor. (a) Operation of the UV sensor when solely driven by the LIB part in the SCPU, which was recorded from the point that the battery just entered its discharging plateau. The left inset is an optical microscope image of the ZnO-nanowire-based UV sensor in this demonstration, and the right inset is the circuit diagram showing the power source. (b) The operation of the UV sensor continuously driven by the SCPU in the "sustainable mode" for ~13 hours. The inset is the circuit diagram showing the UV sensor powered by the SCPU in the "sustainable mode". In both of a and b, the top curve (red) is the current though the sensor, reflecting its response to the UV light, and the bottom curve (blue) is the real time voltage of LIB part.

7.5 Impacts of the Hybridization of Mechanical Energy Harvesting and Energy Storage

Through integrating the mechanical energy harvesting and the energy storage both physically and operationally, the intrinsic limitations of these two technologies can be

remarkably overcome. For the electricity generated by TENGs, the electrical output is pulse-shaped due to their fundamental working mechanism. This output is often noncontinuous and irregular, therefore cannot be used to directly power electronic devices in most cases. By combining a TENG with a LIB in the "sustainable mode", the TENG's only function is to replenish the energy drain in the LIB, so that the harvested mechanical energy can be used to drive the load at a constant voltage through the LIB, which benefits from the stable potential difference between the two electrodes in the electrochemical reaction. Thus, in this integration, the battery works not only as an energy storage, but also as a power regulator (for changing the pulsed electrical outputs into a constant voltage), not just as an energy storage unit. This is a new role for batteries, and can potentially change the traditional views in the battery technology. Since the stored energy in the battery will not be fully used up, having a large capacity in the battery for a longer lifetime through the improvement of the materials' energy densities is no longer essential, which, however, is the current trend in battery research. Also, the size and weight of the battery can be miniaturized, and waste chemicals from dead batteries can be greatly reduced. Moreover, this demonstration opens the door to a new research field for developing long lifetime power sources, that is a wise integration of the TENG and the battery, in the aspects such as the appropriate design of the TENG to meet the desired energy consumption of the load, the optimum capacity of the battery to tolerate the estimated output fluctuation of the TENG in certain environment, and so on.

CHAPTER 8

CONCLUSION

Along with the development of the human civilization, the demand for energy is growing and expanding exponentially, not only for the total quantity in large scale, but for unprecedented functionalities in much smaller scale. For addressing people's demand for energy from different aspects, energy harvesting and energy storage emerge as the two major fields. The chief focus of the research in this dissertation is about the harnessing of mechanical energy—a form of energy that is universally existing in our life and in the nature but has not been fully utilized. Based on the effect of triboelectrification, we developed a new technology—triboelectric nanogenerators—for generating electricity from mechanical motions. Through establishing fundamental operation mechanisms and modes, largely improving power output by rational structural design, developing a variety of structures for harvesting different types of mechanical energies, the research in this dissertation has greatly propel the development of this recently-invented technology. In the further step, in order to utilize mechanical energy for driving electronics sustainably with a constant voltage output, we explored the hybridization of mechanical energy harvesting and energy storage. In this dissertation, both fundamentally-new process for energy conversion and storage, and power units with unprecedented functionalities have been demonstrated.

The basic working principle of triboelectric nanogenerators is the conjunction of triboelectric effect and electrostatic induction based on the periodic contact-separation of two triboelectrically-charged surfaces. Such a contact-separation process can be realized in vertical-to-plane direction, which serves as the first basic mode of TENGs—vertical contact-mode. In order to largely improve the output of the TENG in this mode by enabling an effective electrostatic induction, we rationally designed arch-shaped structure in the TENG, which can enable both the intimate contact and fully separation of the two

triboelectric surfaces. This unique structure achieved a largely improved power output: 128 mW/cm^3 (voltage of 230 V and current of 0.13 mA). This is also the first demonstration of TENG based on the triboelectrification between a conductor and a dielectric. The basic mechanism has been studied both analytically and numerically. With such a high output, the TENG has been demonstrated and systematically studied as a direct power source for electronic devices, revealing the dependence of the TENG's output on the resistance of the external load. Moreover, the TENG was used to build up a power module together with a Li-ion battery for driving a wireless sensor system as well as a commercial cell phone.

In the above contact-mode based TENG, an air gap is mandatory so that the two triboelectrically-charged surfaces can get separated. This usually requires sophisticated design of the device structures. Fundamentally, the charge separation can also be achieved in in-plane direction by sliding motion. Based on this, we for the first time demonstrated the second basic mode of TENG—the lateral sliding-mode. In the first step, the experimental operation and the working principle of this new mode was developed. The voltage generation process and the charge transfer behavior from the sliding motion were clearly outlined by finite-element simulation. According to our experimental study, the electrical outputs have a strong dependence on the sliding motion including the vertical distance and velocity. Based on this mechanism, we further introduced a novel design of disk-shaped triboelectric nanogenerator for harvesting rotational energy. Through experimental comparison, we found an enhancement of current from finer segmental patterns, which can serve as the guidance for future structural design. The disk TENG makes it possible to generate electricity continuously with a high frequency and a high magnitude of power density, showing unprecedented superiority in both driving electronics directly and continuously as well as charging energy storage units. In order to further improve the power output from the harvesting of rotational energy, we develop the disk-structured TENG into multi-layers by ensuring a synchronized rotation of all the

layers and intimate contacts between adjacent triboelectric surfaces. Furthermore, based on the hybridization of the contact-mode and the sliding-mode for TENGs, a wind-cup-based TENG has been demonstrated for effectively harvesting wind energy, especially weak-wind available outdoors.

In the above two modes of TENGs—the contact mode and the sliding mode, each triboelectric layer is attached with an electrode and a lead wire. Such a device configuration largely limits TENGs' versatility and applicability for harvesting energy from an arbitrary moving object. In this regard, we developed a new mode of TENG—freestanding-layer-based mode that can scavenge energy from the mechanical motion of a freestanding object, without an attached electrode. With two stationary electrodes alternatively approached by the tribo-charges on the sliding layer, an alternating current is generated between the electrodes due to electrostatic induction. Compared to the sliding-mode TENG, this new mode has a good tolerance to the vertical separation between the sliding triboelectric surface and the electrode, so that it can operate in both contact and non-contact sliding mode. Because of these unique features, the freestanding-layer-mode TENG can achieve versatile energy harvesting from unrestricted and freely-moving mechanical energy sources, such as a free walking man, a moving car or train, at a greatly-enhanced efficiency. In order to increase the output and applicability for mechanical energy, we developed the grating-structured freestanding-layer TENG. The GF-TENG with finer grating units exhibits improved performance in the respect of the amount of collectable charges, current density, and output frequency. When the device is operated in non-contact mode, it shows an excellent stability and high total conversion efficiency up to 85% at low operation frequency. We further expanded the basic design of this mode of TENG to the disk structures, making it possible to harvesting rotational energy in non-contact mode. Compared with the sliding-mode based disk TENG, this new design has much higher stability and durability, and much smaller deterioration in performance at the non-contact mode.

Since the static surface charge density is the most important factor for the output of the TENGs, we systematically studied the maximum surface charge density through introducing the ionized-air-injection method for the generation of the surface charges. Using this method, the maximum surface charge density for any TENG structure can obtained from the experiments. This maximum surface charge density was studied both experimentally and theoretically, leading to an important conclusion that the maximum surface charge density will get larger at smaller thickness of the dielectric film in the TENG. This will serve as an important guideline for the structure of TENG when trying to increase the triboelectric charge density through materials optimization. Besides, the ionized-air-injection method introduced in this work also provides an effective method for the enhancement of TENGs' power output.

In many cases, the generated electricity through environmental energy harvesting needs to be stored in energy storage units before used to drive electronic devices. In general, electricity generation and energy storage are two distinct processes that are accomplished through two separated units. In this research, we hybridized a piezoelectric nanogenerator for mechanical energy harvesting with a Li-ion battery for energy storage into one device—a self-charging power cell, by replacing the PE separator as for conventional Li battery with a piezoelectric PVDF film. Based on this convoluted structure, a new mechanical-to-electrochemical process is proposed for simultaneously converting and storing mechanical energy directly as chemical energy, with a significantly higher overall efficiency than the traditional charging method composed of two separated units. This new concept of device provides an innovative approach for developing new sustainable power sources for personal electronics.

Such a hybridization of a mechanical energy harvester and a Li-ion battery was also performed on the recently invented triboelectric nanogenerator. This was realized by building a flexible Li-ion battery (LIB) on an arch-shaped TENG structure. As triggered by ambient mechanical vibrations, the TENG part can efficiently generate electricity with

high output, and the rectified electrical energy can be stored in the LIB part. Based on such a device, we proposed a new mode for the integration—the "sustainable mode", in which the surrounding mechanical energy is harvested and simultaneously stored in the LIB, while the LIB is driving an external device. The self-charging power unit (SCPU) in this mode can provide a constant voltage for continuously powering electronic devices. Hence, the integrated SCPU in the proposed "sustainable mode" can potentially serve as an independent, portable, sustainable and stable power unit, which will meet the general requirement of almost any electronic device and make the self-powered system more feasible by harvesting ambient mechanical energy.

It can be anticipated that the development of the fundamental principles and structural designs for mechanical energy harvesting and the demonstration of the new concepts of power sources could open up a broad research direction, especially for material scientists. Through improving the properties of the active materials, the performance of these technologies can be largely enhanced, and hopefully begins to change people's everyday life in the near future.

REFERENCES

1 Goldemberg, J. Special issue on sustainability and energy: Perspectives: "Ethanol for a sustainable energy future" (vol 315, pg 808, 2007). *Science* **317**, 1325-1325 (2007).

2 Bertine, K. K. & Goldberg, E. D. Fossil fuel combustion and major sedimentary cycle. *Science* **173**, 233-& (1971).

3 Dresselhaus, M. S. & Thomas, I. L. Alternative energy technologies. *Nature* **414**, 332-337 (2001).

4 Avouris, P. & Martel, R. Progress in carbon nanotube electronics and photonics. *Mrs Bulletin* **35**, 306-313 (2010).

5 Dionne, J. A., Sweatlock, L. A., Sheldon, M. T., Alivisatos, A. P. & Atwater, H. A. Silicon-based plasmonics for on-chip photonics. *Ieee Journal of Selected Topics in Quantum Electronics* **16**, 295-306 (2010).

6 Patolsky, F., Timko, B. P., Yu, G. H., Fang, Y., Greytak, A. B., Zheng, G. F. & Lieber, C. M. Detection, stimulation, and inhibition of neuronal signals with high-density nanowire transistor arrays. *Science* **313**, 1100-1104 (2006).

7 Tian, B. Z., Cohen-Karni, T., Qing, Q., Duan, X. J., Xie, P. & Lieber, C. M. Three-dimensional, flexible nanoscale field-effect transistors as localized bioprobes. *Science* **329**, 830-834 (2010).

8 Wang, Z. L. Towards self-powered nanosystems: From nanogenerators to nanopiezotronics. *Advanced Functional Materials* **18**, 3553-3567 (2008).

9 Paradiso, J. A. & Starner, T. Energy scavenging for mobile and wireless electronics. *Ieee Pervasive Computing* **4**, 18-27 (2005).

10 Brabec, C. J., Sariciftci, N. S. & Hummelen, J. C. Plastic solar cells. *Advanced Functional Materials* **11**, 15-26 (2001).

11 Huynh, W. U., Dittmer, J. J. & Alivisatos, A. P. Hybrid nanorod-polymer solar cells. *Science* **295**, 2425-2427 (2002).

12 Oregan, B. & Gratzel, M. A low-cost, high-efficiency solar-cell based on dye-sensitized colloidal tio2 films. *Nature* **353**, 737-740 (1991).

13 Tian, B. Z., Zheng, X. L., Kempa, T. J., Fang, Y., Yu, N. F., Yu, G. H., Huang, J. L. & Lieber, C. M. Coaxial silicon nanowires as solar cells and nanoelectronic power sources. *Nature* **449**, 885-U888 (2007).

14 Law, M., Greene, L. E., Johnson, J. C., Saykally, R. & Yang, P. D. Nanowire dye-sensitized solar cells. *Nature Materials* **4**, 455-459 (2005).

15 Luther, J. M., Law, M., Beard, M. C., Song, Q., Reese, M. O., Ellingson, R. J. & Nozik, A. J. Schottky solar cells based on colloidal nanocrystal films. *Nano Letters* **8**, 3488-3492 (2008).

16 Dresselhaus, M. S., Chen, G., Tang, M. Y., Yang, R. G., Lee, H., Wang, D. Z., Ren, Z. F., Fleurial, J. P. & Gogna, P. New directions for low-dimensional thermoelectric materials. *Advanced Materials* **19**, 1043-1053 (2007).

17 Snyder, G. J. & Toberer, E. S. Complex thermoelectric materials. *Nature Materials* **7**, 105-114 (2008).

18 Venkatasubramanian, R., Siivola, E., Colpitts, T. & O'Quinn, B. Thin-film thermoelectric devices with high room-temperature figures of merit. *Nature* **413**, 597-602 (2001).

19 Beeby, S. P., Tudor, M. J. & White, N. M. Energy harvesting vibration sources for microsystems applications. *Measurement Science & Technology* **17**, R175-R195 (2006).

20 Gust, D., Moore, T. A. & Moore, A. L. Solar fuels via artificial photosynthesis. *Accounts of Chemical Research* **42**, 1890-1898 (2009).

21 Shao, Z. P. & Haile, S. M. A high-performance cathode for the next generation of solid-oxide fuel cells. *Nature* **431**, 170-173 (2004).

22 Steele, B. C. H. & Heinzel, A. Materials for fuel-cell technologies. *Nature* **414**, 345-352 (2001).

23 Wang, Z. L. & Song, J. H. Piezoelectric nanogenerators based on zinc oxide nanowire arrays. *Science* **312**, 242-246 (2006).

24 Tarascon, J. M. & Armand, M. Issues and challenges facing rechargeable lithium batteries. *Nature* **414**, 359-367 (2001).

25 Bruce, P. G., Scrosati, B. & Tarascon, J. M. Nanomaterials for rechargeable lithium batteries. *Angewandte Chemie-International Edition* **47**, 2930-2946 (2008).

26 Simon, P. & Gogotsi, Y. Materials for electrochemical capacitors. *Nature Materials* **7**, 845-854 (2008).

27 Beeby, S. P., Torah, R. N., Tudor, M. J., Glynne-Jones, P., O'Donnell, T., Saha, C. R. & Roy, S. A micro electromagnetic generator for vibration energy harvesting. *Journal of Micromechanics and Microengineering* **17**, 1257-1265 (2007).

28 Sari, I., Balkan, T. & Kulah, H. An electromagnetic micro power generator for wideband environmental vibrations. *Sensors and Actuators a-Physical* **145**, 405-413 (2008).

29 Mitcheson, P. D., Miao, P., Stark, B. H., Yeatman, E. M., Holmes, A. S. & Green, T. C. Mems electrostatic micropower generator for low frequency operation. *Sensors and Actuators a-Physical* **115**, 523-529 (2004).

30 Miao, P., Mitcheson, P. D., Holmes, A. S., Yeatman, E. M., Green, T. C. & Stark, B. H. Mems inertial power generators for biomedical applications. *Microsystem Technologies-Micro-and Nanosystems-Information Storage and Processing Systems* **12**, 1079-1083 (2006).

31 Shenck, N. S. & Paradiso, J. A. Energy scavenging with shoe-mounted piezoelectrics. *Ieee Micro* **21**, 30-42 (2001).

32 Sohn, J. W., Choi, S. B. & Lee, D. Y. An investigation on piezoelectric energy harvesting for mems power sources. *Proceedings of the Institution of Mechanical Engineers Part C-Journal of Mechanical Engineering Science* **219**, 429-436 (2005).

33 Wang, X. D., Song, J. H., Liu, J. & Wang, Z. L. Direct-current nanogenerator driven by ultrasonic waves. *Science* **316**, 102-105 (2007).

34 Xu, S., Qin, Y., Xu, C., Wei, Y. G., Yang, R. S. & Wang, Z. L. Self-powered nanowire devices. *Nature Nanotechnology* **5**, 366-373 (2010).

35 Yang, R. S., Qin, Y., Dai, L. M. & Wang, Z. L. Power generation with laterally packaged piezoelectric fine wires. *Nature Nanotechnology* **4**, 34-39 (2009).

36 Zhu, G. A., Yang, R. S., Wang, S. H. & Wang, Z. L. Flexible high-output nanogenerator based on lateral zno nanowire array. *Nano Letters* **10**, 3151-3155 (2010).

37 Qin, Y., Wang, X. D. & Wang, Z. L. Microfibre-nanowire hybrid structure for energy scavenging. *Nature* **451**, 809-U805 (2008).

38 Lowell, J. & Roseinnes, A. C. Contact electrification. *Advances in Physics* **29**, 947-1023 (1980).

39 Castle, G. S. P. Contact charging between insulators. *Journal of Electrostatics* **40-1**, 13-20 (1997).

40 McCarty, L. S. & Whitesides, G. M. Electrostatic charging due to separation of ions at interfaces: Contact electrification of ionic electrets. *Angewandte Chemie-International Edition* **47**, 2188-2207 (2008).

41 Baytekin, H. T., Patashinski, A. Z., Branicki, M., Baytekin, B., Soh, S. & Grzybowski, B. A. The mosaic of surface charge in contact electrification. *Science* **333**, 308-312 (2011).

42 Fan, F. R., Lin, L., Zhu, G., Wu, W. Z., Zhang, R. & Wang, Z. L. Transparent triboelectric nanogenerators and self-powered pressure sensors based on micropatterned plastic films. *Nano Letters* **12**, 3109-3114 (2012).

43 Fan, F. R., Tian, Z. Q. & Wang, Z. L. Flexible triboelectric generator. *Nano Energy* **1**, 328-334 (2012).

44 Zhu, G., Pan, C. F., Guo, W. X., Chen, C. Y., Zhou, Y. S., Yu, R. M. & Wang, Z. L. Triboelectric-generator-driven pulse electrodeposition for micropatterning. *Nano Letters* (2012).

45 Ulaby, F. T. *Fundamentals of applied electromagnetics*. 2001 media edn, (Prentice Hall, 2001).

46 Leijon, M., Danielsson, O., Eriksson, M., Thorburn, K., Bernhoff, H., Isberg, J., Sundberg, J., Ivanova, I., Sjostedt, E., Agren, O., Karlsson, K. E. & Wolfbrandt, A. An electrical approach to wave energy conversion. *Renewable Energy* **31**, 1309-1319 (2006).

47 Yeh, T. H. & Wang, L. Selection of wind generator capacity for capturing maximum wind energy in wind power generation systems. *Proceedings of the Eighth IASTED International Conference on Power and Energy Systems*, 137-142 (2005).

48 Bressers, S., Avirovik, D., Vernieri, C., Regan, J., Chappell, S., Hotze, M., Luhman, S., Lallart, M., Inman, D. & Priya, S. Small-scale modular windmill. *American Ceramic Society Bulletin* **89**, 34-40 (2010).

49 Platt, S. R., Farritor, S., Garvin, K. & Haider, H. The use of piezoelectric ceramics for electric power generation within orthopedic implants. *Ieee-Asme Transactions on Mechatronics* **10**, 455-461 (2005).

50 Ramsay, M. J. & Clark, W. W. Piezoelectric energy harvesting for bio mems applications. *Smart Structures and Materials 2001: Industrial and Commercial Applications of Smart Structures Technologies* **4332**, 429-438 (2001).

51 White, N. M., Glynne-Jones, P. & Beeby, S. P. A novel thick-film piezoelectric micro-generator. *Smart Materials & Structures* **10**, 850-852 (2001).

52 Xu, S., Wei, Y. G., Liu, J., Yang, R. & Wang, Z. L. Integrated multilayer nanogenerator fabricated using paired nanotip-to-nanowire brushes. *Nano Letters* **8**, 4027-4032 (2008).

53 Chang, C. E., Tran, V. H., Wang, J. B., Fuh, Y. K. & Lin, L. W. Direct-write piezoelectric polymeric nanogenerator with high energy conversion efficiency. *Nano Letters* **10**, 726-731 (2010).

54 Hu, Y. F., Zhang, Y., Xu, C., Lin, L., Snyder, R. L. & Wang, Z. L. Self-powered system with wireless data transmission. *Nano Letters* **11**, 2572-2577 (2011).

55 Zhu, G., Wang, A. C., Liu, Y., Zhou, Y. S. & Wang, Z. L. Functional electrical stimulation by nanogenerator with 58 v output voltage. *Nano Letters* **12**, 3086-3090 (2012).

56 Wang, Z. L., Zhu, G., Yang, Y., Wang, S. H. & Pan, C. F. Progress in nanogenerators for portable electronics. *Materials Today* **15**, 532-543 (2012).

57 Henniker, J. Triboelectricity in polymers. *Nature* **196**, 474-& (1962).

58 Davies, D. K. Charge generation on dielectric surfaces. *Journal of Physics D-Applied Physics* **2**, 1533-& (1969).

59 Diaz, A. F. & Felix-Navarro, R. M. A semi-quantitative tribo-electric series for polymeric materials: The influence of chemical structure and properties. *Journal of Electrostatics* **62**, 277-290 (2004).

60 Arico, A. S., Bruce, P., Scrosati, B., Tarascon, J. M. & Van Schalkwijk, W. Nanostructured materials for advanced energy conversion and storage devices. *Nature Materials* **4**, 366-377 (2005).

61 Poizot, P., Laruelle, S., Grugeon, S., Dupont, L. & Tarascon, J. M. Nano-sized transition-metaloxides as negative-electrode materials for lithium-ion batteries. *Nature* **407**, 496-499 (2000).

62 Chan, C. K., Peng, H. L., Liu, G., McIlwrath, K., Zhang, X. F., Huggins, R. A. & Cui, Y. High-performance lithium battery anodes using silicon nanowires. *Nature Nanotechnology* **3**, 31-35 (2008).

63 Kang, B. & Ceder, G. Battery materials for ultrafast charging and discharging. *Nature* **458**, 190-193 (2009).

64 Kovalenko, I., Zdyrko, B., Magasinski, A., Hertzberg, B., Milicev, Z., Burtovyy, R., Luzinov, I. & Yushin, G. A major constituent of brown algae for use in high-capacity li-ion batteries. *Science* **334**, 75-79 (2011).

65 Wu, H., Chan, G., Choi, J. W., Ryu, I., Yao, Y., McDowell, M. T., Lee, S. W., Jackson, A., Yang, Y., Hu, L. B. & Cui, Y. Stable cycling of double-walled silicon nanotube battery anodes through solid-electrolyte interphase control. *Nature Nanotechnology* **7**, 309-314 (2012).

66 Mukherjee, R., Krishnan, R., Lu, T. M. & Koratkar, N. Nanostructured electrodes for high-power lithium ion batteries. *Nano Energy* **1**, 518-533 (2012).

67 Cross, J. A. *Electrostatics : Principles, problems and applications*. (Hilger, 1987).

68 Wang, S. H., Lin, L. & Wang, Z. L. Nanoscale triboelectric-effect-enabled energy conversion for sustainably powering portable electronics. *Nano Letters* **12**, 6339-6346 (2012).

69 Hsueh, C. H. Modeling of elastic deformation of multilayers due to residual stresses and external bending. *Journal of Applied Physics* **91**, 9652-9656 (2002).

70 Sinha, A. K., Levinstein, H. J. & Smith, T. E. Thermal-stresses and cracking resistance of dielectric films (sin, si3n4, and sio2) on si substrates. *Journal of Applied Physics* **49**, 2423-2426 (1978).

71 Hu, Y. F., Zhang, Y., Xu, C., Zhu, G. A. & Wang, Z. L. High-output nanogenerator by rational unipolar assembly of conical nanowires and its application for driving a small liquid crystal display. *Nano Letters* **10**, 5025-5031 (2010).

72 Niu, S. M., Wang, S. H., Lin, L., Liu, Y., Zhou, Y. S., Hu, Y. F. & Wang, Z. L. Theoretical study of contact-mode triboelectric nanogenerators as an effective power source. *Energy & Environmental Science* **6**, 3576-3583 (2013).

73 Mccabe, J. H. Continued fraction expansion, with a truncation error estimate, for dawsons integral. *Mathematics of Computation* **28**, 811-816 (1974).

74 Sloane, N. J. A. The on-line encyclopedia of integer sequences. *Towards Mechanized Mathematical Assistants* **4573**, 130-130 (2007).

75 Zhang, X. S., Han, M. D., Wang, R. X., Zhu, F. Y., Li, Z. H., Wang, W. & Zhang, H. X. Frequency-multiplication high-output triboelectric nanogenerator for sustainably powering biomedical microsystems. *Nano Letters* (2013).

76 Zhong, J. W., Zhong, Q. Z., Fan, F. R., Zhang, Y., Wang, S. H., Hu, B. & Wang, Z. L. Finger typing driven triboelectric nanogenerator and its use for instantaneously lighting up leds. *Nano Energy* (2012).

77 Wang, S. H., Lin, L., Xie, Y. N., Jing, Q. S., Niu, S. M. & Wang, Z. L. Sliding-triboelectric nanogenerators based on in-plane charge-separation mechanism. *Nano Letters* **13**, 2226-2233 (2013).

78 Lin, L., Wang, S. H., Xie, Y. N., Jing, Q. S., Niu, S. M., Hu, Y. F. & Wang, Z. L. Segmentally structured disk triboelectric nanogenerator for harvesting rotational mechanical energy. *Nano Letters* **13**, 2916-2923 (2013).

79 Xie, Y. N., Wang, S. H., Niu, S. M., Lin, L., Jing, Q. S., Su, Y. J., Wu, Z. Y. & Wang, Z. L. Multi-layered disk triboelectric nanogenerator for harvesting hydropower. *Nano Energy* **Under Review** (2014).

80 Xie, Y. N., Wang, S. H., Lin, L., Jing, Q. S., Lin, Z. H., Niu, S. M., Wu, Z. Y. & Wang, Z. L. Rotary triboelectric nanogenerator based on a hybridized mechanism for harvesting wind energy. *Acs Nano* **7**, 7119-7125 (2013).

81 Fang, H., Wu, W. Z., Song, J. H. & Wang, Z. L. Controlled growth of aligned polymer nanowires. *Journal of Physical Chemistry C* **113**, 16571-16574 (2009).

82 Saurenbach, F., Wollmann, D., Terris, B. D. & Diaz, A. F. Force microscopy of ion-containing polymer surfaces - morphology and charge structure. *Langmuir* **8**, 1199-1203 (1992).

83 Niu, S. M., Liu, Y., Wang, S. H., Lin, L., Zhou, Y. S., Hu, Y. F. & Wang, Z. L. Theory of sliding-mode triboelectric nanogenerators. *Advanced Materials* **25**, 6184-6193 (2013).

84 Bai, P., Zhu, G., Lin, Z. H., Jing, Q. S., Chen, J., Zhang, G., Ma, J. & Wang, Z. L. Integrated multi layered triboelectric nanogenerator for harvesting biomechanical energy from human motions. *Acs Nano* **7**, 3713-3719 (2013).

85 Sun, Y. G. & Xia, Y. N. Shape-controlled synthesis of gold and silver nanoparticles. *Science* **298**, 2176-2179 (2002).

86 Ackermann, T. & Soder, L. Wind energy technology and current status: A review. *Renewable & Sustainable Energy Reviews* **4**, 315-374 (2000).

87 Myers, R., Vickers, M., Kim, H. & Priya, S. Small scale windmill. *Applied Physics Letters* **90** (2007).

88 Priya, S. Modeling of electric energy harvesting using piezoelectric windmill. *Applied Physics Letters* **87** (2005).

89 Priya, S., Chen, C. T., Fye, D. & Zahnd, J. Piezoelectric windmill: A novel solution to remote sensing. *Japanese Journal of Applied Physics Part 2-Letters & Express Letters* **44**, L104-L107 (2005).

90 Zhu, G., Lin, Z.-H., Jing, Q. S., Bai, P., Pan, C. F., Yang, Y., Zhou, Y. S. & Wang, Z. L. Toward large-scale energy harvesting by a nanoparticle-enhanced triboelectric nanogenerator. *Nano Letters* **13**, 847-853 (2013).

91 Wang, S. H., Xie, Y. N., Niu, S. M., Lin, L. & Wang, Z. L. Freestanding triboelectric-layer based nanogenerators for harvesting energy from a moving object or human motion in contact and non-contact modes. *Advanced Materials* DOI: 10.1002/adma.201305303 (2014).

92 Yang, Y., Zhang, H. L., Chen, J., Jing, Q. S., Zhou, Y. S., Wen, X. N. & Wang, Z. L. Single-electrode-based sliding triboelectric nanogenerator for self-powered displacement vector sensor system. *ACS Nano* **7**, 7342-7351 (2013).

93 Niu, S. M., Liu, Y., Wang, S. H., Lin, L., Zhou, Y. S., Hu, Y. F. & Wang, Z. L. Theoretical investigation and structural optimization of single-electrode triboelectric nanogenerators. *Advanced Functional Materials* DOI: 10.1002/adfm.201303799 (2014).

94 Eguchi, M. On the permanent electret. *Philosophical Magazine* **49**, 178-192 (1925).

95 Sessler, G. M. & Hillenbrand, J. Electromechanical response of cellular electret films. *Applied Physics Letters* **75**, 3405-3407 (1999).

96 Xie, Y. N., Wang, S. H., Niu, S. M., Lin, L., Jing, Q. S., Yang, J., Wu, Z. Y. & Wang, Z. L. Grating-structured freestanding triboelectric-layer nanogenerator for

harvesting mechanical energy with 85% total conversion efficiency. *Nano Letters*, Submitted (2014).

97 Lin, L., Wang, S. H., Niu, S. M., Liu, C., Xie, Y. N. & Wang, Z. L. Non-contact free-rotating disk triboelectric nanogenerator as a sustainable energy harvester and self-powered mechanical sensor. *ACS Applied Materials & Interfaces* **6**, 3031-3038 (2014).

98 Wang, S. H., Xie, Y. N., Niu, S. M., Lin, L., Liu, C. & Wang, Z. L. Ionized-air-assisted experimentally achieving and theoretically studying the maximum surface charge density for triboelectric generator. In preparation.

99 Waltman, M. J., Dwivedi, P., Hill, H. H., Blanchard, W. C. & Ewing, R. G. Characterization of a distributed plasma ionization source (dpis) for ion mobility spectrometry and mass spectrometry. *Talanta* **77**, 249-255 (2008).

100 Lieberman, M. A. & Lichtenberg, A. J. *Principles of plasma discharges and materials processing*. 2nd edn, (Wiley-Interscience, 2005).

101 Burm, K. T. A. L. Calculation of the townsend discharge coefficients and the paschen curve coefficients. *Contributions to Plasma Physics* **47**, 177-182 (2007).

102 Wakihara, M. & Yamamoto, O. *Lithium ion batteries : Fundamentals and performance*. (Kodansha; Wiley-VCH, 1998).

103 Xue, X. Y., Wang, S. H., Guo, W. X., Zhang, Y. & Wang, Z. L. Hybridizing energy conversion and storage in a mechanical-to-electrochemical process for self-charging power cell. *Nano Letters* **12**, 5048-5054 (2012).

104 Armstrong, G., Armstrong, A. R., Bruce, P. G., Reale, P. & Scrosati, B. Tio2(b) nanowires as an improved anode material for lithium-ion batteries containing $LiFePO_4$ or $LiNi_{0.5}Mn_{1.5}O_4$ cathodes and a polymer electrolyte. *Advanced Materials* **18**, 2597-+ (2006).

105 Zhang, S. S. A review on the separators of liquid electrolyte Li-ion batteries. *Journal of Power Sources* **164**, 351-364 (2007).

106 Macak, J. M., Albu, S. P. & Schmuki, P. Towards ideal hexagonal self-ordering of tio2 nanotubes. *Physica Status Solidi-Rapid Research Letters* **1**, 181-183 (2007).

107 Salimi, A. & Yousefi, A. A. Ftir studies of beta-phase crystal formation in stretched pvdf films. *Polymer Testing* **22**, 699-704 (2003).

108 Fransson, L., Eriksson, T., Edstrom, K., Gustafsson, T. & Thomas, J. O. Influence of carbon black and binder on li-ion batteries. *Journal of Power Sources* **101**, 1-9 (2001).

109 Chiang, C. Y., Shen, Y. J., Reddy, A. J. & Chu, P. P. Complexation of poly(vinylidene fluoride): LiPF6 solid polymer electrolyte with enhanced ion conduction in 'wet' form. *Journal of Power Sources* **123**, 222-229 (2003).

110 Yoshio, M., Brodd, R. J. & Kozawa, A. *Lithium-ion batteries : Science and technologies*. (Springer, 2009).

111 Zhou, Y. K., Cao, L., Zhang, F. B., He, B. L. & Li, H. L. Lithium insertion into TiO_2 nanotube prepared by the hydrothermal process. *Journal of the Electrochemical Society* **150**, A1246-A1249 (2003).

112 Bard, A. J. & Faulkner, L. R. *Electrochemical methods : Fundamentals and applications*. 2nd edn, (John Wiley, 2001).

113 Wang, S. H., Lin, Z. H., Niu, S. M., Lin, L., Xie, Y. N., Pradel, K. C. & Wang, Z. L. Motion charged battery as sustainable flexible-power-unit. *ACS Nano* **7**, 11263-11271 (2013).

114 Lin, Z. H., Roy, P., Shih, Z. Y., Ou, C. M. & Chang, H. T. Synthesis of anatase Se/Te-Tio2 nanorods with dominant {100} facets: Photocatalytic and antibacterial activity induced by visible light. *Chempluschem* **78**, 302-309 (2013).

115 Liu, S. H., Wang, Z. Y., Yu, C., Wu, H. B., Wang, G. & Dong, Q. A flexible TiO_2(b)-based battery electrode with superior power rate and ultralong cycle life. *Advanced Materials* **25**, 3462-3467 (2013).

116 Zhou, J., Gu, Y. D., Hu, Y. F., Mai, W. J., Yeh, P. H., Bao, G., Sood, A. K., Polla, D. L. & Wang, Z. L. Gigantic enhancement in response and reset time of ZnO uv nanosensor by utilizing schottky contact and surface functionalization. *Applied Physics Letters* **94,** 191103 (2009).